

University of Alberta

Development of an Experimental Setup for Measuring Vacuum Decay in Dual-Wall Fiber-Reinforced Composite Pipes

by

Mark Jason Ruhl

A thesis submitted to the Faculty of Graduate Studies and Research
in partial fulfillment of the requirements for the degree of

Master of Science
in
Applied Mechanics

Department of Mechanical Engineering

©Mark Jason Ruhl
Fall 2010
Edmonton, Alberta

Permission is hereby granted to the University of Alberta Libraries to reproduce single copies of this thesis and to lend or sell such copies for private, scholarly or scientific research purposes only. Where the thesis is converted to, or otherwise made available in digital form, the University of Alberta will advise potential users of the thesis of these terms.

The author reserves all other publication and other rights in association with the copyright in the thesis and, except as herein before provided, neither the thesis nor any substantial portion thereof may be printed or otherwise reproduced in any material form whatsoever without the author's prior written permission.

Examining Committee

Pierre Mertiny, Mechanical Engineering, University of Alberta

Marc Secanell, Mechanical Engineering, University of Alberta

Jason Carey, Mechanical Engineering, University of Alberta

Robert Driver, Civil and Environmental Engineering, University of Alberta

Dedication Page

For Doug, Linda, and Michelle.

Abstract

Thermal management and energy input are required to maintain working fluids, i.e., liquefied natural gas, liquid nitrogen, and multi-phase fluids within their optimal working conditions. Increasing a pipes' thermal resistance, e.g., utilizing vacuum insulation, is one method of minimizing energy input. A dual-wall concentric pipe employing a vacuum in the annulus, along with low emissivity surface coatings, is an achievable and economically viable solution. In this study, an experimental setup was designed and utilized to measure the air leakage mass flow rate for single-wall unloaded and mechanically loaded dual-wall fiber reinforced polymeric composite specimens. The mass flow rates were used to develop intrinsic permeability coefficients to quantify leakage, and to determine the maximum serviceable pipe length for a mechanical vacuum pump. In addition, thermal resistance equations were developed to quantify the theoretical heat loss, and an economic study was performed to ascertain the viability for three applications.

Acknowledgements

This work would not have been possible without the support, guidance, and infinite patience of my supervisor, Dr. Pierre Mertiny. Thank you as well to the Department of Mechanical Engineering for providing financial support, and a place to learn and grow, to the Mechanical Engineering shop staff for building my experimental apparatus, to my fellow graduate and undergraduate students for making University life enjoyable, and to Bernie Faulkner for technical support and unfailing doses of humor. Also, thank you to Dr. Mertiny, Dr. Saeed Behzadipour, Dr. Warren Finlay, and Dr. Ben Jar for instilling in me a thirst for research and knowledge.

My list would not be complete without including my parents Doug and Linda, my sisters Cathy and Jennifer, and my wife Michelle. Thank you for your endless support.

MR

Table of Contents

1.	Introduction.....	1
1.1	Background	1
1.2	Outline.....	4
1.3	Flow Chart.....	6
1.4	Possible Applications	7
1.4.1	High-Temperature Superconducting Cables	7
1.4.2	Liquefied Natural Gas.....	9
1.4.3	Hydrogen Pipeline	10
1.4.4	Cryogenic Fluid Storage Tanks	11
1.4.5	Oil Slurries	11
1.5	Effects of FRPC Properties on Vacuum Pressure	12
1.5.1	Density	12
1.5.2	Fiber Volume Fraction.....	12
1.5.3	Void Fraction	13
1.5.4	Ply Thickness	14
1.6	Apercu	14
1.7	References	15
2.	Experimental Setup.....	18
2.1	Dual-Wall Flanged End Connections.....	18
2.1.1	Flanged End Connections	19
2.1.2	Testing Assembly and Installation.....	25
2.1.3	Vacuum Adapter Assembly and Testing	26
2.2	Vacuum Pump and Measuring Devices Installation	28
2.3	Specimen Preparation.....	32
2.3.1	Fiber Volume Fraction.....	35
2.4	Benchtop Test Setup.....	38
2.4.1	Specimen Preparation and Bonding.....	38
2.5	Data Collection.....	39
2.6	Sensor Details.....	41
2.6.1	Thermocouple Gauge.....	41
2.6.2	Capacitance Manometer.....	42
2.6.3	Validyne DP15.....	42

2.6.4	Temperature Sensor	43
2.7	Vacuum System Volume.....	45
2.8	Sampling Frequency and Noise.....	45
2.8.1	Filters	45
2.9	Dual-Wall Test Procedure	47
2.9.1	Controller	47
2.9.2	Loading Considerations	47
2.9.3	Test Procedure	52
2.10	Benchtop Test Procedure.....	54
2.11	Error Analysis.....	55
2.12	Conclusions	55
2.13	References	58
3.	Permeability	60
3.1	Equation Derivations.....	61
3.1.1	Mass Balance	61
3.1.2	Mass Flow Rate.....	62
3.1.3	Intrinsic Permeability	63
3.2	Testing Configurations	65
3.3	Transverse Strain.....	66
3.4	Results	67
3.5	Benchtop Tests	67
3.5.1	Minimum Pressure versus Number of Layers	67
3.5.2	Mass Flow Rate and Intrinsic Permeability	68
3.6	Dual-Wall Specimens.....	69
3.6.1	Initial Pressure versus Load	69
3.6.2	Mass Flow Rate and Intrinsic Permeability	70
3.6.3	Transverse Strain	72
3.7	Intrinsic Permeability versus Transverse Strain.....	77
3.8	Conclusions	78
3.9	References	80
4.	Thermal Analysis	81
4.1	Specimen Properties	82
4.2	Assumptions	82
4.3	Equations.....	83

4.4	Analysis	88
4.4.1	Emissivity, Air Pressure, and Pipe Wall Thickness.....	89
4.4.2	Low Emissivity Coatings on One or Both Surfaces	91
4.5	Conclusions	92
4.6	References	94
5.	Economic Analysis	96
5.1	Specimen Fabrication and Properties.....	97
5.2	Analytical Thermal Analysis.....	98
5.3	Heat Flux	99
5.4	Pump Properties and Serviceable Pipe Length	100
5.5	Air Flow Characterization.....	101
5.6	Abbreviations and Equations for Economic Analysis.....	102
5.7	Case Studies	103
5.7.1	Oil	104
5.7.2	Liquid Nitrogen.....	104
5.7.3	Liquefied Natural Gas.....	104
5.8	Results and Discussion.....	104
5.8.1	Oil	105
5.8.2	Liquid Nitrogen.....	107
5.8.3	Liquefied Natural Gas.....	109
5.9	Conclusions	111
5.10	References	114
6.	Conclusions.....	116
6.1	Experimental Setup:	117
6.2	Permeability:	118
6.3	Thermal Analysis:	119
6.4	Economics Conclusions:	119
6.5	Contributions.....	121
6.6	Suggested Future Work.....	121
6.7	References	123

List of Tables

Table 2-1: Dual-wall (DW) and benchtop (BT) FRPC specimen Data	37
Table 2-2: Load transfer ratios.....	51
Table 3-1: Average test data for the benchtop configuration	69
Table 3-2: Values obtained for the four layer dual-wall specimen.....	71
Table 3-3: Values obtained for the six layer dual-wall specimen.....	71
Table 3-4: Values obtained for the eight layer dual-wall specimen	71
Table 5-1: Air Flow Characteristics for Oil at 60 °C.....	102
Table 5-2: Data for 60 °C Oil	106
Table 5-3: Data for Liquid Nitrogen.....	108
Table 5-4: Data for Liquefied Natural Gas	110

List of Figures

Figure 1-1: Hydrate formation pressure versus water depth.....	2
Figure 1-2: Algorithm for testing dual-wall vacuum-insulated FRPC pipe	7
Figure 2-1: Cutaway schematic of FRPC specimen and dual-wall flanged end connection assembly showing the (a) passive flange, (b) inner tubular specimen, (c) outer tubular specimen, (d) rubber bladder, and (e) supply flange.....	20
Figure 2-2: Exploded view of the supply flange showing (a) flange, (b) outer tab, (c) inner tab with bladder, and (d) gusset plate with pressure port check valve assembly.....	21
Figure 2-3: A 38.1 mm specimen bonded to the supply flange.....	21
Figure 2-4: A 38.1 mm specimen employing (a) the alignment jig.....	21
Figure 2-5: The (b) alignment cylinder aligning the 50.8 mm specimen	21
Figure 2-6: The supply flange illustrating the (a) radial slots and (b) 3/64 inch holes	22
Figure 2-7: The supply flange illustrating the (c) 10-32 tapped hole	22
Figure 2-8: The supply flange with (a) the vacuum attachment	23
Figure 2-9: The passive flanges' gusset plate highlighting the (a) 8-32 hole, (b) o-ring grooves, and (c) bolt holes	24
Figure 2-10: The supply flanges' gusset plate highlighting the (d) face seal o-ring and (e) port check valve assembly	24
Figure 2-11: Vacuum grease is applied to the o-rings	25
Figure 2-12: The gusset plate is pressed into the supply flange	25
Figure 2-13: NUTO H 46 hydraulic fluid filling the inner tubular specimen.....	26
Figure 2-14: The gusset plate is pressed into the passive flange	26
Figure 2-15: The passive supply flange's gusset plate is tightened.....	26
Figure 2-16: Attaching the 10-32 adapter to the supply flange	27
Figure 2-17: The specimen is pressurized with air to 207 kPa.....	27
Figure 2-18: Snoop is poured over the specimen to test for leaks.....	27
Figure 2-19: The supply side attached to the testing machine.....	28
Figure 2-20: The (a) vacuum adapter attached to the (b) supply flange	29
Figure 2-21: Outline of the components of the equipment cart	31
Figure 2-22: Top view of the components of the equipment cart, including the (a) mechanical vacuum pump, (b) valve, (c) thermocouple gauge, (d) capacitance manometer, (e) differential pressure transducer, (f) steel block, and (g) test specimen, in the benchtop testing configuration	31
Figure 2-23: An aluminum block holder	32
Figure 2-24: Front view of the (a) equipment cart, (b) multi-axial testing machine, (c) specimen, and (d) vacuum adapter, in the dual-wall test configuration	32
Figure 2-25: The (a) basalt fiber creels attached to the tensioning system.....	33
Figure 2-26: The (b) routing system and (c) epoxy bath	33
Figure 2-27: Basalt fibers being placed onto a (d) rotating 38.1 mm mandrel.....	33
Figure 2-28: An installed 1.5 inch mandrel	34

Figure 2-29: FVF versus Number of Layers.....	37
Figure 2-30: Cold-cure epoxy profile used for potting specimens	39
Figure 2-31: Front Panel of the virtual instrument showing the (a) record button, (b) plot of recorded voltage changing with time, and (c) table of instantaneous voltages.....	40
Figure 2-32: Block Diagram of the virtual instrument	40
Figure 2-33: Thermocouple gauge volts to pressure conversion chart [6]	41
Figure 2-34: DP15 Voltage versus Pressure Calibration Curve	43
Figure 2-35: LM19 calibration curve.....	44
Figure 2-36: Spectral Power plot for a 1000 Hz signal	46
Figure 2-37: Filtering the four layer specimen data (BT configuration, test one)	47
Figure 2-38: Free body diagram of a dual-wall pipe subjected to uni-axial tension	48
Figure 2-39: A dual-wall FRPC specimen after performing a puncture test	53
Figure 2-40: Benchtop pressure rise data for the six layer FRPC specimen	54
Figure 3-1: Benchtop comparison of range of starting pressure (logarithmic scale) versus number of layers	68
Figure 3-2: Dual-wall comparison of initial pressure (logarithmic scale) versus applied axial load	69
Figure 3-3: A four layer dual-wall specimen, subjected to pure tensile loading, showing surface cracks in the hoop direction	72
Figure 3-4: Load and % strain versus time for the four layer specimen.....	73
Figure 3-5: Axial stress versus strain for the four layer FRPC dual-wall specimen	73
Figure 3-6: Load and % strain versus time for the six layer specimen.....	75
Figure 3-7: Axial stress versus strain for the six layer FRPC dual-wall specimen.....	75
Figure 3-8: Load and % strain versus time for the eight layer specimen	76
Figure 3-9: Axial stress versus strain for the eight layer FRPC dual-wall specimen	76
Figure 3-10: Intrinsic permeability versus transverse strain.....	77
Figure 4-1: Outline of the model	81
Figure 4-2: Thermal resistances in the model.....	83
Figure 4-3: Thermal resistance versus effective emissivity for an annulus pressure of 1.33 Pa	89
Figure 4-4: Thermal resistance versus emissivity for the six layer FRPC pipe....	90
Figure 4-5: Comparison of single and dual-wall effective emissivity coatings for six layer FRPC pipes	91
Figure 5-1: NYPC versus model parameter for oil at 60°C.....	106
Figure 5-2: NYPC versus annulus pressure for LN ₂	108
Figure 5-3: NYPC versus annulus pressure for LNG	110

Nomenclature

Greek Variables

β	Coefficient of volume expansion
γ_{12}	Global shear strain
γ_{\max}	Theoretical performance of a heat pump
γ_{xy}	Local shear strain
δ	Stretched length
ΔT	Temperature gradient
Δx	Annulus thickness
δ	Stretched length
$\underline{\varepsilon}$	Surface emissivity
$\underline{\varepsilon}^*$	Effective emissivity
ε_1	Global longitudinal strain
ε_2	Global transverse strain
$\underline{\varepsilon}_2$	Emissivity of surface 2
$\underline{\varepsilon}_3$	Emissivity of surface 3
ε_x	Local longitudinal strain
ε_y	Local transverse strain
θ	Fiber angle
μ	Dynamic viscosity
μm	Micrometer
ν	Kinematic viscosity

π	The mathematical constant Pi
ρ	Density
ρ_f	Fiber Density
ρ_m	Matrix Density
σ	Stefan-Boltzmann constant
σ_1	Global longitudinal axial stress
σ_o	Global longitudinal axial stress applied to the outer pipe
$\dot{\sigma}_A$	Applied axial load stress rate

English Variables

A_2	Outer surface area of the inner pipe
A_4	Outer surface area of the outer pipe
A_s	Heat transfer surface area
A_A	Systems effective cross-sectional area
A_i	Cross-sectional area of the inner specimen
A_o	Cross-sectional area of the outer specimen
C_e	Cost of electricity
\cos	Cosine
Cont	Continuum air flow characterization
D_i	Inner diameter
D_h	Hydraulic diameter
D_o	Outer diameter

dm/dt	Change in mass with respect to time
dP/dr	Pressure gradient across the FRPC wall
E	Energy required
E_1	Longitudinal modulus of elasticity
E_o	Outer pipes' longitudinal modulus of elasticity
E_{pipe}	Total yearly energy requirements for the pipe under study
E_{SWU}	Total yearly energy requirements for an SWU pipe
F_A	Applied load
\dot{F}_A	Loading rate
F_i	Applied load acting on the inner pipe
F_o	Applied load acting on the outer pipe
F_{cyl}	Geometric factor for concentric cylinders
g	Gravitational constant
h_{conv}	External convection heat transfer coefficient
$h_{\text{rad},2-3}$	Radiation heat transfer coefficient across the annulus
$h_{\text{rad},4-\infty}$	Radiation heat transfer coefficient for the outer pipe
k	Permeability
k'	Intrinsic Permeability
K_0	Thermal conductivity of air at room T and P
k_a	Average thermal conductivity of air
K_e	Average thermal conductivity of air
k_m	Thermal conductivity of pure resin
k_f	Thermal conductivity of basalt rock

k_p	Average thermal conductivity of the pipe wall
L	Length
L_o	Initial Length
L_{test}	Test specimen length
L_c	Characteristic length (outer diameter)
m	mass
M	Molar mass of air
\dot{m}	Mass flow rate
m_c	Mass of the composite
\dot{m}_{CO}	Contamination and outgassing mass flow rate
m_f	Fiber mass
\dot{m}_{in}	Mass flow rate of molecules entering the system
\dot{m}_k	Intrinsic permeability mass flow rate
Mlcr	Molecular air flow characterization
m_m	Matrix mass
\dot{m}_{pump}	Pump mass flow rate
\dot{m}_{SL}	Vacuum system leakage mass flow rate
\dot{m}_{test}	Measured leakage mass flow rate
\dot{m}_{out}	Mass flow leaving the system
Nu	Nusselt number
NR_T	Normalized total thermal resistance
$NYPC$	Normalized yearly power cost

P	Pressure
p	Annulus pressure
∇P	Pressure gradient
P_{env}	Environmental pressure
P_o	Minimum measured annulus pressure
Pr	Prandtl number
P_{vac}	Vacuum pressure
\dot{Q}	Heat flux
$\dot{Q}_{\text{rad},2-3}$	Radiation heat transfer rate across the annulus
R	Universal Gas Constant
r	Tube radius
r_2	Radius of surface 2
r_3	Radius of surface 3
Ra_D	Rayleigh number
$R_{\text{cond},2-3}$	Conduction resistance of the annulus
$R_{\text{cond},1}$	Conduction resistance through the inner tube
$R_{\text{cond},2}$	Conduction resistance through the outer tube
$R_{\text{conv},1}$	Thermal resistance of the working fluid
$R_{\text{conv},4-\infty}$	Convection resistance of heat transfer to the environment
r_i	Inner radius
r_o	Outer radius
$R_{\text{rad},2-3}$	Radiation resistance across the annulus

$R_{\text{rad},4\infty}$	Thermal resistance against radiation for the outer pipe
R_T	Thermal resistance of the dual-wall pipe
S	Air characterization parameter
s_o	Wall thickness of the outer pipe
\sin	Sine
T	Temperature
T_2	Surface 2 temperature
T_3	Surface 3 temperature
T_∞	Air temperature
T_a	Reference Temperature
T_f	Absolute film temperature
T_H	High boundary temperature
T_L	Low boundary temperature
T_m	Measured Temperature
$T(r)$	Temperature at a tube radius r
T_s	External surface temperature
T_{stl}	Transitional air flow characterization
\vec{u}	Velocity vector
V	Volume
V_T	Voltage
\dot{V}	Volumetric flow rate
v_c	Composite Volume
v_f	Fiber Volume

V_f	Fiber volume fraction
V_m	Matrix volume fraction
\dot{V}_{pump}	Volumetric flow rate of the pump
\dot{W}_{cycle}	Work input power of the heat pump
\dot{W}_{vp}	Work input power of the vacuum pump
$YSOU$	Yearly savings over a urethane-insulated steel pipe
$[\pm 60]_{3T}$	Six layer FRPC layup

Abbreviations

6L	Six layer
6LDW	Six layer dual-wall FRPC pipe
6LDWU	6LDW with urethane insulation covering the outer pipe
ACME	Advanced Composite Materials Engineering
BT	Benchtop
CNG	Compressed Natural Gas
CO	Carbon Monoxide
CO_2	Carbon Dioxide
CTE	Coefficient of Thermal Expansion
DW	Dual-Wall
FFT	Fast Fourier Transform
FVF	Fiber Volume Fraction

FRPC	Fiber Reinforced Polymeric Composite
HDPE	High Density Polyethylene
HTS	High-Temperature Superconducting
I	Industrial-Sized
IC	Integrated Circuit
ID	Inner Diameter
L	Large
LH ₂	Liquid Hydrogen
LIDW	Large industrial-sized dual-wall FRPC pipe
LIDWU	LIDW with urethane-insulation covering the outer pipe
LN ₂	Liquid Nitrogen
LNG	Liquefied Natural Gas
LO ₂	Liquid Oxygen
LSS	Large industrial-sized single layer steel pipe
LSSU	LSS with urethane insulation
NPT	National Pipe Thread Tapered Thread
NYPC	Normalized Yearly Power Cost
OD	Outer Diameter
PIP	Pipe-in-Pipe
RAM	Random Access Memory
S	Single layer/Steel
SPL	Serviceable pipe length
SS	Single-wall steel pipe with the 6LDW ID

SSU	SS with urethane insulation
SWU	Single-Wall Urethane-Insulated
TMC	Transverse Matrix Cracks
U	Urethane
YSOU	Yearly savings over a urethane-insulated steel pipe

1. INTRODUCTION

1.1 Background

According to reference [1], “a composite is a structural material consisting of two or more constituents that are combined at a macroscopic level and are not soluble in each other.” In this study composite tubular specimens, with $\pm 60^\circ$ plies, were created by combining basalt rock fibers and an epoxy matrix in a wet filament winding manufacturing procedure, using the Advanced Composite Materials Engineering (ACME) lab at the University of Alberta.

Composite materials have numerous advantages over conventional steels including: a high specific strength-to-weight ratio, corrosion resistance, high fatigue life, and customizable properties, e.g., coefficient of thermal expansion (CTE) by varying the material properties and fiber architecture. In addition, it is known that polyurethane liners can be intrinsically bonded to fiber reinforced polymeric composite (FRPC) pipes [2], and their properties can be tailored for specific applications, e.g., low permeability (high density), abrasion resistance, and low emissivity coatings [3]. Furthermore, it is possible to design FRPC pipe with a near-zero axial CTE by varying the material properties (e.g., Aramid fibers have a negative CTE), and winding angle.

Conventional Pipe-in-Pipe (PIP) designs are manufactured from 304L stainless steel or Invar [4] for applications in the energy sector including deepwater gas extraction. Some of the challenges associated with current deepwater PIP (dual-wall) applications include: ice formation around joints and

bulkheads [5], salt water corrosion of the steel pipe [4], and formation of hydrates [6]. A deepwater gas pipeline is particularly vulnerable to hydrates, which are ice-like crystals formed from water and light hydrocarbons when pressure and temperature conditions encourage agglomeration inside the transfer pipeline, thus blocking the flow path [6]. Ocean water has a predictable temperature at specific depths [6], while hydrate formation for deepwater gas occurs at predictable temperatures and pressures [6]. Combining the graphical data from [6], i.e., water depth versus environmental temperature of deepwater, and pressure versus temperature for hydrate formation, allows for the creation of Figure 1-1, which illustrates the maximum gas pressure that can be employed at a particular water depth (fluid temperature) to avoid hydrate formation, assuming the fluid and environmental temperatures are tantamount. Note that a deepwater well would have a tapped pressure exceeding 40,000 kPa [6] at a depth exceeding

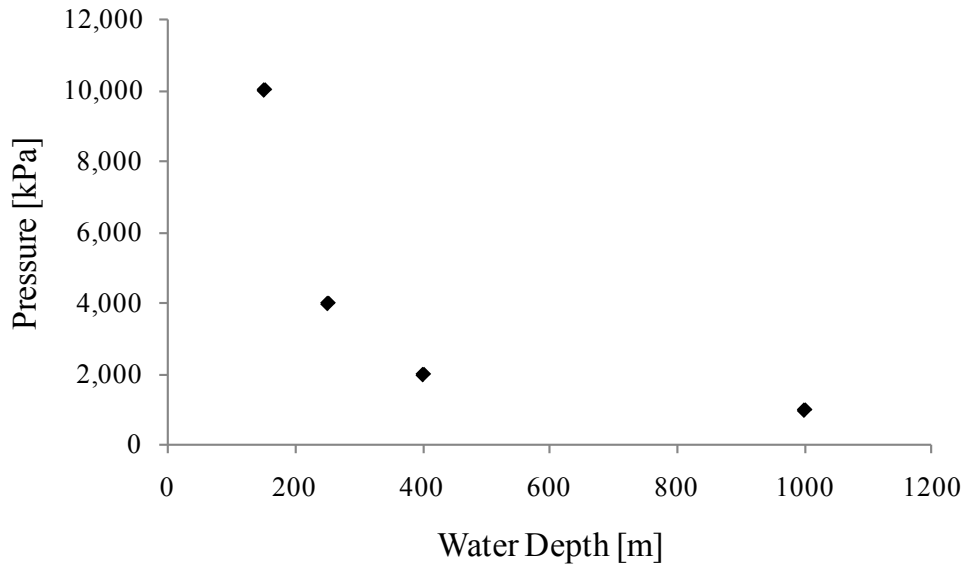


Figure 1-1: Hydrate formation pressure versus water depth

1,000 m [6], which represents optimal hydrate formation conditions. Consequently, measures need to be taken to avoid hydrate formation, which include: adding hydrate inhibitors (salt) [6], or increasing pipe thermal resistance.

Other applications also require thermal management, e.g., the transportation and storage of liquefied natural gas (LNG), liquid nitrogen (LN_2), and oil slurries require a high thermal resistance to avoid fluid boiling (LNG, LN_2), formation of hydrates [6], or solidification of the fluid (oil slurries), to ensure flow assurance. Furthermore, LNG transportation lines must be robust and reliable, as the high capital costs necessitate a low risk and high flow assurance tolerance [7]. LNG pipe is typically made from 304L stainless steel, which has a positive coefficient of thermal expansion (CTE), and requires bellows expansion joints to compensate for the axial expansion arising from the high temperature gradient (LNG at -160 °C and the surrounding environment) [7], and is susceptible to corrosion and abrasion.

FRPC pipe may be superior to metallic pipe for applications requiring thermal management, or corrosion and abrasion resistance. The utilization of a near-zero axial CTE, or application of corrosion and abrasion resistant liners allow FRPC piping to eliminate bellows expansion joints, and decrease premature wear, respectively. Furthermore, dual-wall FRPC pipe employing vacuum insulation improves thermal resistance, and flow assurance, thus decreasing the likelihood of hydrate formation, fluid solidification, and fluid boiling.

1.2 Outline

This study is broken down into four major chapters, including Experimental Setup, Permeability, Thermal Analysis, and Economics, which work collectively to highlight the economic viability of vacuum insulation for dual-wall FRPC specimens.

Basalt/epoxy fiber reinforced polymeric composite (FRPC) pipes were tested in order to determine their suitability for applications requiring vacuum insulation. An experiment was designed to test FRPC tubular specimens that were manufactured using mandrels with 38.1 mm (1.5 inch) and 50.8 mm (2 inch) inner diameter (ID), in a concentric dual-wall setup, and also in a single-wall benchtop setup. Two end connection designs, i.e., single-wall benchtop and dual-wall flanged, were manufactured to measure the through wall air leakage mass flow rate of various FRPC tubular specimens. An equipment cart that provides vacuum and measures and records annulus pressure, environmental pressure, and temperature was assembled for easy transition between setups.

The measured pressures and temperatures were converted into mass flow rates (air leakage rate), and intrinsic permeability coefficients for comparison. The benchtop setup measures the minimum achievable pressure and air leakage rate for a theoretically undamaged FRPC specimen, while the dual-wall setup measures the parameters for specimens subjected to tensile axial traction loading conditions, simulating an FRPC specimen under use. The two test setups allow for the experimental optimization of FRPC tubular specimens for vacuum holding

capability, by changing various conditions, i.e., the number of layers in the FRPC, the load applied, the FRPC manufacturing materials, and intrinsically-bonded high-density coatings.

A theoretical thermal analysis was performed with the goal of creating a generalized model useful for various case studies involving fluids flowing through the center of dual-wall FRPC pipes, i.e., oil, liquid nitrogen (LN_2), and liquefied natural gas (LNG). The boundary conditions are adjustable for the various case studies, i.e., FRPC pipe diameter, vacuum pressure, emissivity, wall thickness, material properties (FRPC and working fluid), and temperatures of the environment and working fluid. The thermal resistance and heat flux can be determined for each case study, and boundary condition, and be input into the economic analysis section to generate an economic viability comparison.

An economic analysis was performed for each of the aforementioned case studies with the goal of determining the economic viability of FRPC pipe over urethane foam-insulated single-wall steel pipe. The heat flux (gain or loss) is converted into electricity for direct comparison between case studies, by assuming a heat pump compensates for the heat flux (gain or loss) over the temperature gradient between the environment and the working fluid. In addition, an FRPC pipe employing vacuum insulation requires a vacuum pump to run continuously, which adds to the total electrical requirement. Furthermore, the serviceable pipe length (SPL) maintained by each mechanical vacuum pump is directly proportional to the target pressure, i.e., the SPL is calculated as the length corresponding to the situation where the measured leakage air mass flow rate

equals the vacuum pumps discharge mass flow rate, at the required annulus pressure. The Economics chapter combines the results of the Permeability and Thermal Analysis chapters to provide a consolidated model for evaluating the economic viability of vacuum-insulated dual-wall FRPC pipe for three specific case studies, i.e., 60 °C oil, LN₂, and LNG.

1.3 Flow Chart

A flow chart of the work performed in the study is shown in Figure 1-2, which features an algorithm for testing the suitability of various FRPC materials and liners on the through-wall air leakage mass flow rate of dual-wall FRPC vacuum-insulated pipe systems. A literature review was initiated to find possible applications for dual-wall FRPC pipe, and to learn of any previous work involved in measuring through wall air leakage mass flow rates of FRPC pipe. Two end connection systems, i.e., single-wall benchtop and dual-wall flanged, were designed and built, and the manufactured basalt/epoxy FRPC tubular specimens were installed to ascertain the difference in air leakage behavior between damaged and undamaged FRPC pipe. Vacuum holding capability experiments were performed to measure the annulus pressure rise, and the resulting data was employed to calculate the air leakage mass flow rate, and intrinsic permeability. The heat flux was determined utilizing the analytical model developed for the dual-wall specimens, based on the measured minimum achievable annulus pressure. The economic viability was determined from the calculated heat flux, minimum achievable annulus pressure and material properties, and the resulting

yearly electrical costs were compared with urethane foam-insulated single-wall steel pipe for each case study.

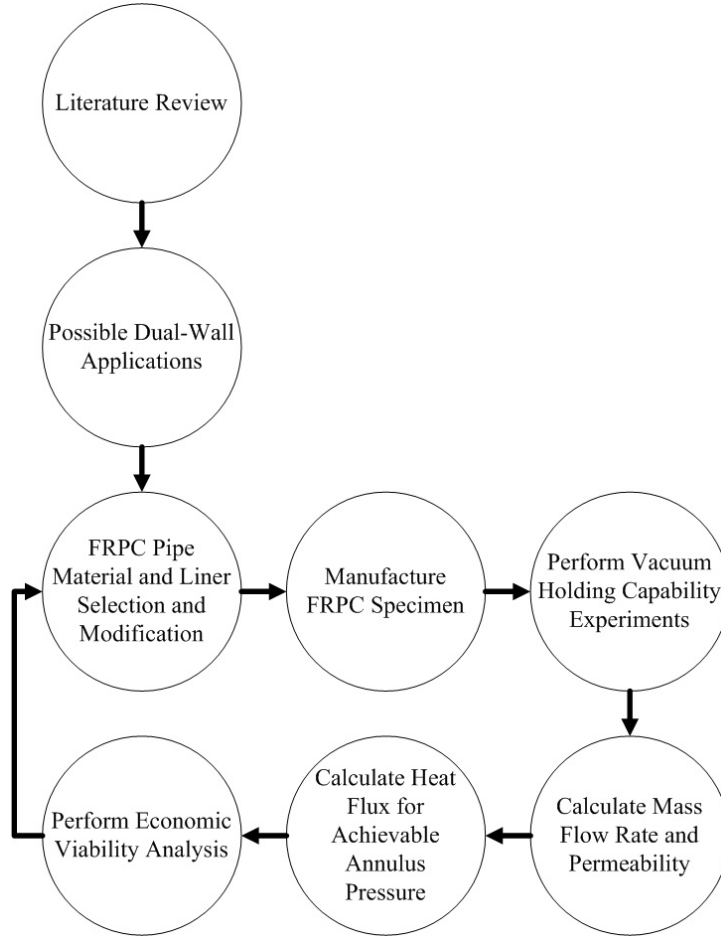


Figure 1-2: Algorithm for testing dual-wall vacuum-insulated FRPC pipe

1.4 Possible Applications

1.4.1 High-Temperature Superconducting Cables

Composites have numerous structural and material advantages over conventional steel pipelines including application of abrasion resistant

polyurethane liners [2], near-zero axial thermal expansion*, high corrosion resistance, high strength to weight ratio, and customizable strength properties. However, are FRPC pipes economically viable for technological applications requiring a high level of thermal resistance? One possible dual-wall or multi-wall concentric tubular pipe application is high-temperature superconducting (HTS) cables [8]. One of the designs involves three concentric pipes in a triaxial Pipe-in-Pipe arrangement [9], whereby various dielectric lines and shields are surrounded by inner and outer layers of LN₂. An additional benefit of FRPC pipes over conventional steel invokes the near-zero axial thermal expansion capabilities. When homogenous materials, i.e., the steel pipes, are heated (or cooled) they expand (or contract) axially. In a pipeline, axial expansion can apply large stresses to joints, leading to system failures. However, FRPC specimens designed with near-zero axial thermal expansion would alleviate these issues.

An obstacle preventing the utilization of concentric tubes in a horizontal placement is maintaining a consistent annular space around the pipes. A dual-wall system consisting of unsupported concentric tubes will have the inner tube naturally sit on the inside surface of the outer tube, which creates a conduction surface for heat transfer. One method of circumventing this loss is to use a low loss spacer with reflecting foils [10]. By combining corrugated, longitudinal welded stainless steel inner tubing, 30 layers of super insulation (aluminum coated foil with fleece spacers), low loss spacers, and additional corrugated stainless steel outer tubing, a 1.33×10^{-3} Pa (10^{-5} Torr) vacuum space was created,

* Note: near-zero axial thermal expansion FRPC tubular specimens can be manufactured by selecting fiber and matrix phases with appropriate thermal properties, along with the weave angle.

which aids in decreasing the heat flux from 10 to 5 W/m² [10]. An additional requirement of any HTS cable is either flexibility for easy shipping [10], or a continuous on-site extrusion manufacturing process. One of the benefits of composite pipes is the ability for continuous extrusion, particularly with a protrusion process. Thus, if a composite piping system can be developed that has a heat flux of 5 W/m² or less for LN₂; it can be a viable alternative to stainless steel tubing for HTS cables.

1.4.2 Liquefied Natural Gas

Another possible application of dual-wall or multi-wall concentric pipes is for transporting LNG. Liquefied or compressed gases can be transported by lot in insulated containers called Dewar, or by flow through insulated piping [11]. Cryogens are frequently transferred for short distances, as longer distances require substantially more insulation [11]. Heat fluxes for an un-insulated liquid H₂ line is typically around 11 kW/m² for still air surrounding the pipe, and 19 kW/m² for wind with a velocity of 6.7 m/s [11]. Insulations including fiber glass [11], polystyrene foam [11], polyurethane foam [11], and liners including high density polyethylene (HDPE) [12], and polyurethane [2] can be employed to further decrease the heat flux.

LNG is often transported from production facilities in hazardous environments, by ship, to storage facilities. LNG, when utilized for ship-to-shore transfers, consists of 90% methane, is cooled to -161 °C, and is stored and transported at atmospheric pressure [13]. Pipes are designed for a variety of ship

to tank situations and lengths, i.e., subsea flow lines, depending on the location of the marine terminal relative to the storage tanks [13]. Comparing various pipeline designs it was found that 9% Ni steel pipes with vacuum or aerogel insulation is the most economical method [13]. However, the aerogel insulation is preferred as it has low maintenance relative to the vacuum insulation [13]. Therefore, if a leak-free dual-wall FRPC tubular specimen is developed, aerogel insulation could be used to maintain concentricity in a horizontal arrangement, and further increase thermal resistance.

1.4.3 Hydrogen Pipeline

A hydrogen-based economy is one of the current research areas, and it is based upon the transport of hydrogen for use as a fuel. Pipelines have historically been constructed using various carbon steels, which are susceptible to the negative effects of hydrogen, i.e., hydrogen embrittlement, hydrogen-assisted cracking, strain-rate embrittlement, hydride formation, hydrogen blistering, and high temperature effects [14]. Hydrogen flowing through a steel-chromium or steel-molybdenum alloy pipe may lead to weakening and crack formation by the permeation of hydrogen into the crystal lattice, and resultant dissolution [14]. This weakening could potentially lead to pipe failure. However, a dual-wall composite wrapped steel alloy pipe would maintain the hydrogen permeability resistance and the structural strength of the composite [14]. Furthermore, if dual-wall composite pipes can be manufactured with non-metallic hydrogen resistant liners they would alleviate the use of steel alloy pipes for liquid hydrogen (LH_2) applications.

1.4.4 Cryogenic Fluid Storage Tanks

Additional applications for composite technology involving gas holding capability and cryogenic fluid storage include: oxygen holding tanks for space transportation (shuttles), civil aircraft, and land vehicles [15]. Civil transport vehicles can use cryogenic fluids as fuels, i.e., LH₂, and compressed natural gas (CNG), while spacecraft can use liquid oxygen (LO₂) as an oxidizer or a ‘fuel’ (for space transport) [15]. Current economics make only the space applications relevant due to the mass savings and thermo-mechanical properties of the composites outweighing the additional material costs [15]. However if the leakage of air, represented as oxygen and nitrogen, through composites can be improved, for inexpensive composite materials, civil aircraft and land vehicles may become viable economic options for cryogenic fuel holding tanks.

1.4.5 Oil Slurries

Another possible application involves transporting multi-phase fluids, i.e. oil slurries, in FRPC pipes. An intrinsically-bonded polyurethane-basalt/epoxy FRPC pipe is resistant to abrasion from the oil slurry, and will not wear as quickly as uncoated steel pipes [2]. However, multi-phase fluid slurries may solidify if they are not periodically heated when transported over large distances under cold environment conditions. A polyurethane-lined dual-wall vacuum insulated pipe would invoke abrasion and thermal resistance, decreasing maintenance and re-heating costs, respectively.

1.5 Effects of FRPC Properties on Vacuum Pressure

The thermal resistance benefits of vacuum insulation depend on the quantity (pressure) of the remaining constituent gas molecules in the evacuated system, which are directly related to (i) the influx through-wall air leakage mass flow rate, and (ii) the expulsion mass flow rate of a continuously operating vacuum pump. Various methods are explored to decrease the influx through-wall air leakage mass flow rate of FRPC tubular specimens, which include: density, fiber volume fraction (FVF), void fraction, and ply thickness.

1.5.1 Density

Dominguez and Rivera [16] found that at high matrix densities, with the Lennard-Jones potential mathematical model describing the molecular interactions, there is an apparent competition between the high density diffusing material and the repulsion between the constituent particles of the matrix. This leads to the diffusion coefficient being lower in a high density matrix compared to its low density counterpart [16], and provides a method of decreasing the leakage rate for undamaged specimens, i.e., by increasing the density of the matrix phase in FRPC tubular specimens.

1.5.2 Fiber Volume Fraction

Disdier et al. [17] found that glass fiber composites loaded at room temperature show no modification of helium permeation, except for applied stresses near failure. The proposed failure mechanisms in [17] elucidate three

loading responses: (i) enclosed damage between laminates, (ii) external or internal surface damage, or (iii) through-specimen damage. Loads resulting in localized enclosed damage between laminates or in surface damage may have the effect of changing the slope of the permeability curve, although not significantly [17]. Through-specimen damage is the only mechanism that results in gas permeation without diffusion [17], and occurs for loads nearing failure [17], and henceforth it is expected that basalt/epoxy dual-wall FRPC pipe will show similar increases in air leakage mass flow rate near failure. In addition, it was found that increasing the FVF decreases the permeability of glass fiber composites by (i) ensuring the fluid must pass through reduced volumes of polymer matrix phase embedding, i.e., the impermeable glass fibers [17], and (ii) increasing the FRPC failure strength. Thus, one method of decreasing the air leakage mass flow rate is to increase the FVF while increasing the FRPC failure strength, thereby decreasing the probability of through specimen damage at loads not nearing failure.

1.5.3 Void Fraction

Evans and Reed [18] found that composite void content plays a significant role in increasing the flow rate of gas passing through a resin based composite panel. However, the composite panel was impermeable to carbon monoxide (CO) and carbon dioxide (CO₂), and it was reasoned that CO and CO₂ bond to the reactive groups formed during the reaction mechanism of epoxide resins with anhydride curing agents in the polymer structure of the particular matrix phase employed by [18]. While the epoxy utilized in the current study lacks the reactive groups necessary for molecular adherence, and thus maintains CO and CO₂

permeability, the results of [18] raise the design consideration that leakage rate can be temporarily diminished by employing reactive groups in the matrix phase specific to the permeating fluid.

1.5.4 Ply Thickness

Noh et al. [19] developed a numerical computational fluid dynamics model using FLUENT that determined leakage through transverse matrix cracks (TMC), and found that reducing ply thickness is significant in reducing the leakage rate of cryogenic fuel. Thinner plies lead to fewer interconnecting TMC and delamination areas in the damage network (expressed as a function of crack density) of a composite structure, resulting in fewer interconnecting pores which thus decrease leakage due to permeability [19]. This result agrees with [17], and suggests increased winding tension for basalt/epoxy FRPC tubular specimens will lead to thinner laminates, and specifically to a reduction of the air leakage rate.

1.6 Apercu

In this thesis, Experimental Setup, Permeability, Thermal Analysis, and Economics chapters follow, and are used to identify a monetary benefit of employing dual-wall FRPC pipe for LNG, LN₂, and oil slurry applications. Although the present study is not a validation of a specific FRPC dual-wall design for a particular application, it is an indication of the efficacy of dual-wall vacuum-insulated FRPC piping for said applications. Furthermore, the experimental setup and resulting data analysis sections provide a baseline that can be used for improving the leakage characteristics of FRPC piping.

1.7 References

- [1] Kaw, AK. Mechanics of Composite Materials. 2nd ed. Boca Raton: CRC Press; 2006.
- [2] Juss K, Mertiny P. Fabrication and Performance of a Novel Polyurethane-Lined Fiber-Reinforced Composite Pipe. Proc. Canadian Society for Mechanical Engineering Forum; Ottawa; 2008.
- [3] Yan X, Xu G. Corrosion and mechanical properties of polyurethane/Al composite coatings with low infrared emissivity. *J Alloys Compd.* 2010;491:649-653.
- [4] McKinnon, C. Technical Challenges of Subsea LNG Pipelines. Society for Underwater Technology [homepage on the Internet]. London, UK: SUT; c2009 [updated 2007 Mar 22; cited 2010 Mar 31]. Available from: http://events.sut.org.uk/past_events/2007/070322/LNGpipeline.pdf
- [5] Gallet, I. Technical Challenges of Subsea LNG Pipelines. Report on SUT London Evening Meeting. Society for Underwater Technology [homepage on the Internet]. London, UK: SUT; c2009 [updated 2007 Mar 22; cited 2010 Mar 31]. Available from: http://events.sut.org.uk/past_events/2007/070322/report.pdf
- [6] Morgan, JEP. Deepwater Gas What's the problem? Society for Underwater Technology [homepage on the Internet]. London, UK: SUT; c2009 [updated 2006 Apr 26; cited 2010 Mar 31]. Available from: http://events.sut.org.uk/past_events/2007/070426_oz/Morgan.pdf

- [7] Brown T, Jukes P, Sun J. Mechanical Design of Subsea and Buried LNG Pipelines. In: Proceedings of the Offshore Technology Conference; 2009 May 4-7; Houston, Texas, USA. 2009 Offshore Technology Conference [homepage on the Internet]. Houston, Texas, USA: Offshore Technology Conference; c2006-2010 [cited 2010 Mar 31]. Available from:
<http://www.otcnet.org/2009/pages/schedule/documents/otc202261.pdf>
- [8] Superconductivity for Electric Systems 2005 Annual Peer Review [homepage on the Internet]. Washington, DC: U.S. Department of Energy; [updated 2005 Aug 2-4; cited 2010 Feb 23]. Available from:
<http://www.hptspeerreview.com/2005/>
- [9]. High Temperature Superconducting Cable for Power Transmission Applications. WAMS 2004 Workshop on Accelerator Magnet Superconductors; March 22 – 24; Archamps, France; 2004.
- [10] Schippl K. Very Low Loss Cryogenic Envelope for long HTS-cables [homepage on the Internet]. [Cited 2010 Jan 26]. Available from:
<http://www.cryo-schippl.de/Transmag.pdf>
- [11] Shah RM, Savalia SC, Mehta RN. Theoretical thermal performance of a vacuum insulated liquid hydrogen transfer line. Indian Vacuum Society National Symposium; 2005 November 16 – 18; Gandhinagar, Gujarat, India.
- [12] Kim BS, Kim BH, Kim JB, Joe CR. Study on the development of composite CNG pressure vessels. *Cryogenics*. 1998;38:131-134.

- [13] Kinney B, Prescott N, Zhang J. Comparison of LNG Transfer Solutions Between Ship and Tank. Presentation to SNAME/MTS Joint Meeting; 2008 Mar 28; Texas A&M University.
- [14] Hayden LE, Tverberg JC. Materials in support of a newly emerging Hydrogen infrastructure. In: Flaw Evaluation, Service Experience, and Materials for Hydrogen Service, ASME PVP, Vol. 475 July 25-29; San Diego, California USA; 2004. PVP2004-2562.
- [15] Heydenreich R. Cryotanks in future vehicles. *Cryogenics*. 1998;38:125-130.
- [16] Dominguez H, Rivera M. Studies of porosity and diffusion coefficient in porous matrices by computer simulations. *Mol Phys*. 2002;100(24):3829-3838.
- [17] Disdier S, Rey JM, Pailler P, Bunsell AR. Helium permeation in composite materials for cryogenic applications. *Cryogenics*. 1998;38:135-142.
- [18] Evans D, Reed RP. The permeability of resin based composite materials to radiolytic gases. *Cryogenics*. 1998;38:149-154.
- [19] Noh J, Whitcomb J, Peddiraju P, Lagoudas D. Prediction of Leakage Rate through Damage Network in Cryogenic Composite Laminates. Proceedings of the 45th AIAA/ASME/ASCE/AHS/ASC Structures, Structural Dynamics & Materials Conference; 2004 April 19-22; Palm Springs, California, USA. AIAA 2004-1861.

2. EXPERIMENTAL SETUP^{*}

In order to determine the economic viability of vacuum insulation, various measurements needed to be performed on the dual-wall fiber reinforced polymeric composite (FRPC) specimens, i.e., the minimum pressure attainable in the annulus, the leakage rate of air, and the effect of an applied load on the leakage rate. Two different tubular specimen holding flanged end connections were designed to test the FRPC specimens, i.e., dual-wall and single-wall scenarios. The dual-wall flanged end connection design invokes the multi-axial testing machine to measure the effect of load on leakage rate. The single-wall design is useful for determining the minimum pressure attainable for undamaged specimens. The FRPC specimens consist of two pipes, an inner pipe with a 38.1 mm (1.5 inch) inner diameter (ID), and an outer pipe with a 50.8 mm (2 inch) ID. Three sets of FRPC specimens were wet filament wound with a fiber architecture of $\pm 60^\circ$, consisting of four, six, and eight layers.

2.1 Dual-Wall Flanged End Connections

The dual-wall flanged end connection system was developed to test the effect of various load scenarios on the suitability of vacuum insulation. The highlights of the dual-wall flanged end connection include:

- Application of the 38.1 mm ID ‘inner’ tubular specimen

^{*}A version of this chapter was published in the Proceedings of the 28th International Conference on Ocean, Offshore and Arctic Engineering, OMAE 2009, Honolulu, Hawaii, USA [1].

- Application of the 50.8 mm ID ‘outer’ tubular specimen
- Total installed length of 203.2 mm (8 inches)
- 101.6 mm (4 inch) gauge length
- Vacuum applied directly to the annulus
- Sealable ports for wiring allow for strain measurement in the annulus, while maintaining a vacuum seal
- Machined from 4340 steel
- Re-useable by removing the potting epoxy and FRPC pipe through a ‘burn out’ procedure, i.e., burning off the epoxy in an oven for three hours at 538 °C (1000°F)
- Suitable for compression, tension, internal and external pressurization loadings.

2.1.1 Flanged End Connections

The dual-wall flanged end connections have two unique sides, each with a different intention. The supply flange allows for application of the vacuum system located on the equipment cart to the annulus, and internal pressurization of the inner specimen, while the passive flange ensures containment of the pressurized fluid. Both flanges allow for the sample to be connected to the multi-axial testing machine through a gusset plate. A cutaway schematic of the flanged end connection assembly is shown in Figure 2-1. In addition, both sides are composed of three concentric specimen holders that are assembled using an interference fit,

i.e., a flange, an outer tab, and an inner tab, which is shown in Figure 2-2. The purpose of the rubber bladder, shown in Figure 2-1 and Figure 2-2, is to limit possible fluid leaking into the annulus during internal pressurization.

The inner tab of the supply flange was designed so the inside of the inner tubular specimen rests against the tabs outer surface, which aids in alignment, as shown in Figure 2-3. A second alignment cylinder fits over the alignment jig, to ensure the inner tubular specimen is properly aligned in the flanged end

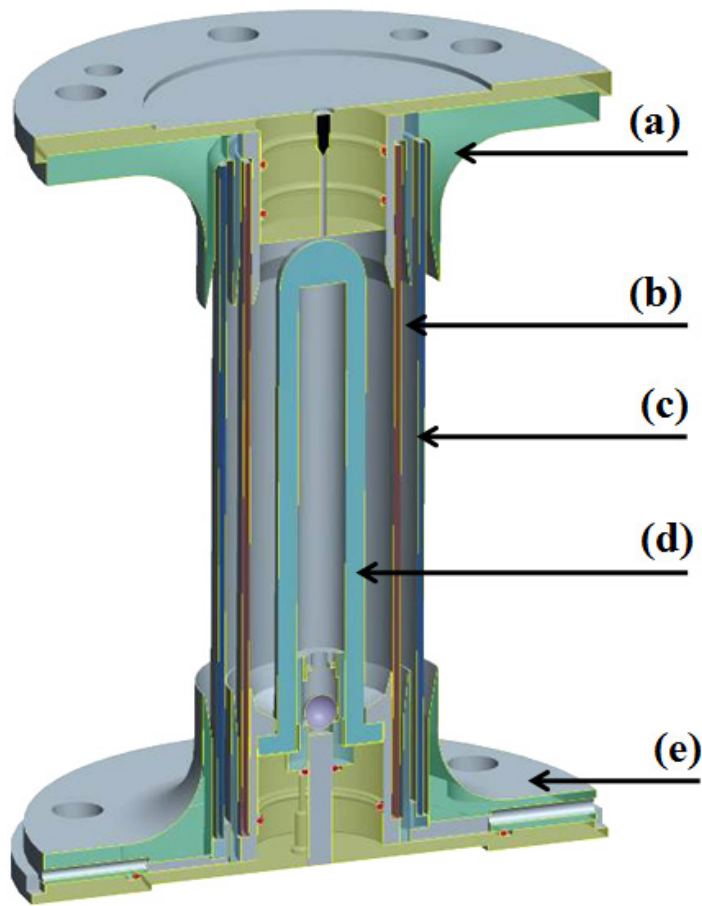


Figure 2-1: Cutaway schematic of FRPC specimen and dual-wall flanged end connection assembly showing the (a) passive flange, (b) inner tubular specimen, (c) outer tubular specimen, (d) rubber bladder, and (e) supply flange

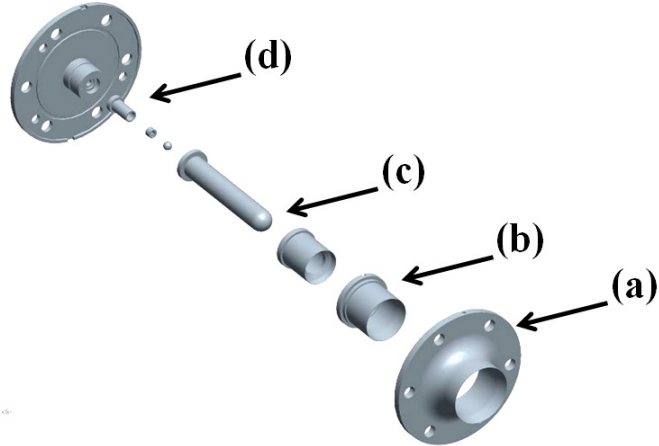


Figure 2-2: Exploded view of the supply flange showing (a) flange, (b) outer tab, (c) inner tab with bladder, and (d) gusset plate with pressure port check valve assembly



Figure 2-3: A 38.1 mm specimen bonded to the supply flange



Figure 2-4: A 38.1 mm specimen employing (a) the alignment jig



Figure 2-5: The (b) alignment cylinder aligning the 50.8 mm specimen

connections, shown in Figure 2-4. Cold cure epoxy is employed to bond the inner tubular specimen to the outer tab.

A lip on the outside of the outer tab of the supply flange is used to ensure the bottom of the outer tubular specimen is concentric with the supply flange. In addition, an aluminum alignment cylinder, shown in Figure 2-5, ensures the top of

the outer tubular specimen is concentric with the inner tubular specimen. Cold cure epoxy is applied to bond the outer tubular specimen to the flange when proper alignment of the specimens is achieved.

A single 3/64 inch hole was drilled into the outer tabs' lip, which is used as a port to apply vacuum to the annulus. A radial slot on the bottom of the supply flange, shown in Figure 2-6, intersects with the 3/64 inch hole, and also with a 10-32 threaded hole drilled from the top of the supply flange, shown in Figure 2-7. The vacuum pump is connected through a 1/4 inch stainless steel tube that attaches to a Swagelok adapter, shown in Figure 2-8, which fits into the 10-32 hole.

Two additional 3/64 inch holes were drilled on the opposite side of the outer tabs lip to allow passage of the strain gauge wires outside of the annulus. The strain gauge wires fit through the holes, and are passed through a radial slot in the

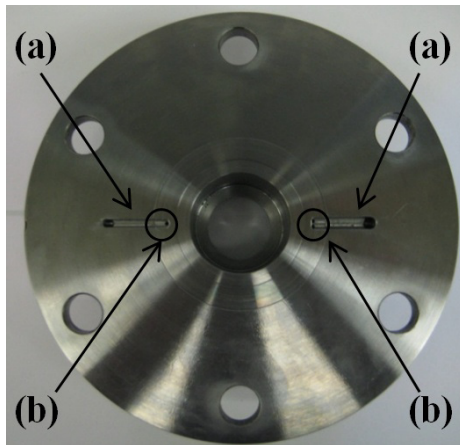


Figure 2-6: The supply flange illustrating the (a) radial slots and (b) 3/64 inch holes

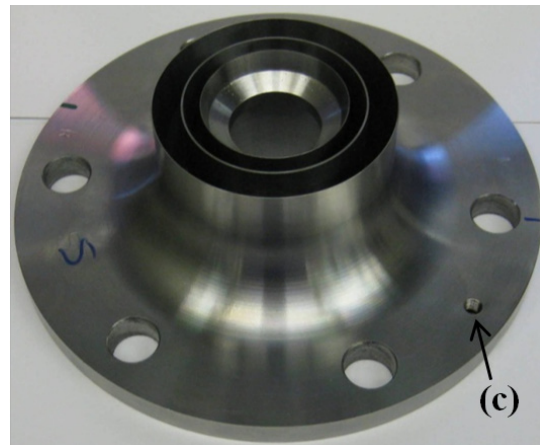


Figure 2-7: The supply flange illustrating the (c) 10-32 tapped hole

supply flange, shown in Figure 2-6. 3M DP-460 epoxy adhesive is poured into the slot during assembly, and allowed to cure, which ensures a vacuum tight seal.

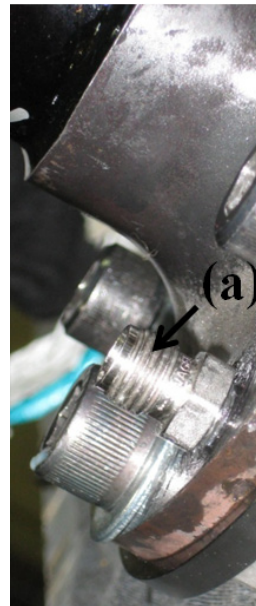


Figure 2-8: The supply flange with (a) the vacuum attachment

The two flanges are attached to the multi-axial testing machine through the gusset plates, and six hex-key bolts. The extrusion in the center of the passive flanges' gusset plate has two o-rings, which ensure pressurized oil is sealed inside of the inner tubular specimen from the passive side. In addition, an o-ring on the supply flanges' gusset plate and an additional o-ring on the face of the gusset plate ensures oil is sealed from the supply side.

The multi-axial testing machines load piston has a lip that fits into the back of the gusset plates, which ensures proper alignment in the machine. In addition, an 8-32 hole was drilled into the centre of the passive gusset plate and fitted with

a screw, to facilitate bleeding of air when the specimen is filled with oil. The passive flanges' gusset plate is shown in Figure 2-9.

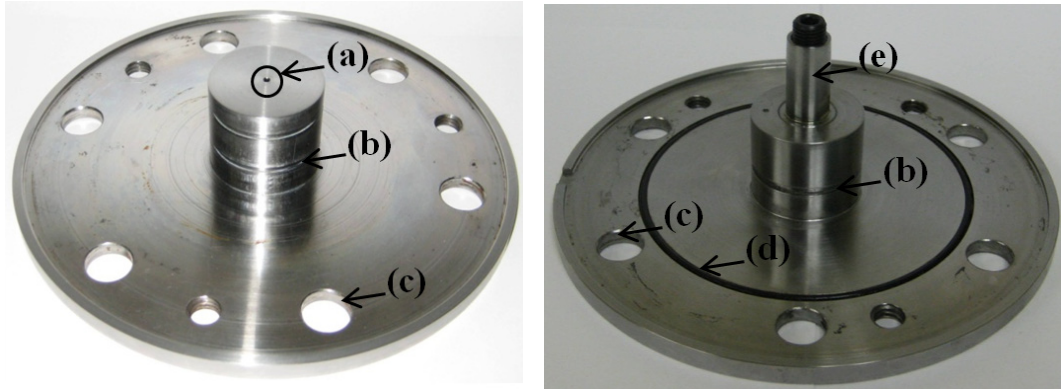


Figure 2-9: The passive flanges' gusset plate highlighting the (a) 8-32 hole, (b) o-ring grooves, and (c) bolt holes

Figure 2-10: The supply flanges' gusset plate highlighting the (d) face seal o-ring and (e) port check valve assembly

The supply flanges' gusset plate, shown in Figure 2-10, contains the same extrusion as the passive flanges' gusset plate, except it has a single extrusion o-ring to compliment a face seal o-ring. The face seal o-ring keeps pressurized oil, that may leak past the extrusion o-ring, from reaching the vacuum port.

The oil injector is applied to the flanged end connections through an oversized $\frac{1}{4}$ inch hole, that was drilled through the center of the supply flanges' gusset plate. A check valve consisting of a steel ball, spring, and hex screw was placed at the top of the supply flanges' gusset plate. The bladder fits over the check valve, and is pressurized by the oil injector during testing. An o-ring seal ensures pressurized oil does not leak into the vacuum port.

2.1.2 Testing Assembly and Installation

Once the inner and outer tubular specimens are bonded to the flanged end connections, the assembly must be prepared for installation into the multi-axial testing machine. The first step is to apply a coating of Dow Corning vacuum grease to the o-rings, shown in Figure 2-11. The rubber bladder is then fitted to the supply flanges' gusset plate, which is then pressed into the supply flange shown in Figure 2-12. Six hex-head bolts, twelve washers and six nuts are used to tighten the gusset plate to the flange. Next the inner tubular specimen is filled with oil, shown in Figure 2-13, the 8-32 hole in the passive flanges' gusset plate is removed, and the gusset plate is pressed into the passive flange, shown in Figure 2-14. Excess oil is squeezed out through the small bleed hole, as an additional six hex-head bolts, twelve washers, and six nuts are used to tighten the gusset plate to the flange, shown in Figure 2-15. The 8-32 screw on the passive flanges' gusset plate is then tightened, and the oil injector is used to fill the bladder on the supply flange with oil.



Figure 2-11: Vacuum grease is applied to the o-rings



Figure 2-12: The gusset plate is pressed into the supply flange



Figure 2-13: NUTO H 46 hydraulic fluid filling the inner tubular specimen



Figure 2-14: The gusset plate is pressed into the passive flange

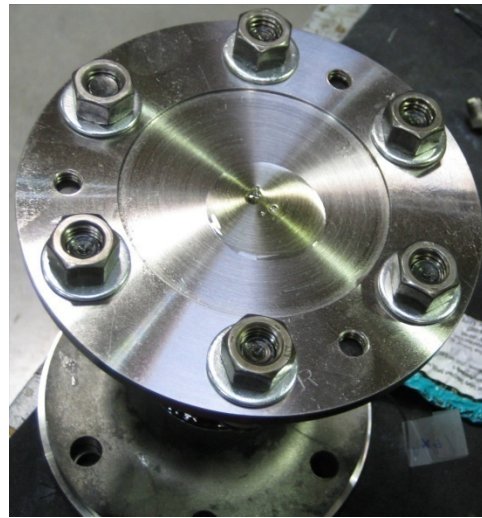


Figure 2-15: The passive supply flange's gusset plate is tightened

2.1.3 Vacuum Adapter Assembly and Testing

The face of the supply flange is covered with vacuum grease (Dow Corning), and a $\frac{1}{4}$ inch tubing to 10-32 adapter, shown in Figure 2-16, is fitted into the 10-32 threaded hole. A face seal and an o-ring fit between the adapter and the hole to ensure a leak free junction.



Figure 2-16: Attaching the 10-32 adapter to the supply flange



Figure 2-17: The specimen is pressurized with air to 207 kPa.

Figure 2-18: Snoop is poured over the specimen to test for leaks.

Testing of the 10-32 adapter for leakage involves pressurizing the annulus with air at 207 kPa (30 psi), and spraying Snoop over the junction. The joint is tightened until bubbles no longer appear. A figure illustrating the Snoop testing procedure is shown in Figure 2-17, and Figure 2-18.

Once the specimen is determined to be leak-free, the bolts, nuts and washers are removed from the supply side, which is then fitted to the multi-axial testing machine using six bolts, as shown in Figure 2-19.



Figure 2-19: The supply side attached to the testing machine.

The bolts, washers and nuts are then removed from the passive side. The multi-axial testing machine is turned on, the MTS controller integrators are turned off (to slow the response time of the controller), and the machine piston is moved into contact with the passive side. The piston is rotated until the bolt holes are aligned. Then a slight compressive load is applied, and the bolts are installed. The integrators are reset, and the MTS controller is ready for testing.

2.2 Vacuum Pump and Measuring Devices

Installation

The next step in the installation process is to connect the vacuum system located on the equipment cart, which includes the measuring devices, and a

mechanical vacuum pump. The cart is rolled next to the testing machine, and a custom-bent $\frac{1}{4}$ inch OD stainless steel tube is connected to the 10-32 adapter as shown in Figure 2-20.

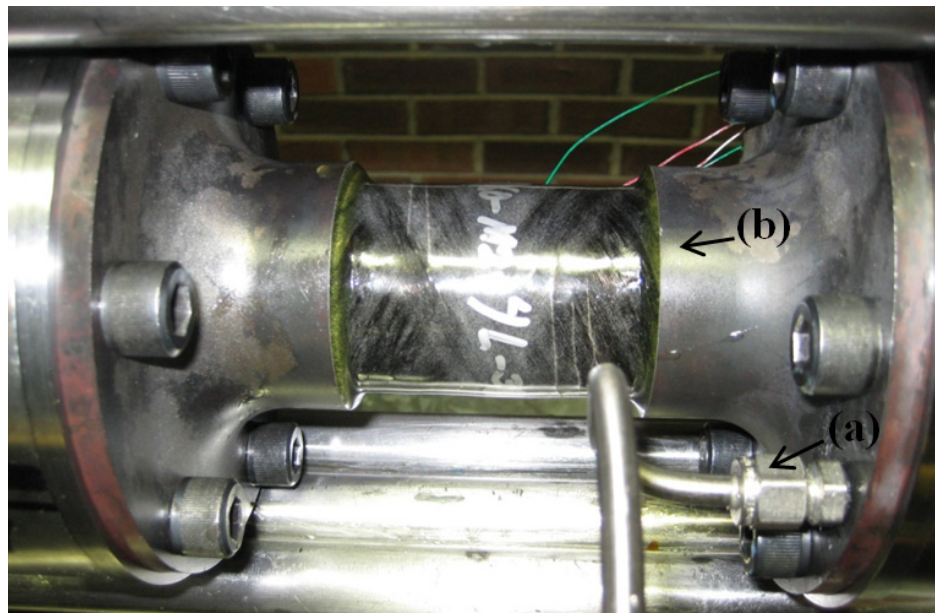


Figure 2-20: The (a) vacuum adapter attached to the (b) supply flange

The equipment cart is used for dual-wall tests in the multi-axial testing machine, or for long term benchtop tests. Figure 2-21 outlines the components, and Figure 2-22 shows a top view of the equipment cart. The pump is a Leybold-Heraeus Trivac D8A dual stage rotary vane mechanical vacuum pump [2]. It is connected to $\frac{1}{4}$ inch OD, 0.035 inch wall, 304 stainless steel tubing (Swagelok: 304L-T4-S-035-20) through an aluminum vacuum adapter and a $\frac{1}{4}$ inch tubing to 1/8 inch NPT male connector (Swagelok: SS-400-1-4). Note that whenever an NPT fitting is employed, Jet-Lube PTFE thread seal tape covers the NPT connection, and Dow Corning high vacuum grease is spread over the tape to

create a vacuum seal. A stainless steel screwed-bonnet needle valve (Swagelok: SS-4JB) is connected in line to separate the vacuum pump from the three pressure sensors, and the specimen.

The first sensor^{*} is a Granville Phillips No. 270006 thermocouple gauge, which is connected to a Series 270 Granville Phillips Ionization Gauge Controller. The thermocouple gauge has 1/8 inch NPT threads, which were screwed into a stainless steel tube fitting female branch tee (Swagelok: SS-400-3TTF).

The second sensor is an MKS 626A1STAD Capacitance Manometer, which has a 1/2 inch sensing port that is coated with a thin layer of vacuum grease. The sensing port fits into a 1/2 inch to 3/8 inch NPT Adapter (Swagelok: SS-8-UT-1-6), which is then screwed into a 3/8 inch NPT to 1/8 inch NPT Reducing Adapter (Swagelok: SS-6-RA-2). The reducing adapter is then screwed into a stainless steel tube fitting female branch tee (Swagelok: SS-400-3TTF).

The third sensor is a Validyne DP15 with a 20 psi (#42) diaphragm. The Validyne DP15 is screwed onto a stainless steel tube fitting male branch tee (Swagelok: SS-400-3TTM). The DP15 is connected to a Validyne CD15 Carrier Demodulator.

The 1/4 inch stainless tubing is then connected to a steel ‘block’ tank with an internal volume of 958.7 cm³. The block increases the system volume, which decreases the effect of leaks in the vacuum system, or contaminations on measurement sensitivity. The block connects to the samples that are being tested. The stainless steel tubing, valve, and pressure sensors are fixed in position with

^{*} Note there is additional information regarding each sensor in Section 2.6.

three aluminum blocks, shown in Figure 2-23, which are anchored to a wooden board with screws. The dual-wall setup utilizing the multi-axial testing machine and the equipment cart is shown in Figure 2-24.

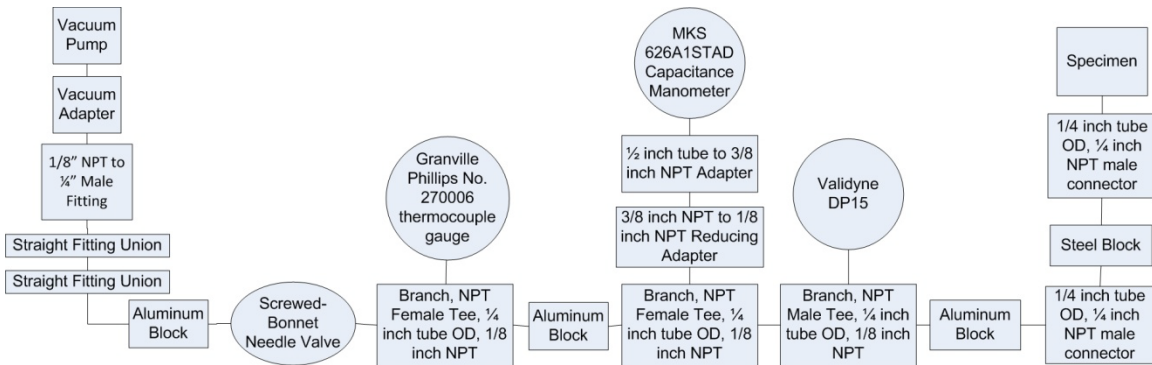


Figure 2-21: Outline of the components of the equipment cart



Figure 2-22: Top view of the components of the equipment cart, including the (a) mechanical vacuum pump, (b) valve, (c) thermocouple gauge, (d) capacitance manometer, (e) differential pressure transducer, (f) steel block, and (g) test specimen, in the benchtop testing configuration



Figure 2-23: An aluminum block holder

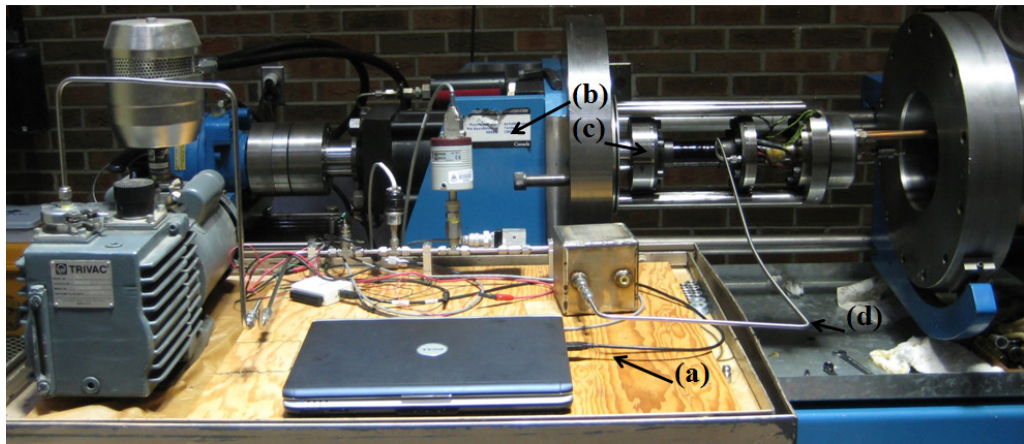


Figure 2-24: Front view of the (a) equipment cart, (b) multi-axial testing machine, (c) specimen, and (d) vacuum adapter, in the dual-wall test configuration

2.3 Specimen Preparation

The FRPC tubular specimens were manufactured using the industrial filament winding system [3] in the ACME lab. The materials consisted of basalt fiber strands (KV12, Kamenny Vek, Russia), and a bisphenol-A epoxy system with a non-MDA polyamine hardener (EPON826/EPICURE9551, Hexion Specialty Chemicals, USA) [4]. Specimens consisting of four, six and eight layers with fiber architecture of $\pm 60^\circ$ were filament wound using 38.1 mm and 50.8 mm

mandrels [4]. Fibers from the five basalt fiber creels were routed through a resin bath, maintained at 30 °C. A steel blade held against an aluminum roller



Figure 2-25: The (a) basalt fiber creels attached to the tensioning system



Figure 2-26: The (b) routing system and (c) epoxy bath

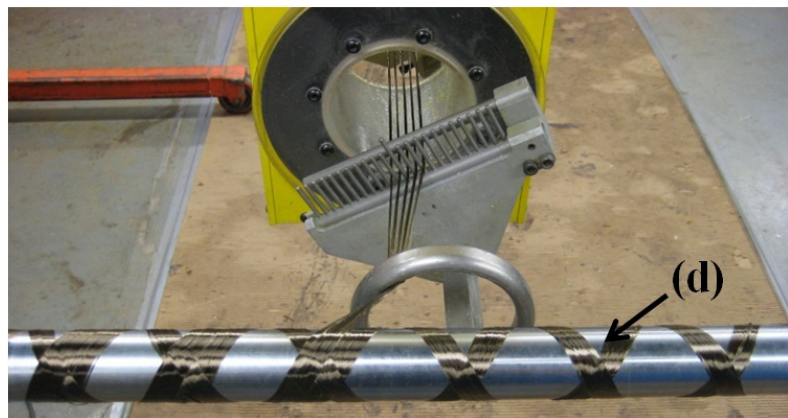


Figure 2-27: Basalt fibers being placed onto a (d) rotating 38.1 mm mandrel

controlled the amount of epoxy impregnated onto the fiber bundles. A picture of the basalt rock creels, the routing system, and the resin bath are shown in Figure 2-25 and Figure 2-26. The epoxy-coated fibers were then wrapped onto a rotating mandrel, as shown in Figure 2-27.

The steel mandrels were installed in the filament winding machine through removable adapters, and rotated using a chuck head. The mandrels were coated with a Frekote 700-NC releasing agent, and the adapter ends were covered in a high temperature tape, to ensure easy FRPC extraction. Figure 2-28 below shows a prepared mandrel installed in the filament winding machine.



Figure 2-28: An installed 1.5 inch mandrel

An OmniNT351 Omnidwind Machine Control program runs the filament winder, in symphony with the McClean Anderson tensioning system operating with 6 pounds of fiber tension per tow. The completed wet filament wound pipes were placed onto an oven baking cart, which was wheeled into a EWN-414-4E Wisconsin Oven Corp. industrial-sized oven. The mandrel was connected to a rotisserie during the curing process to prevent pooling of resin. Up to three composite pipes can be cured simultaneously, although only a single set of 38.1 mm and 50.8 mm pipes were wound during the same session to ensure epoxy consistency. The composite specimens were cured according to the optimal specifications for the epoxy [5].

2.3.1 Fiber Volume Fraction

Once cured, the pipes were removed from the oven, and extracted from the mandrels using a manual hydraulic pump, a steel jig, and an aluminum extruder plate. Three samples were marked per pipe with lengths of approximately 15.4 cm, interspersed with samples measuring 2.5 cm in length. The samples were cut using a tile cutting saw, and the dual-wall specimens were length-matched using 240 grit water lubricated polishers. The 2.5 cm long samples were used to determine the fiber volume fraction (FVF) using a burn-out procedure. The FVF, V_f , is the ratio of the fiber volume, v_f , to the composite volume, v_c , as shown in Eq. [2-1].

$$V_f = \frac{v_f}{v_c} \quad [2-1]$$

It is known that the volume of a homogenous substance is equal to the mass, m , divided by the density, ρ , as shown in Eq. [2-2].

$$v = \frac{m}{\rho} \quad [2-2]$$

Substituting Eq. [2-2] into Eq. [2-1] results in Eq. [2-3], where m_f is the fiber mass, ρ_f is the fiber density, m_m is the matrix mass, and ρ_m is the matrix density.

$$V_f = \frac{\frac{m_f}{\rho_f}}{\frac{m_f}{\rho_f} + \frac{m_m}{\rho_m}} \quad [2-3]$$

The mass of the composite, m_c , assuming zero void fractions, is equal to the mass of the matrix, m_m , and the mass of the fibers, m_f , as shown below.

$$m_c = m_m + m_f \quad [2-4]$$

Substituting Eq. [2-4] into Eq. [2-3] yields Eq. [2-5] for the fiber volume fraction.

$$V_f = \frac{\frac{m_f}{\rho_f}}{\frac{m_f}{\rho_f} + \frac{m_c - m_f}{\rho_m}} \quad [2-5]$$

The density of the matrix, ρ_m , is 1.151 g/cm^3 , and the density of the basalt fibers, ρ_f , is 2.660 g/cm^3 . The mass of the composite specimen is measured before and after commencing a burn out procedure, which removes the epoxy matrix and leaves the fibers behind, and consists of heating the specimen to 538°C (1000°F) for three hours. The mass of the composite before the burn out, the mass of the fibers remaining, and the densities of the fibers and matrix were consequently used to find the fiber volume fraction. The pipes used in this study and their fiber volume fractions are shown in Table 2-1.

Figure 2-29 shows the FVF versus the number of layers for the 38.1 mm and 50.8 mm specimens tested during the benchtop and dual-wall experiments.

Table 2-1: Dual-wall (DW) and benchtop (BT) FRPC specimen Data

Pipe	# Layers	m_c [g]	m_f [g]	m_m [g]	V_f	D_i [mm]	D_o [mm]	L_o [mm]
378DW	4	6.6	4.5	2.1	0.481	38.1	40.665	63.9
379DW	4	9.7	6	3.7	0.412	50.8	53.899	63.9
273BT	4	7.3	5.5	1.8	0.569	50.8	52.680	63
342DW	6	9.7	7.3	2.4	0.568	38.1	41.504	67
341DW	6	12.1	9	3.1	0.557	50.8	53.797	67
381BT	6	10.4	7.6	2.8	0.540	50.8	53.899	70
382DW	8	14.1	10.3	3.8	0.540	38.1	42.850	70
383DW	8	19.2	13.9	5.3	0.532	50.8	55.728	70
336BT	8	16.7	12.7	4	0.579	50.8	54.839	72

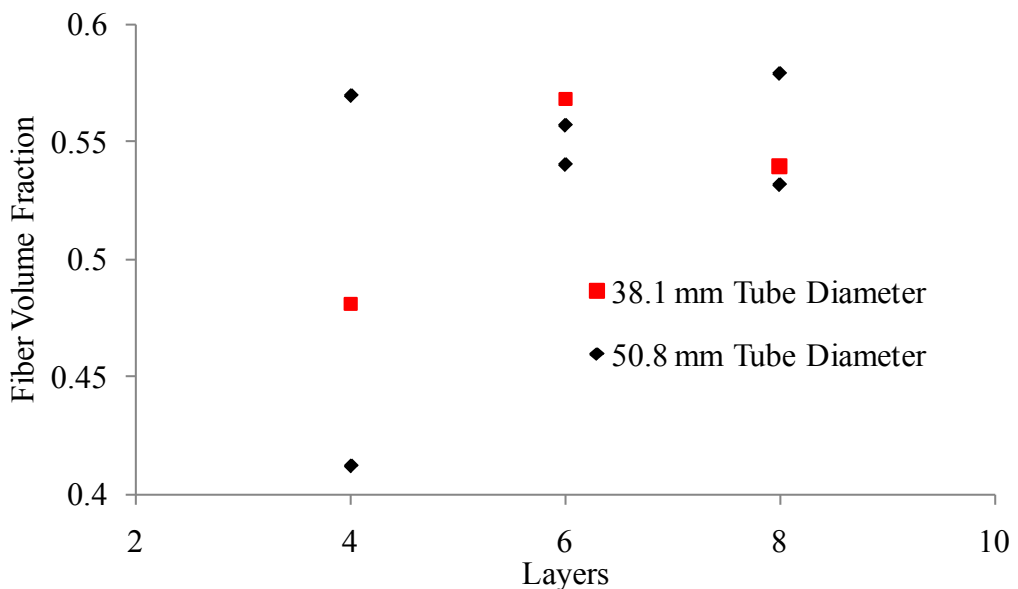


Figure 2-29: FVF versus Number of Layers

There was a relatively wide range of fiber volume fractions recorded for the four layer specimens and less for the six and eight layer specimens. A cover of excess resin collecting on the outside of the tube surface was found to be non-uniform, which is believed to have caused FVF measurements to be strongly affected for specimens with low fiber mass.

2.4 Benchtop Test Setup

The benchtop end connections, also known as ‘dummy clamps,’ were designed for testing single-wall tubes without mechanical loading. Each end connection consists of 38.1 mm (1.5 inch) long steel tubes with dimensions of 60.325 mm (2.375 inch) ID and 63.5 mm (2.5 inch) OD, and 45.136 mm (1.777 inch) ID and 47.625 mm (1.875 inch) OD, as well as a 38.1 mm (1.5 inch) long 1018 steel cylinder, which are welded to a 101.6 mm (4 inch) by 101.6 mm (4 inch) 12.7 mm ($\frac{1}{2}$ inch) thick steel plate. There are two versions of the end connections, a supply end connection and a passive end connection, which are identical except for an additional $\frac{1}{4}$ inch NPT hole in the center of the supply end connection, that is used to accommodate the $\frac{1}{4}$ " NPT to $\frac{1}{4}$ " Swagelok Male Fitting (Swagelok: SS-400-1-4), and connects the supply end connection to the equipment cart. Note that Jet-Lube PTFE Petro Tape and Dow Corning vacuum grease coat the NPT fitting, and ensure a vacuum tight seal.

2.4.1 Specimen Preparation and Bonding

The tubular specimens are lightly sanded with 1000 grit Premier Red Aluminum oxide Dri-Lube sheets from Carborundum Abrasives (B 0712 DO), and washed with acetone to ensures a strong bond between the steel and the composite specimen. The prepared specimen is then placed in the supply end connection, and Cold Cure epoxy is used to bond the sample. The epoxy cures overnight, and the next day additional epoxy is added until the specimen-clamp profile matches that shown in Figure 2-30, which indicates uniformity.



Figure 2-30: Cold-cure epoxy profile used for potting specimens

The free end of the composite specimen is bonded to the passive end connection using the same procedure. Concentricity is approximated by adjusting the specimens' position in the end connection until the epoxy annulus is consistent around the pipe.

2.5 Data Collection

Pressure is measured by a Granville Phillips No. 270006 thermocouple gauge, MKS 626A1STAD Capacitance Manometer, and a Validyne DP15, while temperature is measured by a National Instruments LM19 temperature sensor. The voltage outputs of the four gauges are measured by a National Instruments NI USB-6009 data acquisition device, and recorded by a LabVIEW virtual instrument. The Front Panel of the .vi, shown in Figure 2-31, includes a

table showing instantaneous voltage, and a plot showing the recorded voltage changing with time.

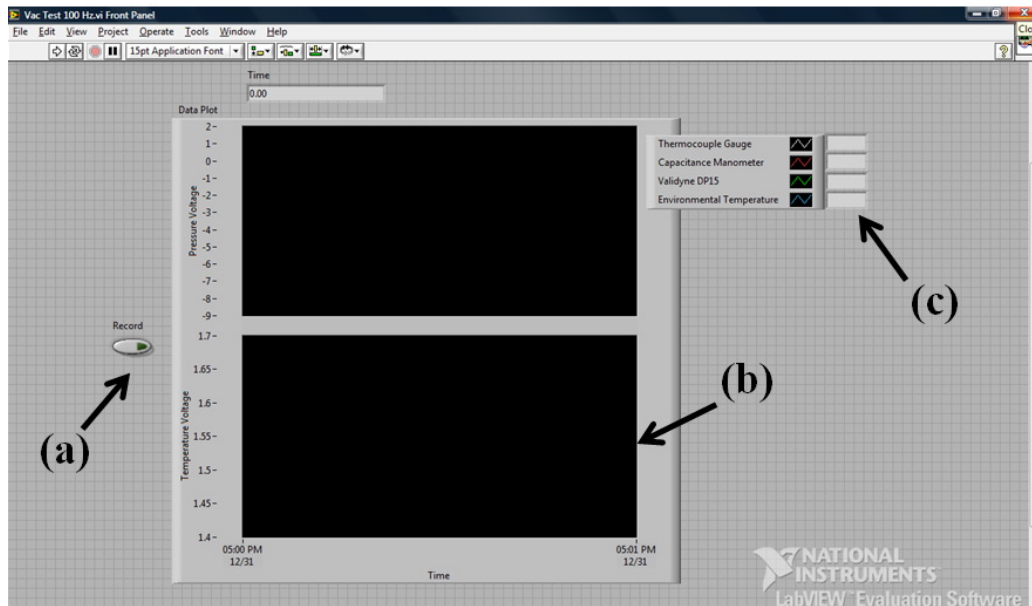


Figure 2-31: Front Panel of the virtual instrument showing the (a) record button, (b) plot of recorded voltage changing with time, and (c) table of instantaneous voltages.

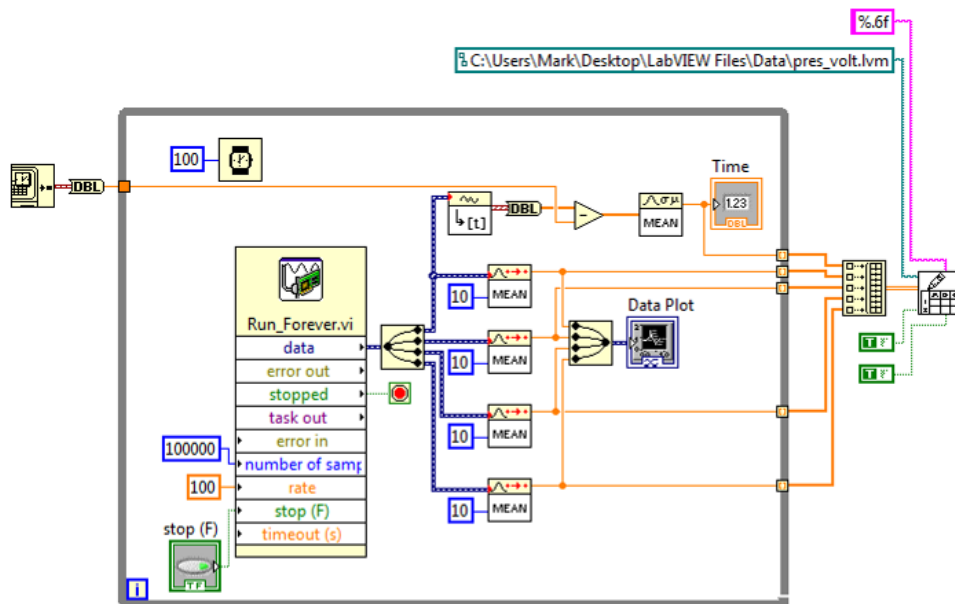


Figure 2-32: Block Diagram of the virtual instrument

The Block Diagram of the virtual instrument, shown in Figure 2-32, samples the data at 100 Hz and stores the average of every ten values to the computer's random access memory (RAM). The data is recorded to a file on the hard drive when the 'Record' button on the Front Panel is clicked.

2.6 Sensor Details

2.6.1 Thermocouple Gauge

The Granville Phillips No. 270006 thermocouple gauge measures pressure over a range from 1.33×10^{-1} Pa (10^{-3} Torr) to 133 Pa (1 Torr), and is powered by a Granville Phillips Series 270 Gauge Controller [6]. The manual for the Gauge

$$P = 0.0027 * \exp(3.0489 * V_T) \quad [2-6]$$

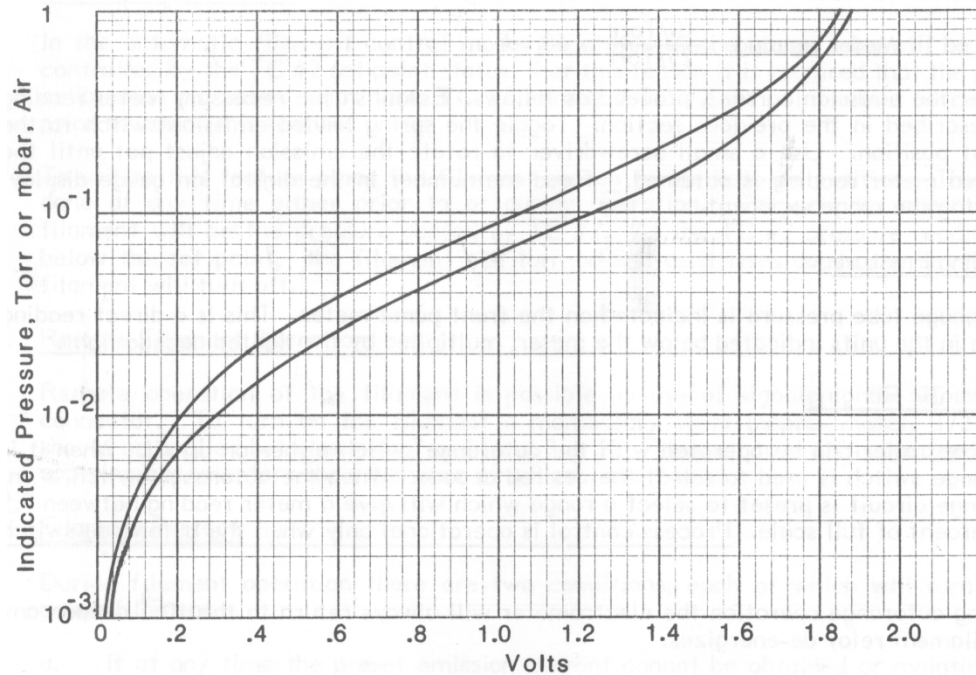


Figure 2-33: Thermocouple gauge volts to pressure conversion chart [6]

Controller includes a calibration curve specific to the thermocouple gauge, which converts voltage to Torr, as shown in Figure 2-33. A pencil and ruler were used to draw a line between the upper and lower boundaries (i.e., 1.88 V and 0.2 V respectively) and develop Eq. [2-6], which converts volts, V_T , to pressure, P .

2.6.2 Capacitance Manometer

The MKS 626A1STAD Capacitance Manometer is sensitive for pressures in the range from 66.7 Pa (0.5 Torr) to 133 kPa (1000 Torr), and has an accuracy of 0.25% of full scale. It is powered by a Canadian Analytical & Process Technologies (CAPT) 115V 10A power supply (SR5-SP411-11-0), and has a conversion factor of 100 Torr = 1 V.

2.6.3 Validyne DP15

The Validyne DP15 differential pressure transducer and Validyne CD15 Carrier Demodulator were calibrated utilizing an Omega DPI 610 portable pressure calibrator and a conversion factor of 110 kPa = 10 V for five pressurizations from 0 kPa to 110 kPa, and five depressurizations from 110 kPa to 0 kPa. The individual data points for all ten data sets are shown in Figure 2-34.

The equation representing the slope of voltage, V_T , versus pressure, P , shown in Figure 2-34 is re-arranged, and presented as Eq. [2-7].

$$\Delta P = \frac{V_T - 0.0679}{0.0913} \quad [2-7]$$

The pressure terms are converted from units of kPa, to Torr, resulting in Eq. [2-8] for environmental pressure, P_{env} , based on the DP15 voltage and the vacuum pressure, P_{vac} .

$$P_{\text{env}} = \left(\frac{V_T - 0.0679}{0.0913} \right) * \left(\frac{760 \text{ Torr}}{101.325 \text{ kPa}} \right) + P_{\text{vac}} \quad [2-8]$$

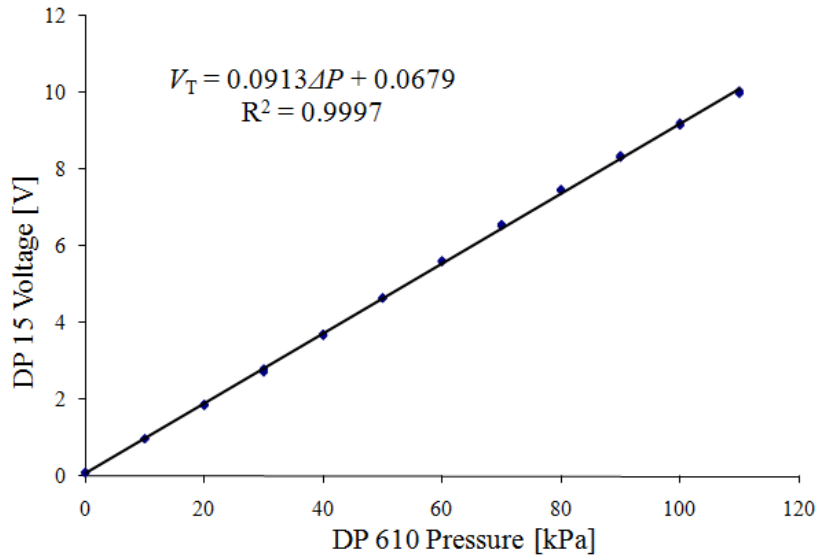


Figure 2-34: DP15 Voltage versus Pressure Calibration Curve

2.6.4 Temperature Sensor

A National Instruments LM19 temperature sensor was built to measure the environmental temperature of the test lab. The LM19 sensor is a precision analog output CMOS integrated-circuit (IC) temperature sensor with an operating range from -55°C to 130°C [7], and is powered by a 5V power supply. The reported accuracy of the LM19 utilizing the manufacturer's transfer function for converting voltage to temperature is $\pm 2.5^{\circ}\text{C}$, at an ambient temperature of $+30^{\circ}\text{C}$ [7]. The temperature sensor draws a quiescent current of less than $10 \mu\text{A}$, resulting in a self-heating in still air of less than 0.02°C [7].

2.6.4.1 Calibration

The IC was calibrated at temperatures of -12, 2, 18, and 27 °C, against an OMEGA HH506 Digital Thermometer that has a resolution of 0.1 °C [8]. The corresponding sensor output voltage was recorded with the LabVIEW USB data acquisition system. The IC responds slowly to changes in temperature, so multiple tests were run to ensure the IC was at a steady state temperature. From the National Semiconductor LM19 data sheet [7], the recorded voltage, V_T , can be converted to a temperature, T , in degrees Celsius using Eq. [2-9].

$$T = -1481.96 + \sqrt{2.1962 \times 10^6 + \frac{1.8639 - V_T}{3.88 \times 10^{-6}}} \quad [2-9]$$

A linear polynomial was curve fit to the temperature data, shown in Figure 2-35. The resulting calibration equation, Eq. [2-10], is shown below where T_a is the reference temperature (°C) from the HH506 Digital Thermometer and T_m (°C) is from Eq. [2-9].

$$T_a = 1.02 * T_m - 0.2952 \quad [2-10]$$

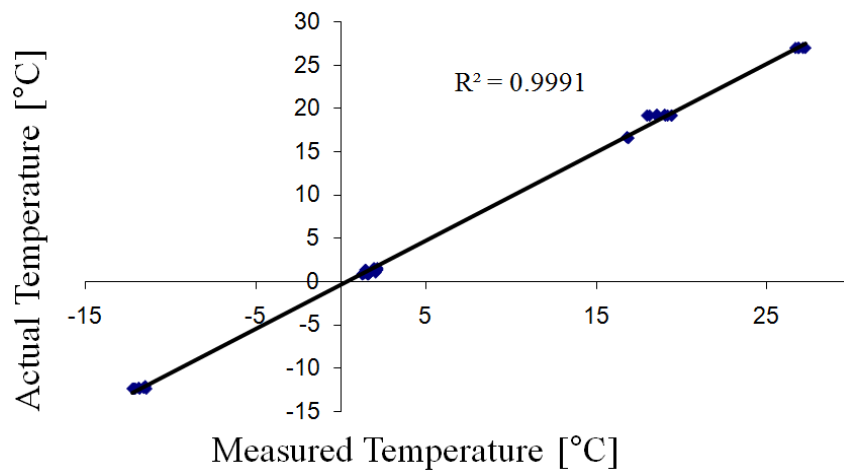


Figure 2-35: LM19 calibration curve

2.7 Vacuum System Volume

The volume of the components in the vacuum system was calculated by comparing their mass before and after being filled with tap water. In addition, the mass of the $\frac{1}{4}$ inch stainless steel tubing was compared to the mass of a standard length that had a known internal volume.

2.8 Sampling Frequency and Noise

Early in the setup process it was found the pressure sensors were generating noisy signals. In order to facilitate the determination of the source of noise, data were collected with a sampling rate of 1000 Hz for 829 seconds, and a spectral analysis plot was generated using an FFT Discrete Fourier Transform from an example given by a MathWorks tutorial [9], as shown in Figure 2-36. The spike at 60 Hz is the electrical noise in the building, and the spike at 0 Hz is the sensor response. Lack of additional spikes suggests the 60 Hz signal is the only prevalent noise, and it can be eliminated using a low pass filter.

2.8.1 Filters

Two types of filters were applied to the acquired data in order to determine which one produced the smoothest and most consistent results.

2.8.1.1 Fourth Order Butterworth

A fourth order low pass Butterworth filter was chosen as it is easily accessible in MATLAB using the built in functions, and can be combined

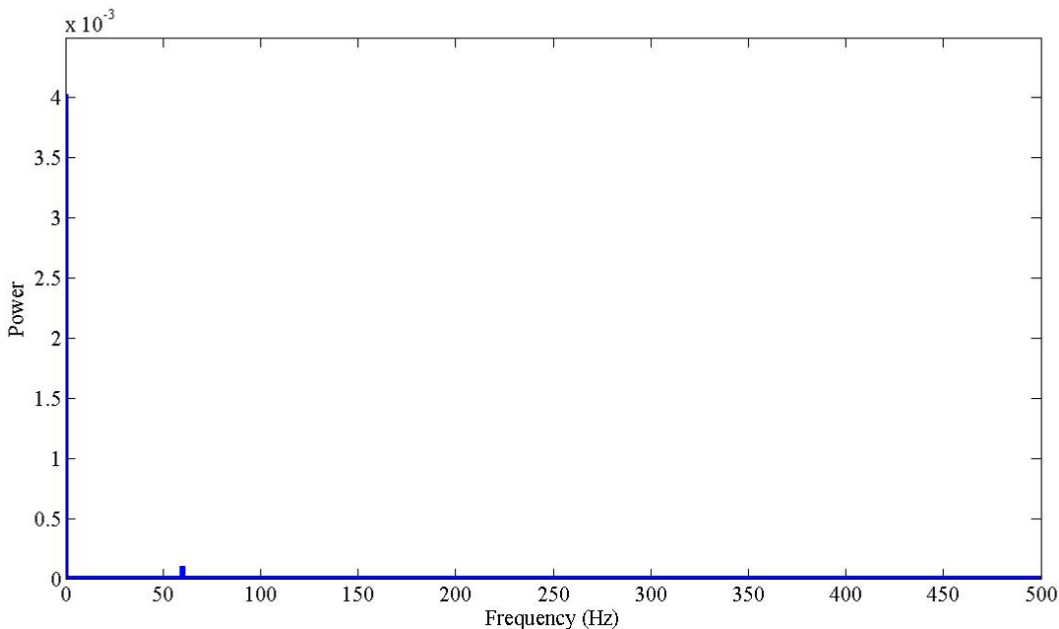


Figure 2-36: Spectral Power plot for a 1000 Hz signal

with the ‘`filtfilt`’ command to ensure no phase shift in the resultant filtered data. A cutoff of 0.0002 radians per second was used, as the measured data has a frequency approaching 0 Hz, the noise was at a frequency of 60 Hz, and it provided a smooth curve that maintains the shape of the original data.

2.8.1.2 Fastsimooth Filter

The fastsmooth filter is a pseudo-Gaussian sliding average filter with edge smoothing, and was posted on the MATLAB Central Exchange System on May 21, 2008 [10]. This filter proved to provide more consistent smoothing results for each data set, and was used in favor of the fourth order Butterworth. A comparison of the fourth order Butterworth and Fastsmooth filtered data is shown in Figure 2-37. Note how the Butterworth filter does not eliminate all of the noise, and the Fastsmooth filter consistently travels through the center of the unfiltered data.

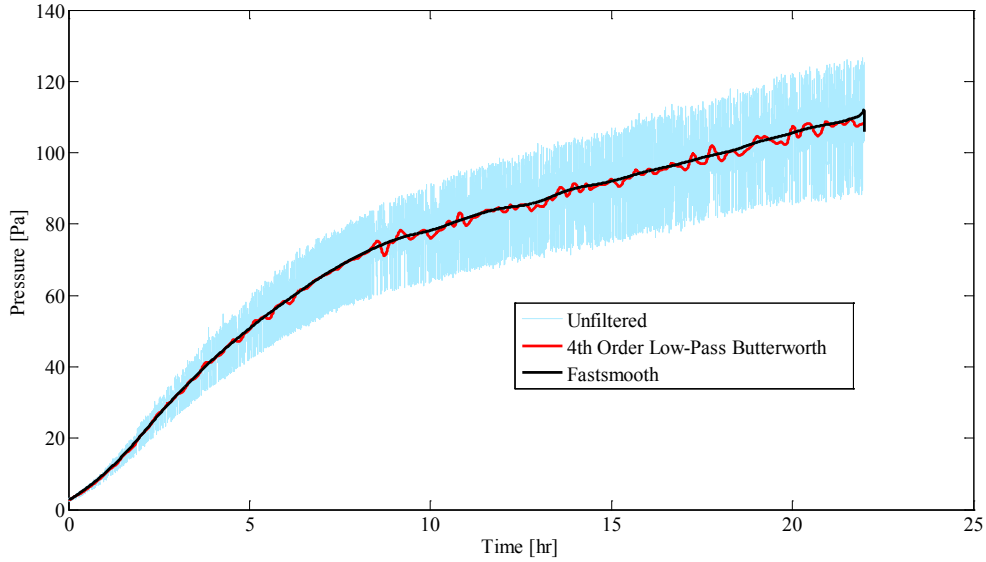


Figure 2-37: Filtering the four layer specimen data (BT configuration, test one)

2.9 Dual-Wall Test Procedure

2.9.1 Controller

For testing under mechanical loading an MTS 458.10 MicroConsole and MTS Flextest GT Digital Controller were used to load the dual-wall flanged end connections, under tension, at a rate of 4.63 N/s (1.04 lb/s). The digital controller also recorded test time, load, axial strains, and transverse strain for each specimen installed in the multi-axial testing machine.

2.9.2 Loading Considerations

The load sharing between the two concentric pipes of the dual-wall specimens is based on thin wall pressure vessel theory. The free body diagram of the axial loading scheme is shown in Figure 2-38, where F_A is the applied load, E_l

is the longitudinal modulus of elasticity, A_o and A_i are the areas of the outer and inner tubes, respectively, L_o is the initial length, and δ is the stretched length.

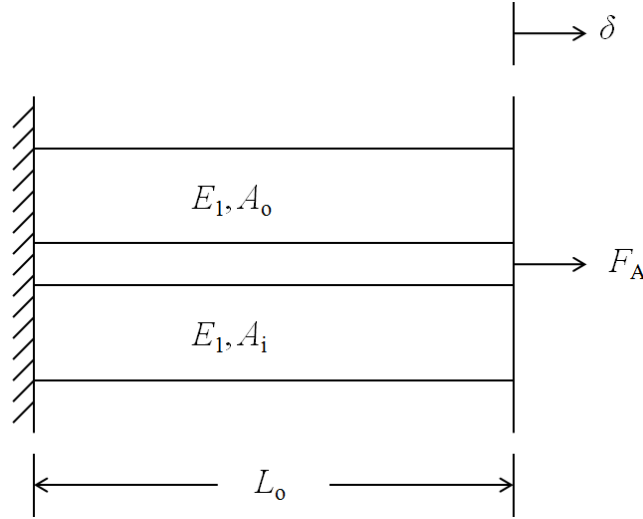


Figure 2-38: Free body diagram of a dual-wall pipe subjected to uni-axial tension

2.9.2.1 Load Sharing

The equation relating the applied axial load, F_A , to the longitudinal axial stress, σ_1 , is shown in Eq. [2-11], where A_A is the system's cross-sectional area, i.e., the summation of the individual pipe cross-sectional areas, A_o and A_i respectively.

$$F_A = \sigma_1 A_A \quad [2-11]$$

It is known that for each individual specimen, longitudinal axial stress is related to longitudinal modulus of elasticity and longitudinal axial strain, ε_1 , through Eq. [2-12].

$$\sigma_l = E_l \varepsilon_l \quad [2-12]$$

Furthermore, axial strain is calculated utilizing Eq. [2-13], where δ is the stretched length and L_o the original length.

$$\varepsilon_l = \frac{\delta}{L_o} \quad [2-13]$$

The axial load applied to the dual-wall system, shown in Eq. [2-11], can be expanded by substituting Eq. [2-12] for the longitudinal stress component and Eq. [2-13] for the axial strain component as shown in Eq. [2-14].

$$F_A = E_l \frac{\delta}{L_o} (A_o + A_i) \quad [2-14]$$

The axial load applied to the outer pipe, F_o , is shown in Eq. [2-15], where σ_o is the longitudinal axial stress applied to the outer pipe.

$$F_o = \sigma_o A_o \quad [2-15]$$

The axial load applied to the outer pipe can be expanded by substituting Eq. [2-12] for the longitudinal stress component and Eq. [2-13] for the axial strain component, as shown in Eq. [2-16], where E_l is the outer pipe's modulus of elasticity.

$$F_o = E_l \frac{\delta}{L_o} A_o \quad [2-16]$$

Taking the ratio of F_o/F_A , i.e., Eq. [2-16]/Eq. [2-14], indicates the proportion of the applied load that is shared by the outer tubular specimen, as

shown in Eq. [2-17]. Note the proportion of the applied load shared by the inner tubular specimen can be calculated by utilizing the same method.

$$\frac{F_o}{F_A} = \frac{E_l \frac{\delta}{L_o} A_o}{E_l \frac{\delta}{L_o} (A_o + A_i)} \quad [2-17]$$

The strain components will cancel by employing the assumption that both tubes maintain the same original length and stretch, which results in Eq. [2-18].

$$\frac{F_o}{F_A} = \frac{E_l A_o}{E_l (A_o + A_i)} \quad [2-18]$$

The longitudinal modulus of elasticity depends on the composite's lamina and laminate thickness, fiber and matrix material properties (i.e., longitudinal elastic modulus, transverse elastic modulus, major Poisson's ratio, minor Poisson's ratio, and shear modulus). If one assumes the outer and inner pipes have the same number of layers and laminate thickness, then they also have identical longitudinal elastic modulus constants. Furthermore the outer pipe's modulus of elasticity and the systems modulus of elasticity cancel from Eq. [2-18], as the systems effective elastic modulus is equivalent to each individual pipes' elastic modulus, which results in Eq. [2-19] the load transfer ratio, which is the ratio of the applied load that is transferred to the outer tubular specimen relative to the entire system.

$$\frac{F_o}{F_A} = \frac{A_o}{(A_o + A_i)} \quad [2-19]$$

Furthermore, the area of a thin cylinder is given by Eq. [2-20], where D_o and D_i are the outer and inner diameters, respectively.

$$A = \frac{\pi}{4} (D_o^2 - D_i^2) \quad [2-20]$$

Note the load transfer ratios for the four, six and eight layer tubular specimens are included in Table 2-2.

Table 2-2: Load transfer ratios

Pipe	$\frac{F_o}{F_A}$	$\frac{F_i}{F_A}$
Four Layer	0.57	0.43
Six Layer	0.56	0.44
Eight Layer	0.55	0.45

2.9.2.2 Loading Rates

Differentiating Eq. [2-11] with respect to time results in Eq. [2-21], which is the stress loading rate, $\dot{\sigma}_A$, of a dual-wall tubular specimen subjected to the axial traction loading rate, \dot{F}_A .

$$\dot{\sigma}_A = \frac{\dot{F}_A}{A_o + A_i} \quad [2-21]$$

Resulting stress loading rates were determined to be 12.23 kPa/s (1.77 psi/s) for the four layer dual-wall specimen, 10.53 kPa/s (1.53 psi/s) for the six layer specimen, and 7.02 kPa/s (1.02 psi/s) for the eight layer specimen. Loading rates

of between 4.63 kPa/s and 46.3 kPa/s were used in [11] to determine the effect of winding tension and loading rate on the test results for single wall FRPC tubes. Note that the utilized loading rates were all within the range specified by [11], to allow for direct comparison between historical leakage, winding tension, and loading rate data. Furthermore, note that the relative stress applied to the external tubular specimen is found by multiplying the systems' longitudinal stress (calculated from Eq. [2-11]) by the load transfer ratio from Eq. [2-19]. Furthermore, the relative stress applied to the internal tubular specimen is found utilizing the same method, except A_o is replaced with A_i in the numerator of Eq. [2-19].

2.9.3 Test Procedure

To measure the zero load baseline leakage rate the digital controller was set to apply zero load while the vacuum pump evacuated the annulus for a period of 48 hours. After initial depressurization, the screwed-bonnet needle valve separating the vacuum pump from the annulus of the pipe specimens was closed, and the pressure increase was recorded for 10 hours. The valve was then opened and the specimen was evacuated for an additional 13 hours. Note the vacuum source, testing machine pumps and load controller ran continuously to ensure consistently applied loading, and that no leakage occurred through the screwed-bonnet needle valve.

Following the initial assessment of vacuum decay, the dual-wall specimen was loaded with a tensile rate of 4.63 N/s (1.04 lb/s). Upon reaching a load of

4.45 kN (1000 lb) the loading was held constant. The MTS Flextest GT Digital Controller and laptop data acquisition systems recorded the data during the test, and the mechanical pump ran continuously with the screwed-bonnet needle valve open. Any changes to the vacuum pressure, during the test, were a direct result of the load applied to the sample. When reaching the axial load of 4.45 kN (1000 lbs), the valve was closed and the annular pressure rise was recorded for 10 hours. After 10 hours had passed, the valve was opened and the annulus was evacuated for 13 hours. This procedure was repeated for limit loads of 8.90 kN (2000 lb), and 13.3 kN (3000 lb) loads. After completion of the pressure rise measurements at 13.3 kN (3000 lb), a puncture test was performed using a rotary saw to ensure the sensors were measuring annulus pressure (i.e. ensuring that all vacuum ports were properly open and not blocked by e.g. adhesive). The rotary saw punctures the outer tube of the dual-wall specimen, as shown in Figure 2-39, exposing the annulus to atmospheric pressure.

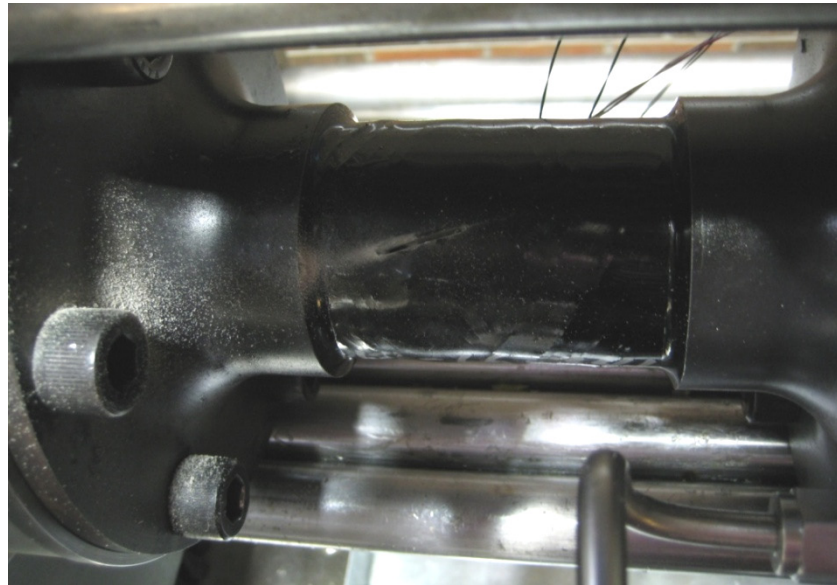


Figure 2-39: A dual-wall FRPC specimen after performing a puncture test

2.10 Benchtop Test Procedure

Once the benchtop specimens were prepared, bonded to the ‘dummy clamps,’ and installed in the equipment cart, they were subjected to an initial depressurization from the vacuum pump for a period exceeding 40 hours while the data acquisition system recorded the pressure and temperature readings. The screwed-bonnet needle valve was then closed, while the vacuum pump continued to run, and the pressure rise was measured for a period exceeding 10 hours. After the pressure rise test was completed, the screwed-bonnet needle valve was re-opened, and the specimens were depressurized for a period exceeding 10 hours. The 10 hour cyclic test was repeated until the slope of the pressure versus time plots appeared to change slightly, as shown in Figure 2-40. Note that the pressure rise data plots for the benchtop and dual-wall tests are included in Appendix A.

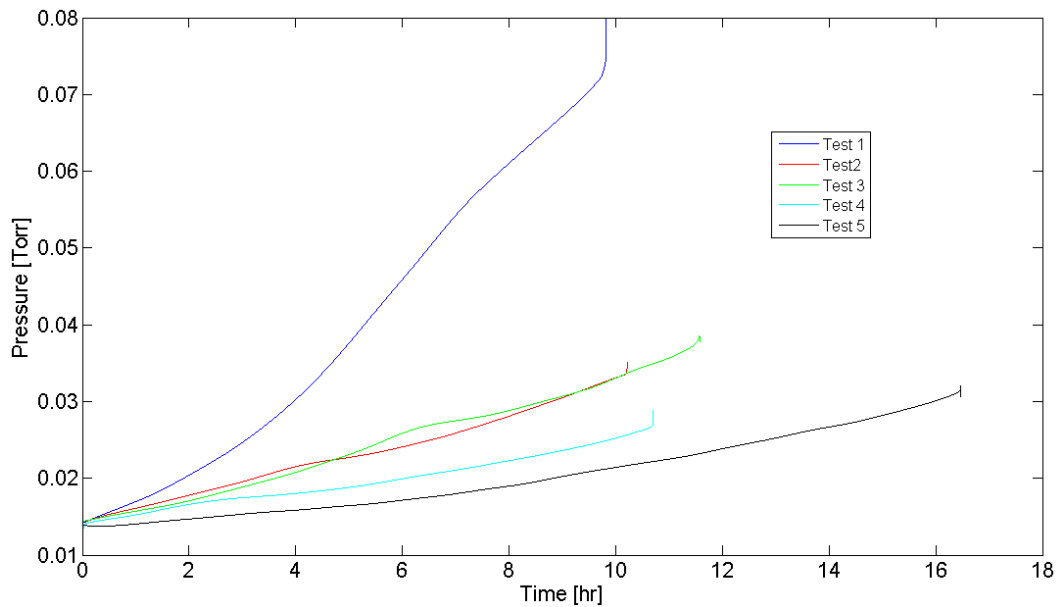


Figure 2-40: Benchtop pressure rise data for the six layer FRPC specimen

2.11 Error Analysis

A full error analysis of the experimental data that takes into consideration the repeatability of the pressures and temperature measurement devices was not performed, and thus a system error is not available. However, it is expected that if an error analysis was performed it would result in a repeatability error that is of the same magnitude, or lower than the calculated mass flow rates.

2.12 Conclusions

Two testing configurations, i.e., loaded dual-wall, and unloaded single-wall composite pipes were developed to measure the minimum achievable annulus pressure, and leakage rate for various loading scenarios. The end connection designs for both loading scenarios were presented, and their main points highlighted. The FRPC manufacturing and end connection installation procedures were also outlined. In addition, the test procedures for the dual-wall and single-wall cases were shown, along with a derivation for the load sharing. The equipment cart system was also highlighted, along with the LabVIEW data collection software, the system volume measurements, the pressure and temperature gauges, and the filters used to remove noise from the signals. In addition, the FVF equation was derived, and data was presented for the four, six, and eight layer tested specimens. Furthermore, the following conclusions can be summarized from the information presented in this chapter.

- A dual-wall flanged end-connection test setup was designed and built to measure the minimum achievable annulus pressure, and the

air leakage rate under various loading scenarios, for FRPC tubular specimens.

- A single-wall benchtop test setup was designed and built to measure the minimum achievable holding pressure for FRPC tubular specimens.
- Taking into account the time required for specimen manufacture, end connection assembly, depressurization and testing, each complete specimen test for the single and dual-wall setups requires approximately two weeks.
- The equipment cart can be used for either the single or dual-wall test setups by changing the vacuum adapter.
- The thermocouple gauge and capacitance manometer are able to cooperatively measure the annulus pressure over a net range from 1.33×10^{-1} Pa (10^{-3} Torr) to 133 kPa (1000 Torr).
- A large variation in fiber volume fraction was found for the four layer specimens. A cover of excess resin remaining on the specimen surface after manufacturing was non-uniform, which caused the FVF measurements to be affected for specimens more strongly with low fiber mass, i.e. the four layer specimens.
- The applied axial stress loading rates were 12.23 kPa/s (1.77 psi/s) for the four layer dual-wall specimen, 10.53 kPa/s (1.53 psi/s) for the six layer specimen, and 7.02 kPa/s (1.02 psi/s) for the eight layer

specimen, which were all within the range specified by reference [11], meaning historical single-wall FRPC pipe data can be compared with these experimental results.

2.13 References

- [1] Ruhl M, Juss K, Mertiny P. Novel Vacuum-Insulated Dual-Wall Composite Pipe for Cold Environment Applications. Proc. 28th International Conference on Ocean, Offshore and Arctic Engineering; 2009 31 May – 5 June; Honolulu, HI.
- [2] Leybold D8 D8A Trivac Rotary Vane Dual Stage Mechanical Vacuum Pump Rebuilt Refurbished [homepage on the Internet]. [cited 2010 Jan 7]. Available from: <http://www.pchemlabs.com/product.asp?pid=649>
- [3] Wolodko J, Mertiny P, Meijer G, Martens M, Ellyin F. Development of a facility for filament winding GFRP tubulars. Proc. 46th International SAMPE Symposium; 2001; Long Beach, CA, pp. 1271-1282.
- [4] Ruhl M, Mertiny P. Diffusion and leakage in vacuum-insulated dual-wall composite piping. Proc. International SAMPE Symposium; 2010; Seattle, WA.
- [5] Meijer G. [$\pm 60^\circ_3$]_T Glass Fibre Reinforced Epoxy Tubes and the Influence of an Interleaf on Transverse Cracking and Fluid Containment. PhD Dissertation; University of Alberta; 2006.
- [6] Granville-Phillips. Series 270 Ionization Gauge Controller Instruction Manual, P/N 270046 100; Nov 1984.
- [7] National Semiconductor LM19 2.4V, 10 μ A, TO-92 Temperature Sensor. [Monograph on the Internet]. [Cited 2009 Oct 13]. Available from: <http://www.national.com/ds/LM/LM19.pdf>

[8] OMEGA HH506 Digital Thermometer [monograph on the Internet]. [Cited 2009 Nov 25]. Available from:

<http://www.omega.com/manuals/manualpdf/M2811.pdf>

[9] The MathWorks [homepage on the Internet]. Support – Using FFT to Obtain Simple Spectral Analysis Plots. [Cited 2010 Jan 14]. Available from:

<http://www.mathworks.com/support/tech-notes/1700/1702.html>

[10] O'Haver T. Fast smoothing function [monograph on the Internet]. [Updated 2008 May 22; cited 2009 Dec 9]. Available from:

<http://www.mathworks.com/matlabcentral/fileexchange/19998-fast-smoothing-function>

[11] Mertiny P, Gold A. Quantification of leakage damage in high-pressure fibre-reinforced polymer composite tubular vessels. *Polymer Testing*. 2007;26:172-179.

3. PERMEABILITY*

Leakage through an FRPC material, i.e., permeation, was assessed by converting the measured pressure and temperature data to a mass flow rate, and then utilizing Darcy's law with the measured data to characterize the leakage. Knowledge of the leakage rate allows a prospective designer to perform an economic analysis on the viability of vacuum insulation at various annulus pressures. The volumetric flow rate of the dual-vane mechanical vacuum pump, combined with the leakage mass flow rate, and the target pressure can be employed to calculate the maximum serviceable pipe length for a specific vacuum source. In addition, if the energy required for thermally managing the working fluid exceeds the heat flux then a dual-wall FRPC pipe system with annulus vacuum insulation is a worthwhile endeavor.

Both experimental setups that were previously discussed in Chapter 2, i.e., benchtop and multi-axial, are considered in this chapter. Vacuum pressure was applied to the annulus formed by the concentric tubes, and the pressure rise was measured for each applied tensile traction load. The data was subsequently analyzed using the equations developed in the present chapter.

*A version of this chapter was published in the conference proceedings of the International SAMPE Symposium, 2010, Seattle, WA [1].

3.1 Equation Derivations

3.1.1 Mass Balance

A mass balance was completed on the system control volume, i.e. the annulus for a dual-wall specimen, and an equation was developed for the sources of pressure rise, as highlighted in Eq. [3-1]. It is assumed the mass flow rate leaving the system, \dot{m}_{out} , is exiguous relative to the mass flow rate entering the system, \dot{m}_{in} , *ergo* \dot{m}_{out} is ignored. In addition, prior to commencing vacuum pressure decay tests, the control vacuum was evacuated for a period of 40 hours for benchtop, and 13 hours for the axial traction tests. This ensures that the contamination and outgassing mass flow rate, \dot{m}_{CO} , has a negligible effect on the systems effective mass flow rate, and hence \dot{m}_{CO} is ignored. Furthermore, the vacuum system without a specimen installed was capped and calibrated prior to performing vacuum decay tests, and a vacuum system leakage mass flow rate, \dot{m}_{SL} , was determined, and subsequently subtracted from the leakage mass flow rate assessed during specimen testing. From Eq. [3-1], the remaining component is the mass flow rate due to intrinsic permeability, \dot{m}_k . The intrinsic permeability-based mass flow rate represents a damaged specimen, assuming flow along pathways, i.e., cracks in the polymer matrix material, and will vary depending on the extent of the damage.

$$\dot{m} = \dot{m}_{\text{in}} - \dot{m}_{\text{out}} = \dot{m}_k + \dot{m}_{\text{SL}} + \dot{m}_{\text{CO}} - \dot{m}_{\text{out}} = \dot{m}_k \quad [3-1]$$

3.1.2 Mass Flow Rate

Assuming that air is an ideal gas, the mass of air within an enclosed control volume, i.e., the annulus of a dual-wall specimen, or the space enclosed by a single tubular specimen, is calculated by utilizing the ideal gas law shown in Eq. [3-2].

$$m = \frac{PVM}{RT} \quad [3-2]$$

The systems enclosed control volume, V , the molar mass of air, M (29.97 kg/kmol), the Universal Gas Constant, R (8.3145 kJ/kmol/K), and the temperature, T , of the molecules in the enclosed space are assumed to be constant with time. Thus, if the systems mass were to increase with time, the pressure must show a corresponding increase as well. Differentiating Eq. [3-2] with respect to time yields the following equation for mass flow rate, \dot{m} :

$$\dot{m} = \frac{dm}{dt} = \frac{V M}{R T} \frac{dP}{dt} \quad [3-3]$$

where P is the measured pressure of the control volume. Note that any molecules entering the system must be causing the mass and pressure increases, and the systems change in mass with respect to time, dm/dt , is thus equivalent to the leakage mass flow rate. Furthermore, note that a constant leakage rate was assumed for each test condition and loading regime, which allows for the pressure derivative term to be obtained from the first derivative of a linear curve fit of the system pressure versus time data.

3.1.3 Intrinsic Permeability

The intrinsic permeability was calculated for each FRPC specimen using Darcy's Law. An expression for the intrinsic permeability was derived based on the velocity vector for a fluid penetrating a porous medium, shown in Eq. [3-4].

$$\vec{u} = -k \nabla P \quad [3-4]$$

where \vec{u} is the velocity vector, k is the permeability of the specimen, and ∇P is the pressure gradient. Air is assumed to flow only in the radial direction relative to the specimen axis, which allows for the simplification of Eq. [3-4], *ergo* Eq. [3-5], where dP/dr is the pressure gradient across the FRPC wall.

$$u = -k \frac{dP}{dr} \quad [3-5]$$

The velocity component, u , from Eq. [3-5], can be replaced with the ratio of the volumetric flow rate, \dot{V} , to the surface area normal to the fluid flow, i.e., $A_s=2 \pi r L$, where r is the tube radius, and L is the specimens length, evolving into Eq. [3-6].

$$\frac{\dot{V}}{2 \pi r L} = -k \frac{dP}{dr} \quad [3-6]$$

The volumetric flow rate is not constant along the flow line, as the volume changes with air pressure, and thus, the ideal gas law is differentiated with respect to time to compensate, as shown in Eq. [3-7].

$$P\dot{V} = \frac{\dot{m}}{M} RT \quad [3-7]$$

Substituting \dot{V} , from Eq. [3-7], into Eq. [3-6] and utilizing the separation of variables technique induces the following integral, which is evaluated along the direction of air flow into the annulus:

$$\int_{r_o}^{r_i} \frac{dr}{r} = \frac{-kM}{\dot{m}RT} 2\pi L \int_{P_{env}}^{P_{vac}} P dP \quad [3-8]$$

Integrating Eq. [3-8] with the indicated boundary conditions, i.e., r_i and r_o the inner and outer radii, respectively, and P_{vac} and P_{env} the vacuum and environmental pressures, respectively, results in Eq. [3-9] for permeability:

$$k = \frac{-\ln\left(\frac{r_i}{r_o}\right)\dot{m}RT}{\pi LM(P_{vac}^2 - P_{env}^2)} \quad [3-9]$$

However, the permeability of various materials and fluids can only be directly compared if it is converted to an intrinsic permeability, k' , which takes into account the fluid properties, and is defined by Eq. [3-10] (with dimension of length squared).

$$k' = \mu k \quad [3-10]$$

where the dynamic viscosity for air at 20°C, μ , is given as 1.80×10^{-5} (Pa s) [2].

Note that the dynamic viscosity of air is assumed to be constant across the FRPC wall. Substituting Eq. [3-10] into Eq. [3-9], results in Eq. [3-11] for air flow resembling isothermal Newtonian steady-state flow permeating a porous circular

wall in the radial direction, which is the sought expression for intrinsic permeability.

$$k' = \frac{-\ln\left(\frac{r_i}{r_o}\right)\dot{m}RT\mu}{\pi LM(P_{vac}^2 - P_{env}^2)} \quad [3-11]$$

where the leakage mass flow rate, \dot{m} , is calculated using Eq. [3-3], P_{vac} is the vacuum pressure, and P_{env} is the environmental pressure. A similar equation was obtained while establishing a relation between conductance and permeability [3], for isothermal flow of gases through porous media.

In a previous study [4], an intrinsic permeability of 10^{-18} m^2 was referred to as low, 10^{-17} m^2 as moderate, and 10^{-16} m^2 as high for the permeation of pressurized NUTO H 46 hydraulic fluid through $[\pm 60]_{3T}$ E-glass/epoxy composite tubular specimens that were damaged during mechanical loading. The intrinsic permeability values calculated in this study for undamaged basalt/epoxy FRPC tubes are in the range of 10^{-21} to 10^{-23} m^2 for both testing scenarios, which suggests the specimens were practically impermeable.

3.2 Testing Configurations

Two different test configurations were utilized in measuring the mass flow rate and calculating permeability, namely the benchtop and dual-wall scenarios. The benchtop tests were designed to subject single-wall tubular specimens to long-term vacuum conditions in the absence of mechanical loads. It was assumed that pristine specimens would contain only those physical flow pathways created

during manufacture, and the specimens would exhibit significantly less leakage compared with specimens subjected to axial traction loads. Accordingly, the benchtop tests explore leakage conditions resulting purely from manufacturing processes. Conversely, the dual-wall tests involve subjecting concentric tubular specimens to axial traction loads, and measuring the leakage rate. It was expected that the mechanically loaded specimens would possess additional physical flow pathways required for higher leakage rates.

3.3 Transverse Strain

During testing under mechanical loading, the external strain was measured on the outer surfaces of both FRPC tubulars in the longitudinal and hoop directions of the global coordinate system. Note that a global coordinate system is aligned with the pipe axis, whereas a local coordinate system corresponds to the directions parallel and transverse to the fiber direction. The coordinate system transformation of global strains to local strains, for a lamina subjected to purely axial tensile traction, with specimens that are filament wound with $\pm\theta^\circ$ layers, is developed in Eq. [3-12], Eq. [3-13], and Eq. [3-14] [5]. The transformation from global to local strains is given in Eq. [3-12].

$$\begin{bmatrix} \varepsilon_x \\ \varepsilon_y \\ \frac{\gamma_{xy}}{2} \end{bmatrix} = \begin{bmatrix} \cos^2 \theta & \sin^2 \theta & -2 \sin \theta \cos \theta \\ \sin^2 \theta & \cos^2 \theta & 2 \sin \theta \cos \theta \\ \sin \theta \cos \theta & -\sin \theta \cos \theta & \cos^2 \theta - \sin^2 \theta \end{bmatrix} \begin{bmatrix} \varepsilon_1 \\ \varepsilon_2 \\ \frac{\gamma_{12}}{2} \end{bmatrix} \quad [3-12]$$

It is assumed that during testing the specimens are installed in perfect alignment, and only tensile loads are applied, i.e., the shear strains are zero, which leads to the simplification of Eq. [3-12], shown as Eq. [3-13]

$$\begin{bmatrix} \varepsilon_x \\ \varepsilon_y \end{bmatrix} = \begin{bmatrix} \cos^2 \theta & \sin^2 \theta \\ \sin^2 \theta & \cos^2 \theta \end{bmatrix} \begin{bmatrix} \varepsilon_1 \\ \varepsilon_2 \end{bmatrix} \quad [3-13]$$

As all of the tubular specimens were filament wound with $\pm 60^\circ$ layers, the transformation matrix is further simplified by replacing the cosine and sine terms with their respective mathematical values, as shown in Eq. [3-14].

$$\begin{bmatrix} \varepsilon_x \\ \varepsilon_y \end{bmatrix} = \begin{bmatrix} 0.25 & 0.75 \\ 0.75 & 0.25 \end{bmatrix} \begin{bmatrix} \varepsilon_1 \\ \varepsilon_2 \end{bmatrix} \quad [3-14]$$

3.4 Results

3.5 Benchtop Tests

3.5.1 Minimum Pressure versus Number of Layers

Single-wall FRPC specimens were evacuated to the minimum pressure attainable, 1.33 Pa (10^{-2} Torr), utilizing the vacuum system. This was achieved by pumping for periods ranging from 8 to 65 hours. A plot of the minimum achievable pressure versus number of layers, for each tubular specimen, is shown in Figure 3-1. Note the error bars represent the range of measured starting pressures. The test data from the four, six, and eight layer specimens is available in Appendix sections A and B.

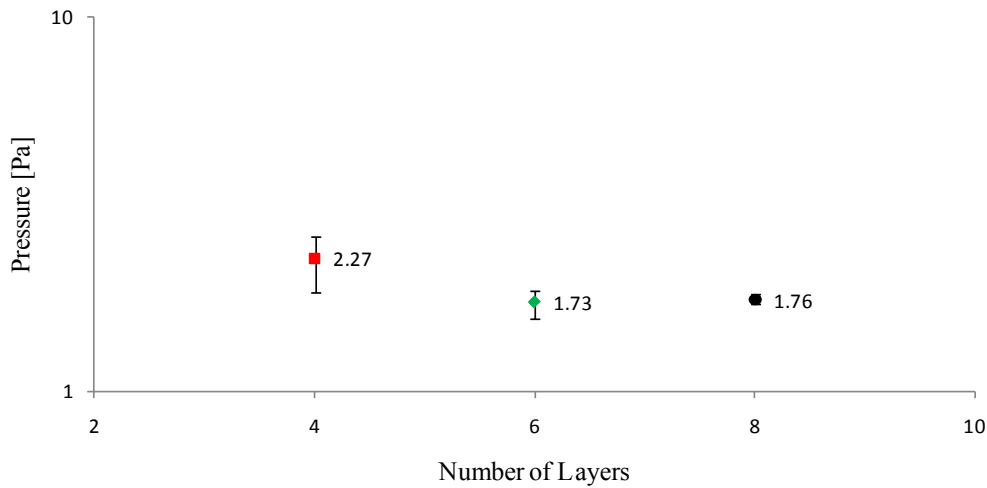


Figure 3-1: Benchtop comparison of range of starting pressure (logarithmic scale) versus number of layers

3.5.2 Mass Flow Rate and Intrinsic Permeability

In Table 3-1, test data including the calculated mass flow rates, intrinsic permeability coefficients, and the ‘initial pressure’ is shown. P_0 , the ‘initial pressure,’ is the minimum measured pressure that was achieved prior to starting the decay tests by isolating the specimen from the pump using the needle valve. Initial pressures on the order of 1.33 Pa (10^{-2} Torr) were consistently achieved, which indicate the FRPC pipes ability to hold a ‘medium’ vacuum level. Note that a ‘high’ vacuum level is commonly defined for pressures below $1.33 \times 10^{-1} \text{ Pa}$ (10^{-3} Torr). Pressures of $1.33 \times 10^{-1} \text{ Pa}$ were achieved for a capped vacuum system, without excess tubing, or composite specimens installed. Lower pressures were not possible due to system limitations, i.e. the type of fittings and size of tubing, as they choke the mass flow to the pump at decreasing pressure levels. However, the intrinsic permeability coefficients shown in Table 3-1 indicate that leakage for the FRPC tubes was minute prior to mechanical loading.

Table 3-1: Average test data for the benchtop configuration

# layers	\dot{m} [10^{-13} kg/s]	k' [10^{-23} m 2]	P _o [Pa]	# tests
4	158	48.3	2.27	3
6	4.92	2.25	1.73	4
8	14.1	8.24	1.76	3

3.6 Dual-Wall Specimens

3.6.1 Initial Pressure versus Load

The dual-wall FRPC specimens were evacuated to the minimum pressure attainable, 1.33 Pa (10^{-2} Torr), utilizing the vacuum system. This was achieved by pumping for periods ranging from 13 to 46 hours. A plot of the minimum achievable pressure versus number of layers, for each tubular specimen at the specified axial tension load is shown in Figure 3-2. Note that applied axial tension did not appear to have a strong effect on the minimum pressure attainable, although additional tests are required for certainty. In addition, the test data from the four, six, and eight layer specimens is available in Appendix sections A and B.

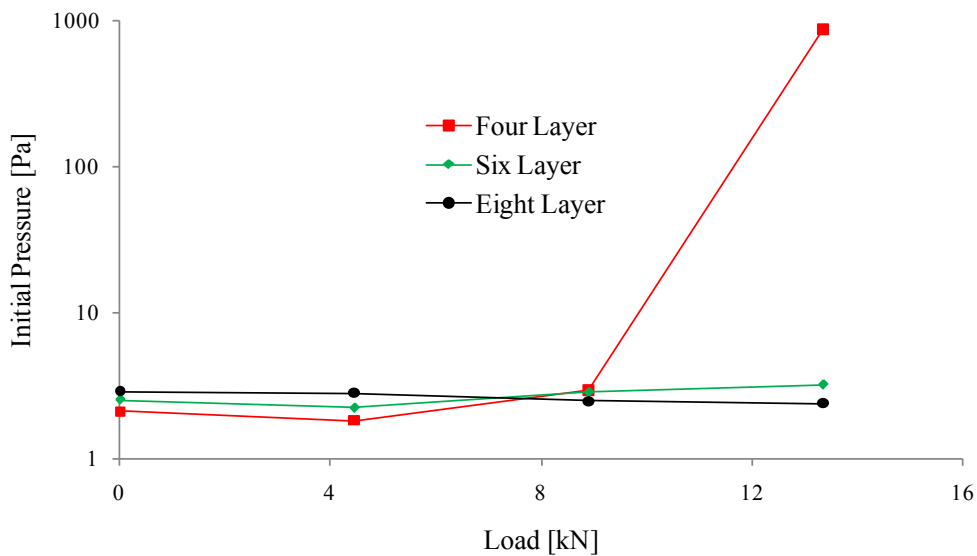


Figure 3-2: Dual-wall comparison of initial pressure (logarithmic scale) versus applied axial load

3.6.2 Mass Flow Rate and Intrinsic Permeability

During mechanical testing, axial loading occurred at a constant rate of 4.63 N/s (1.04 lb/s). The applied axial force was increased in stages up to a maximum load of 13.3 kN (3000 lbs). Initially, the tensile load was raised to 4.5 kN (1000 lbs), where the load was held constant for the duration of the pressure rise experiment, i.e., 10 hours. The vacuum pump was then reconnected, and the annular space was evacuated for an additional 13 hours. Subsequent test stages occurred for loads of 8.9 kN (2000 lbs), and 13.3 kN (3000 lbs) employing the same time intervals. Note that the mechanically loaded flanges were assembled using a press-fit technique with a compressive load of approximately 15.6 kN (3500 lbs). Therefore, axial forces of 4.5, 8.9 and 13.3 kN were chosen as they allow for three equally spaced loading conditions that do not exceed the critical tensile load for the mechanically loaded flanges, i.e., where they begin to pull apart, which occurs at a tensile load of 15.6 kN (3500 lbs).

The experimental results are shown in Table 3-2, Table 3-3, and Table 3-4 for specimens with four, six, and eight layers, respectively. Note that the specimens tested under the benchtop configuration had consistently lower leakage mass flow rates, which correspond to lower intrinsic permeability coefficients, compared with dual-wall specimens subjected to no axial load. Two explanations are proposed for this behavior: (a) the benchtop test setup deviates from the mechanical testing configuration for installation procedures, annulus vacuum port diameter, type of connections, and amount of tubing employed; (b) the dual-wall specimens may have been susceptible to a small amount of fluid leakage from the

hydraulic fluid filled inner tube (even though the NUTO H 46 hydraulic fluid has a kinematic viscosity that is 2.7 times higher than air at 40 °C) [6, 7].

From Table 3-2, Table 3-3, and Table 3-4, the four layer specimen was unique in exhibiting significantly higher leakage at the 13.3 kN (3000 lb) load level, which corresponds well to the resulting damage (cracking) visible on the surface of the specimen in Figure 3-3. The intrinsic permeability increases by four orders of magnitude (from 10^{-21} to 10^{-17} m^2), which correlates with the findings discussed in [4], i.e., leakage through FRPC tubular specimens occurs when a loading threshold is exceeded, leading to a sudden rise in leakage mass flow rate and a rapid increase in intrinsic permeability. Below this loading threshold, FRPC tubes remain practically impermeable. In addition, it is found in [8] the air permeability

Table 3-2: Values obtained for the four layer dual-wall specimen

Load [kN]	\dot{m} [10^{-11} kg/s]	k [10^{-21} m^2]	P _o [Pa]
0	3.37	1.67	2.13
4.45	3.02	1.27	1.87
8.90	2.88	1.42	2.93
13.3	108 720	79 059	8.80

Table 3-3: Values obtained for the six layer dual-wall specimen

Load [kN]	\dot{m} [10^{-11} kg/s]	k [10^{-21} m^2]	P _o [Pa]
0	4.17	1.95	2.53
4.45	3.25	1.54	2.27
8.90	3.38	1.55	2.80
13.3	118.05	54.92	3.20

Table 3-4: Values obtained for the eight layer dual-wall specimen

Load [kN]	\dot{m} [10^{-11} kg/s]	k [10^{-21} m^2]	P _o [Pa]
0	3.31	2.34	2.93
4.45	3.43	2.44	2.80
8.90	3.41	2.53	2.53
13.3	2.33	1.73	2.40

of prepreg composites to be on the order of 10^{-18} m^2 , which also correlates with the present findings.



Figure 3-3: A four layer dual-wall specimen, subjected to pure tensile loading, showing surface cracks in the hoop direction

3.6.3 Transverse Strain

3.6.3.1 Four layer

In Figure 3-4, the applied traction loads and resulting strain data is plotted against time, while axial stress versus axial strain is shown in Figure 3-5. The strain changes from linear to non-linear at 0.3% axial strain, for the external tube, corresponding to 0.2% transverse strain. An interesting observation from Figure 3-5 is the time dependent effect of the external tube (reminiscent of viscoelastic creep behaviour), which appears as an increase in the axial strain from 0.5% to 1% while no additional mechanical loading was applied. Note that the strain gauges were bonded to the external lamina of each tube, in the center of the gauge length. In Figure 3-4, the external strains increase sharply at 1.3 hours,

corresponding with the crack formation shown in Figure 3-3. Note the cracks on either side of the strain gauge can be observed. At a peak axial strain of about 3%, the mode I crack surfaces separate, leading to a disconnection across the outer lamina on both sides of the strain gauge, and a subsequent drop in axial strain.

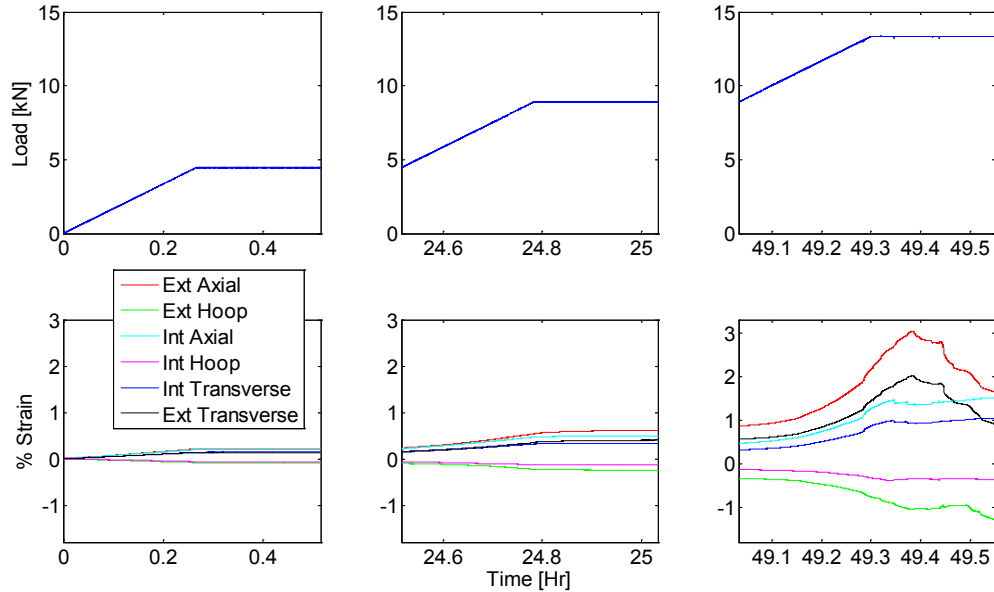


Figure 3-4: Load and % strain versus time for the four layer specimen

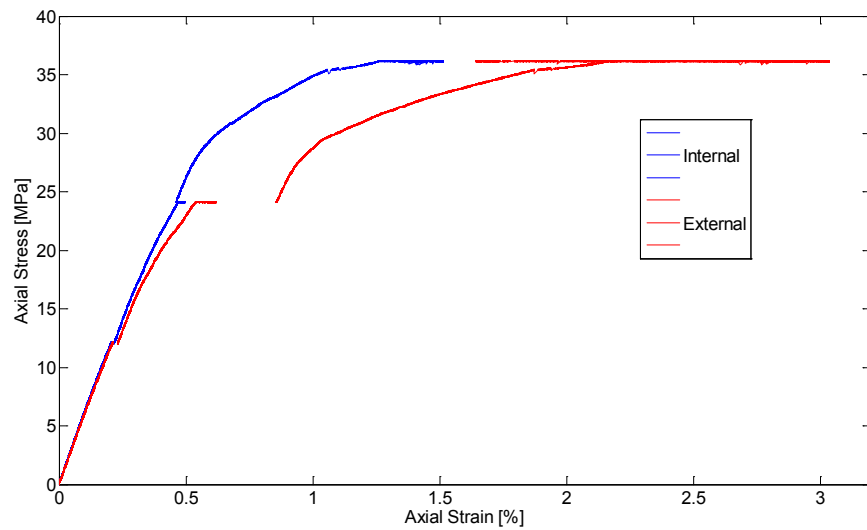


Figure 3-5: Axial stress versus strain for the four layer FRPC dual-wall specimen

However, the axial strain does not approach zero, as delamination does not occur between layers. Note in Figure 3-4 there is a time delay of 24 hours between subsequent loading cycles, i.e., between 4.5 and 8.9 kN, and between 8.9 and 13.3 kN.

3.6.3.2 Six layer

In Figure 3-6, applied traction loads and the resulting strain data is plotted against time. Strains exhibit linear behavior for all but the final loading step, where a non-linear strain response suggests the onset of crack formation, and mode I crack propagation. An increase in the permeability coefficient, shown in Table 3-3, corresponds with the strain increase at the particular loading state. Axial stress is plotted against axial strain in Figure 3-7. The stress appears to deviate from linear around an axial strain of 0.4%, which corresponds to a transverse strain of 0.27%. Note the time dependent strain increase (viscoelastic creep) visible in the four layer data is also present for the six layer specimen, shown in Figure 3-7, except it occurs for both tubes. Note in Figure 3-6 there is a time delay of 24 hours between subsequent loading cycles, i.e., between 4.5 and 8.9 kN, and between 8.9 and 13.3 kN, that is identical to the delay for the four layer specimen.

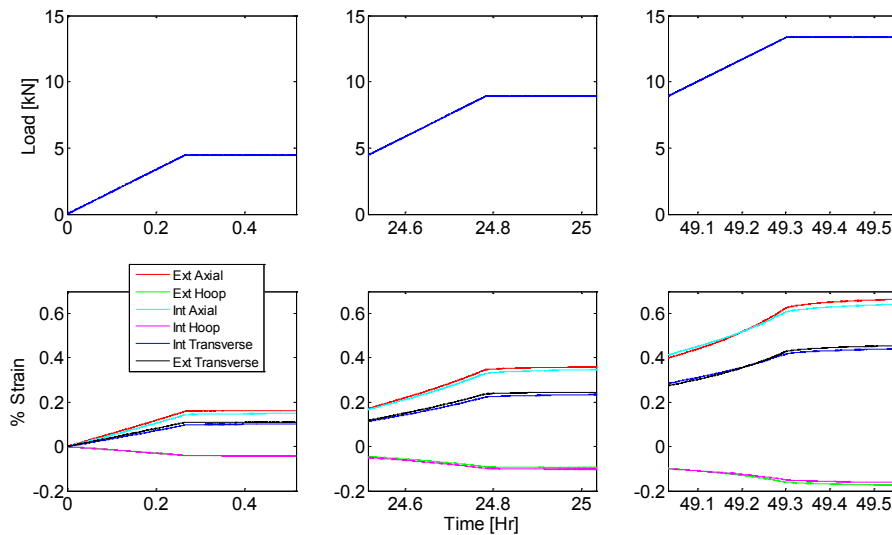


Figure 3-6: Load and % strain versus time for the six layer specimen

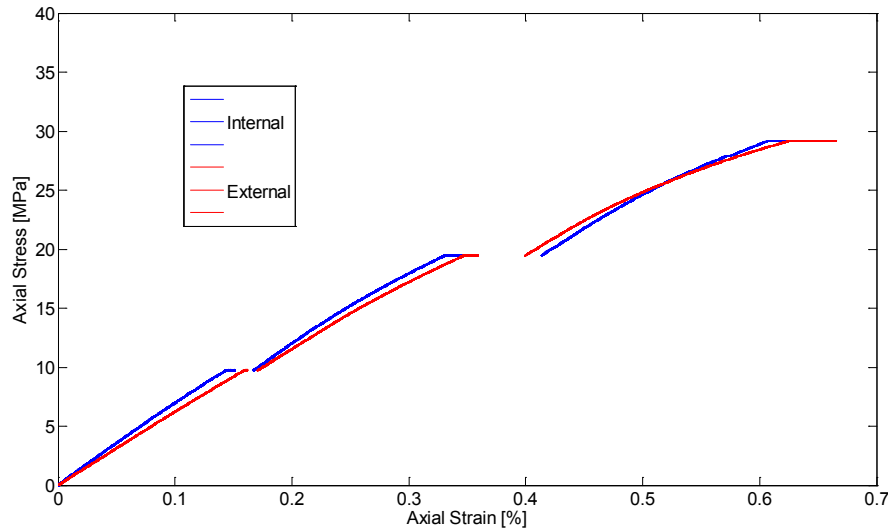


Figure 3-7: Axial stress versus strain for the six layer FRPC dual-wall specimen

3.6.3.3 Eight layer

In Figure 3-8, applied traction loads and the resulting strain data is plotted against time. The strains exhibit a linear profile for all loading states. In Figure 3-9, axial stress is plotted against axial strain. As previously displayed for the six layer tubes, the time dependent effect (viscoelastic creep) is also present

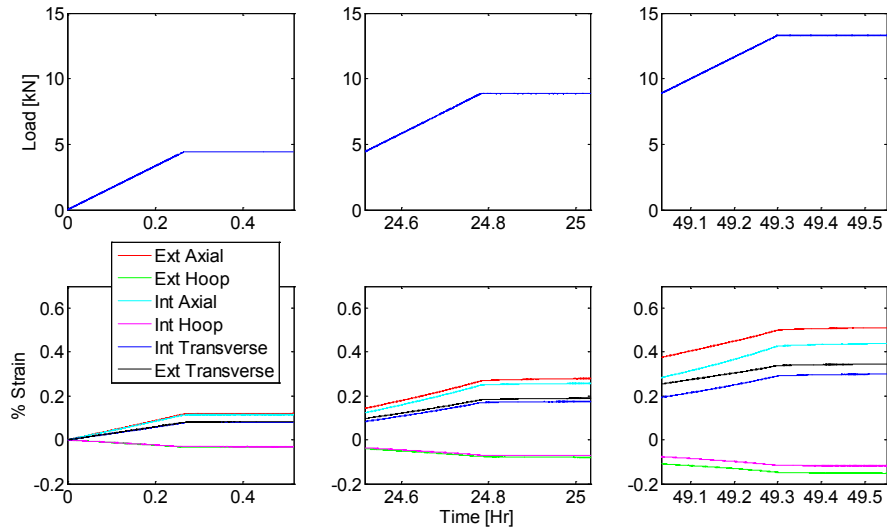


Figure 3-8: Load and % strain versus time for the eight layer specimen

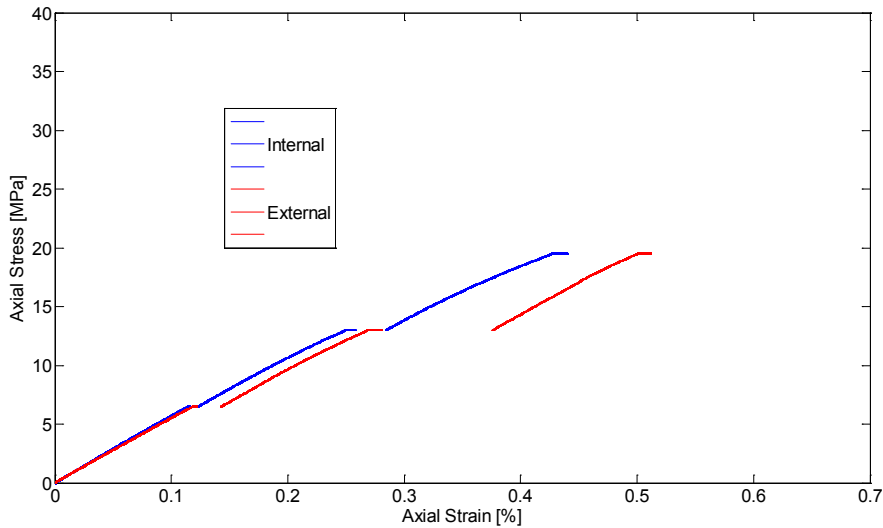


Figure 3-9: Axial stress versus strain for the eight layer FRPC dual-wall specimen

for the eight layer specimen, shown in Figure 3-9, as a strain increase between tests. Note in Figure 3-8 there is a time delay of 24 hours between subsequent loading cycles, i.e., between 4.5 and 8.9 kN, and between 8.9 and 13.3 kN, that is identical to the delays for the four and six layer specimens.

3.7 Intrinsic Permeability versus Transverse Strain

The intrinsic permeability coefficients were plotted against transverse strain for the four, six, and eight layer specimens as shown in Figure 3-10. The data points for the 13.3 kN (3000 lb) load from the four and six layer specimens are not shown, as they are for considerably higher permeability coefficients. It was reported in [4] that leakage failure in E-glass fiber/epoxy tubes while under pressure loads from hydraulic oil occurred at an average transverse strain of 0.3%. The basalt fiber/epoxy specimens investigated in this study show a quantitatively similar behavior, as leakage is absent for transverse strains below 0.3%.

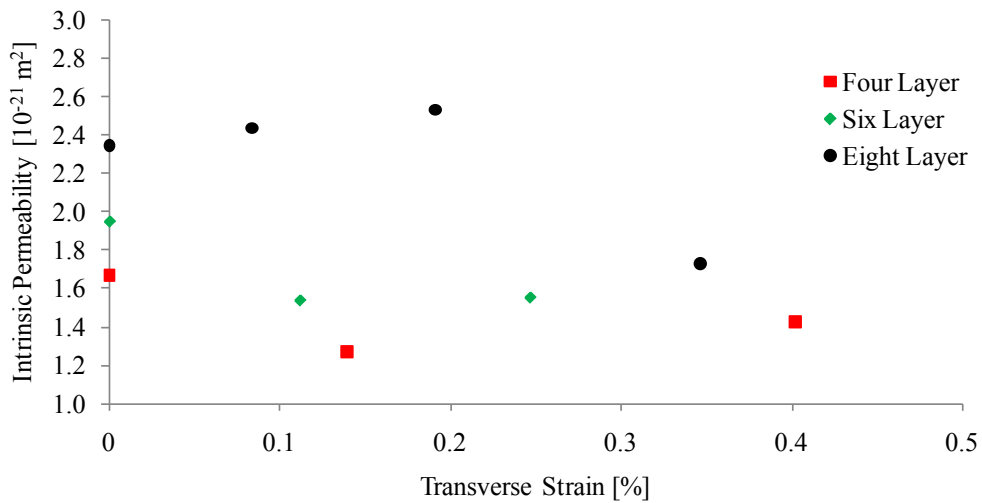


Figure 3-10: Intrinsic permeability versus transverse strain

It is interesting to note that in Figure 3-10 there is a drop in the permeability coefficients for each of the specimens, although they occur at different transverse strain values. This may be an effect of the resultant radial compressive loads, brought on by mechanical deformation, aiding in closing micro-cracks that are

present in the polymer matrix. However, a conclusive explanation with analytical and numerical models employing fracture mechanics was not explored in detail.

3.8 Conclusions

In this chapter tubular FRPC specimens were assessed for their ability to hold vacuum under two testing scenarios, i.e., a benchtop configuration for long-term testing of single-wall tubes, and a mechanical loading scenario for dual-wall tubes. The intrinsic permeability coefficients were derived from the measured pressure rise data and the following conclusions were drawn.

- Both experimental setups were suitable for measuring the vacuum holding capability of FRPC tubes. The benchtop configuration measures the minimum possible leakage rate for undamaged specimens, while the mechanical loading scenario provides a repeatable method for correlating leakage rate with load for dual-wall pipes.
- Leakage mass flow rates were used to determine intrinsic permeability coefficients for single-wall tubes without mechanical loading. The benchtop configuration proves FRPC tubular specimens are capable of holding a vacuum, but it decays slowly with time.
- The minimum achievable pressure for the present basalt/epoxy FRPC specimens is on the order of 1.33 Pa (10^{-2} Torr), which corresponds to a ‘medium’ vacuum level.

- Leakage mass flow rates were also used to determine permeability coefficients for dual-wall FRPC specimens under mechanical loading. The specimens exhibited significant leakage and pressure rise (vacuum decay) when under axial tension loadings causing polymer matrix cracking. A linear increase in leakage rate was not observed for transverse strains (to the fiber direction) below 0.3%.
- A slight drop in leakage mass flow rate was initially detected for subsequent increases in mechanical loading, for each specimen tested. Further analysis is required to explain this phenomenon.

The measured vacuum holding capability of basalt/epoxy FRPC specimens is encouraging, and further investigation into the feasibility of dual-wall pipes for insulation is prudent. The materials employed should be optimized to improve the vacuum holding performance, specifically to decrease the minimum achievable pressure beyond 1.33 Pa. In addition, the significance of vacuum pressure will be discussed in an economic analysis, which is presented in Chapter 5. There the viability of FRPC vacuum insulation for various working fluid case studies and pipe dimensions is highlighted, i.e. liquid natural gas, liquid nitrogen, and oil.

3.9 References

- [1] Ruhl M, Mertiny P. Diffusion and leakage in vacuum-insulated dual-wall composite piping. Proc. International SAMPE Symposium; 2010; Seattle, WA.
- [2] White FM. Fluid Mechanics. 5th ed. New York: McGraw-Hill; 2003.
- [3] Roy S, Benjamin M. Modeling of permeation and damage in graphite/epoxy laminates for cryogenic fuel storage. Compos Sci Technol. 2004;64:2051-2065.
- [4] Mertiny P, Gold A. Quantification of leakage damage in high-pressure fiber reinforced polymer composite tubular vessels. Polymer Testing. 2007;26:172-179.
- [5] Kaw AK. Mechanics of Composite Materials. 2nd ed. Boca Raton: CRC Press; 2006.
- [6] Çengel YA. Heat Transfer A Practical Approach. 2nd edition. New York: McGraw Hill; 2003.
- [7] Exxon Nuto H Series [homepage on the Internet]. Fairfax, VA: Exxon Mobil Corporation c2007 [cited 2010 May 13]. Available from:
<http://www.exxon.com/usa-english/lubes/pds/nausenindexnutoh.asp>
- [8] Sequeira Tavares S, Michaud V, Månsen, J-AE. Through thickness air permeability of prepgs during cure. Compos Part A Appl Sci Manuf. 2009; 40: 1587-1596.

4. THERMAL ANALYSIS*

Thermal management is necessary for various applications involving the transportation of working fluids, such as multi-phase fluids in oil exploration, liquefied natural gas (LNG), and liquid nitrogen (LN_2) for use in high temperature superconducting (HTS) cables. Vacuum insulation is useful, as it allows for the implementation of a high level of thermal resistance. In the following, a thermal analysis was conducted for oil flowing through the center of the inner tube, by varying the boundary properties of the case study, i.e., emissivity, annulus pressure, oil temperature, and number of lamina. The cases were modeled based on one-dimensional radial heat transfer for the specific measured dimensions of the manufactured four, six, and eight layer specimens. The thermal resistance equations were developed assuming the dual-wall pipes were surrounded by still air at 4°C , and the working fluid was transported through the center of the inner

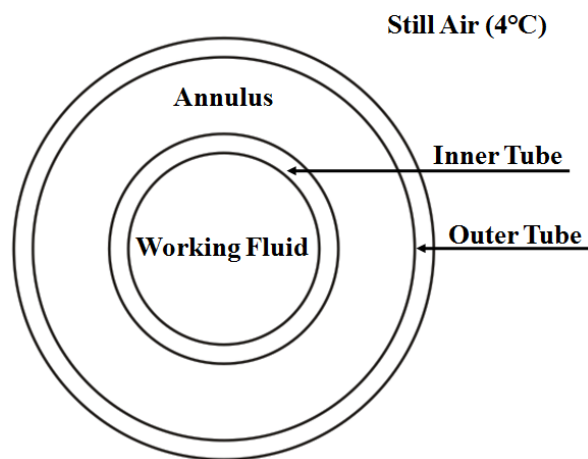


Figure 4-1: Outline of the model

* A version of this chapter was published in the conference proceedings of the 28th International Conference on Ocean, Offshore and Arctic Engineering [1].

tube at a velocity of 2 m/s. A two-dimensional slice of the thermodynamic model is shown in Figure 4-1.

4.1 Specimen Properties

A concentric dual-wall piping system contains inner and outer tubes, which are manufactured by utilizing the method discussed in section 2.3. The average wall thicknesses for the four, six, and eight layer specimens were measured as $1.26_{-0.32}^{+0.29}$ mm, $1.58_{-0.08}^{+0.12}$ mm, and $2.29_{-0.27}^{+0.18}$ mm, respectively. In addition, the average fiber volume content for the four, six, and eight layer specimens were $48.8_{-7.5}^{+8.2}\%$, $55.5_{-1.5}^{+1.3}\%$ and $55.0_{-1.8}^{+2.9}\%$, respectively.

4.2 Assumptions

In order to solve the system analytically, three base assumptions were required to simplify the problem, i.e., isothermal heat transfer occurs under steady state conditions, air is an ideal gas, and pipe sections with a unit length of 1 m are oriented horizontally.

The calculations were conducted for one-dimensional heat transfer in the radial direction [3], whereby $T = T(r)$ where T is temperature and r is the tube radius [1]. Simplifying Fourier's Law of Heat Conduction, the rate of heat transfer, \dot{Q} , is the ratio of the temperature gradient, ΔT , to the thermal resistance of a dual-wall piping system, R_T , as shown in Eq. [4-1] [3].

$$\dot{Q} = \frac{\Delta T}{R_T} \quad [4-1]$$

The thermal resistance component is a summation of the effective resistances of the components in the system, shown in Figure 4-2. They consist of the thermal resistance of the working fluid, $R_{\text{conv},1}$, the conduction resistance through the inner tube, $R_{\text{cond},1}$, the radiation and conduction resistances of the annulus, $R_{\text{rad},2-3}$ and $R_{\text{cond},2-3}$ respectively, the conduction resistance through the outer tube, $R_{\text{cond},2}$, and the radiation and convection resistances of heat transfer to the environment, $R_{\text{rad},4-\infty}$, and $R_{\text{conv},4-\infty}$, respectively.

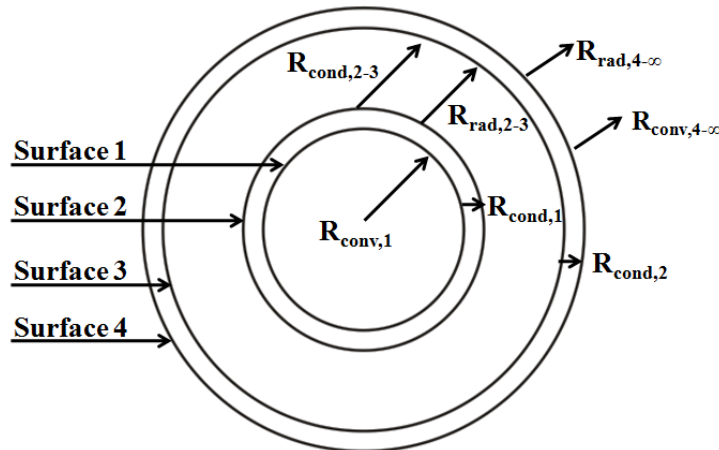


Figure 4-2: Thermal resistances in the model

4.3 Equations

The thermal resistance network for heat transfer through the dual-wall pipe model employs a combined series-parallel arrangement, shown in Eq. [4-2].

$$R_T = R_{\text{conv},1} + R_{\text{cond},1} + \frac{R_{\text{rad},2-3} \times R_{\text{cond},2-3}}{R_{\text{rad},2-3} + R_{\text{cond},2-3}} + R_{\text{cond},2} + \frac{R_{\text{rad},4-\infty} \times R_{\text{conv},4-\infty}}{R_{\text{rad},4-\infty} + R_{\text{conv},4-\infty}} \quad [4-2]$$

The thermal resistance to convection of the working fluid, $R_{\text{conv},1}$, and of the surrounding environment, $R_{\text{conv},2}$, are calculated using Eq. [4-3] [3].

$$R_{\text{conv}} = \frac{1}{h_{\text{conv}} A_s} \quad [4-3]$$

From Eq. [4-3], A_s is the heat transfer surface area, i.e., surface 1 or 4, and h_{conv} , the external convection heat transfer coefficient, is found using Eq. [4-4] [3].

$$h = \frac{Nu \times k_a}{D_o} \quad [4-4]$$

As two cases require Eq. [4-4] to calculate h , i.e., the working fluid and the surrounding air, they require separate coefficients. The average thermal conductivity, k_a , is a fluid property, D_o is the diameter of the heat transfer surface, and Nu is the Nusselt number, which is 3.66 for the working fluid [3]. The Nusselt number for the surrounding air is calculated using Eq. [4-5] [3].

$$Nu = \left\{ 0.6 + \frac{0.387 Ra_D^{1/6}}{\left[1 + \left(0.559 / Pr \right)^{9/16} \right]^{8/27}} \right\}^2 \quad [4-5]$$

The Prandtl number, Pr , which is a fluid property accessible from Tables [3], and the Rayleigh number, Ra_D , are required to solve for the Nusselt number in

Eq. [4-5]. The Rayleigh number is calculated using Eq. [4-6], and must be below the critical number of 1.0×10^{12} [3], or a different version of Eq. [4-5] is required.

$$Ra_D = \frac{g\beta(T_s - T_\infty)L_c^3}{\nu^2} P_r \quad [4-6]$$

From Eq. [4-6], g , the gravitational acceleration constant (9.81 m/s^2), β , the coefficient of volume expansion, T_s , the external surface temperature of the outer pipe, T_∞ , the air temperature, ν , the kinematic viscosity, L_c , the outer diameter of the pipe, and the Prandtl number are required. In addition, β is calculated from Eq. [4-7] where T_f is the absolute film temperature of the air (K), approximated as the average between T_s and T_∞ [3].

$$\beta = \frac{1}{T_f} \quad [4-7]$$

The conduction resistance of each cylinder layer, R_{cond} , is calculated separately, and requires knowledge of the outer radius, r_o , inner radius, r_i , the unit pipe length (1 m), L , and the average thermal conductivity of the pipe wall, k_p , as shown in Eq. [4-8].

$$R_{\text{cond}} = \frac{\ln\left(\frac{r_o}{r_i}\right)}{2\pi L k_p} \quad [4-8]$$

The thermal conductivity for pure resin, k_m , is 0.21 W/m/K [4], and the thermal conductivity for basalt rock, k_f , is 1.513 W/m/K [5]. The average thermal conductivity of the FRPC wall, shown in Eq. [4-9], takes into account the relative

proportions of fiber and matrix, represented by the fiber and matrix volume fractions, V_f and V_m , respectively.

$$k_p = V_f k_f + V_m k_m \quad [4-9]$$

The thermal resistance against radiation, R_{rad} , is calculated separately for two cases, i.e., the outer pipe, and across the annulus. In Eq. [4-10], the thermal resistance against radiation for the outer pipe, $R_{rad,4-\infty}$, is calculated using $h_{rad,4-\infty}$, the radiation heat transfer coefficient, and A_4 [3].

$$R_{rad,4-\infty} = \frac{1}{h_{rad,4-\infty} A_4} \quad [4-10]$$

The radiation heat transfer coefficient, shown in Eq. [4-11], requires the surface emissivity, $\underline{\varepsilon}$, the Stefan-Boltzmann constant ($5.6704 \times 10^{-8} \text{ W/m}^2\text{K}^4$), σ , and the absolute temperatures of the surface and environment, T_s and T_∞ , respectively [3].

$$h_{rad,4-\infty} = \underline{\varepsilon} \sigma (T_s^2 + T_\infty^e) (T_s + T_\infty) \quad [4-11]$$

The radiation heat transfer rate across the annulus, denoted as surfaces ‘2’ and ‘3’, is given by Eq. [4-12], and the radiation heat transfer coefficient by Eq. [4-13] [3].

$$\dot{Q}_{rad,2-3} = \underline{\varepsilon}^* \sigma A_2 (T_2^4 - T_3^4) \quad [4-12]$$

$$h_{\text{rad},2-3} = \frac{\dot{Q}_{\text{rad},2-3}}{A_2(T_2 - T_3)} \quad [4-13]$$

The thermal resistance of the annulus to radiation, which is shown in Eq. [4-14], is derived by substituting Eq. [4-12] into Eq. [4-13], and placing the resultant expression for the radiation heat transfer coefficient into Eq. [4-10]. Note that the view factor for concentric cylinders is 1.

$$R_{\text{rad},2-3} = \frac{(T_2 - T_3)}{\underline{\varepsilon}^* \sigma (T_2^4 - T_3^4) A_2} \quad [4-14]$$

For infinitely long concentric cylinders, the effective emissivity, $\underline{\varepsilon}^*$, is determined from Eq. [4-15] where $\underline{\varepsilon}_2$ and $\underline{\varepsilon}_3$ are the emissivity's of the bounding annular surfaces, 2 and 3 [3].

$$\underline{\varepsilon}^* = \frac{1}{\frac{1}{\underline{\varepsilon}_2} + \frac{1 - \underline{\varepsilon}_3}{\underline{\varepsilon}_3} \left(\frac{r_2}{r_3} \right)} \quad [4-15]$$

The thermal resistance to conduction in the annulus is calculated from Eq. [4-16], where the average thermal conductivity of the air, K_e , is calculated from Eq. [4-17] [6,7,8]

$$R_{\text{cond}} = \frac{\ln\left(\frac{r_o}{r_i}\right)}{2\pi L K_e} \quad [4-16]$$

The thermal conductivity of the air remaining in a vacuum depends on the thermal conductivity of air at room temperature and pressure (0.0284 W/m/K), K_0 , [6], the absolute average temperature (K), T , the annulus pressure (Pa), P , and the

annulus thickness (m), Δx , as shown in Eq. [4-17]. Note that T is the average temperature of the bounding annular surfaces, 2 and 3.

$$K_e = \frac{K_0}{1 + 7.6 \times 10^{-5} \frac{T}{P\Delta x}} \quad [4-17]$$

Furthermore, note that if the mean free path of the transmitting fluid, i.e., air, is greater than 10 mm, which occurs for pressures below 1.33 Pa (10^{-2} Torr) [6], heat transfer in the annulus is due to a conduction mechanism, over natural convection. An alternative deterministic method employs the calculation of F_{cyl} , as shown in Eq. [4-18] [3], and requires the length of the dual-wall pipe, L_c , and the inner and outer diameters of the bounding annular surfaces, D_o and D_i , respectively.

$$F_{cyl} = \frac{\left[\ln\left(\frac{D_o}{D_i}\right) \right]^4}{L_c^3 \left(D_i^{-3/5} + D_o^{-3/5} \right)^5} \quad [4-18]$$

Natural convection is considered negligible if $F_{cyl}Ra_L < 100$ and $0.70 \leq Pr \leq 6000$, where Ra_L is calculated from Eq. [4-6] [3].

4.4 Analysis

Three variables were considered to determine their effect on the total thermal resistance, i.e., emissivity, air pressure, and number of FRPC layers. The effect of applying low emissivity coatings to one or both surfaces was also examined. Note that the surface 1 wall temperature is assumed to be identical to

the working fluid (oil) at a temperature of 60 °C. Furthermore, note that thermal resistance is plotted against effective emissivity, calculated using Eq. [4-15]. An iterative approach with appropriate convergence was required to solve for thermal resistance and heat flux, as T_3 and \dot{Q} were initially unknown quantities.

4.4.1 Emissivity, Air Pressure, and Pipe Wall Thickness

Emissivity and air pressure were changed to determine their effect on the total thermal resistance for the four, six, and eight layer pipes. Emissivity coatings were varied from 0.005 to 1 for constant pressures of 1.33×10^{-7} Pa (10^{-9} Torr), 1.33×10^{-2} Pa (10^{-4} Torr), 1.33 Pa (10^{-2} Torr) and 101.325 kPa (760 Torr). Note that surfaces 2 and 3 had identical emissivity coatings. In Figure 4-3, a constant annulus pressure of 1.33 Pa was assumed. It is shown that the differences in thermal resistance between the various layers are small for each emissivity. The

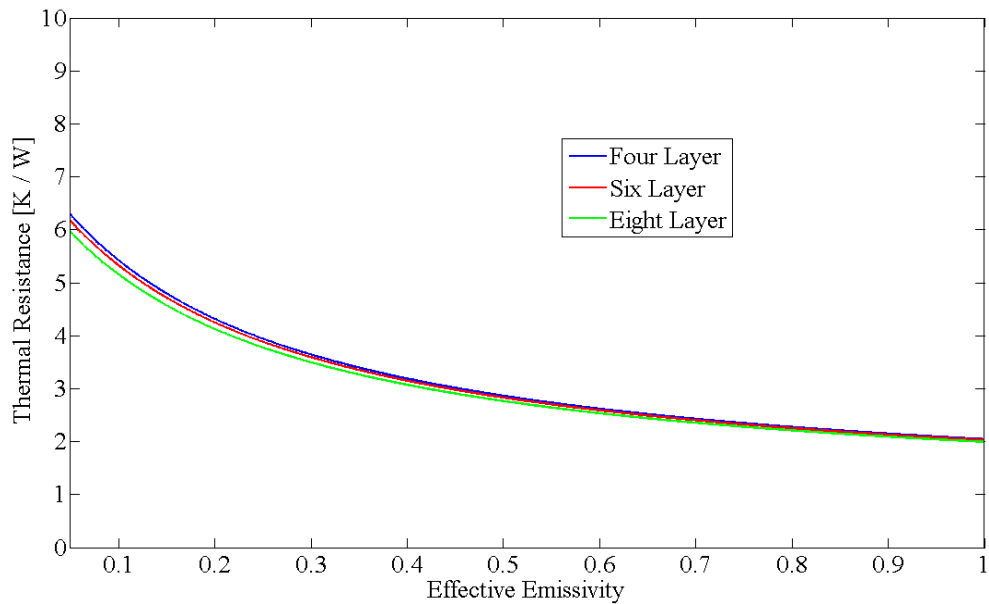


Figure 4-3: Thermal resistance versus effective emissivity for an annulus pressure of 1.33 Pa

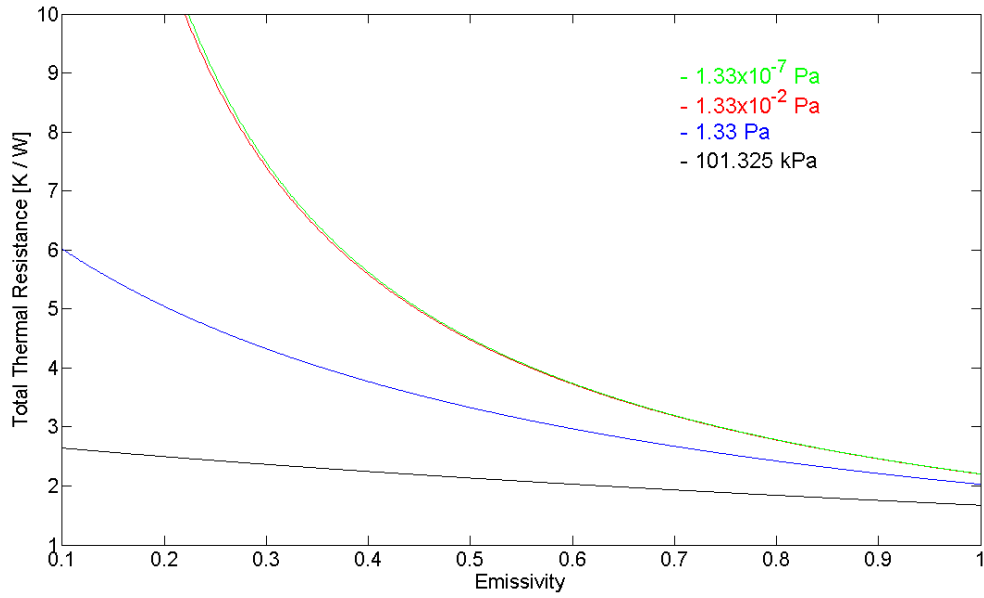


Figure 4-4: Thermal resistance versus emissivity for the six layer FRPC pipe

same effect is seen for annulus pressures of 1.33×10^{-7} Pa, 1.33×10^{-2} Pa, and 101.325 kPa, and the small differences make showing the thermal resistance trends in the present text redundant.

The effect of changing annulus air pressure on thermal resistance is shown in Figure 4-4 for a six layer FRPC dual-wall pipe. Note that figures for four and eight layer specimens were omitted here and instead are included in Appendix C, as they show identical trends and similar numerical values.

From Figure 4-4, the thermal resistance increases exponentially with decreasing emissivity. A significant increase in resistance occurs by dropping the annulus pressure from 101.325 kPa to 1.33 Pa, but an even larger increase occurs by dropping the annulus pressure from 1.33 Pa to 1.33×10^{-2} Pa. Decreasing the annulus pressure below 1.33×10^{-2} Pa has less of an effect, except for very low

emissivity coatings, e.g., 0.005. Note that an annulus pressure of 1.33×10^{-2} Pa can be achieved by employing a mechanical vacuum pump, while pressures of 1.33×10^{-7} Pa require additional vacuum systems, i.e., oil diffusion pumps with cold traps, and liquid cryogenic pumps [9], and significantly longer pumping times.

4.4.2 Low Emissivity Coatings on One or Both Surfaces

The effect of applying various low emissivity surface coatings to either the radiation emitting or absorbing surfaces, or both, is explored. In the case where only a single surface is coated, the radiation absorbing surface is assumed to be a black body ($\varepsilon = 1$), while the radiation emitting surface was assigned emissivity values ranging from 0.005 to 1. When both surfaces are coated, they are assigned identical emissivity values ranging from 0.005 to 1. The resultant thermal

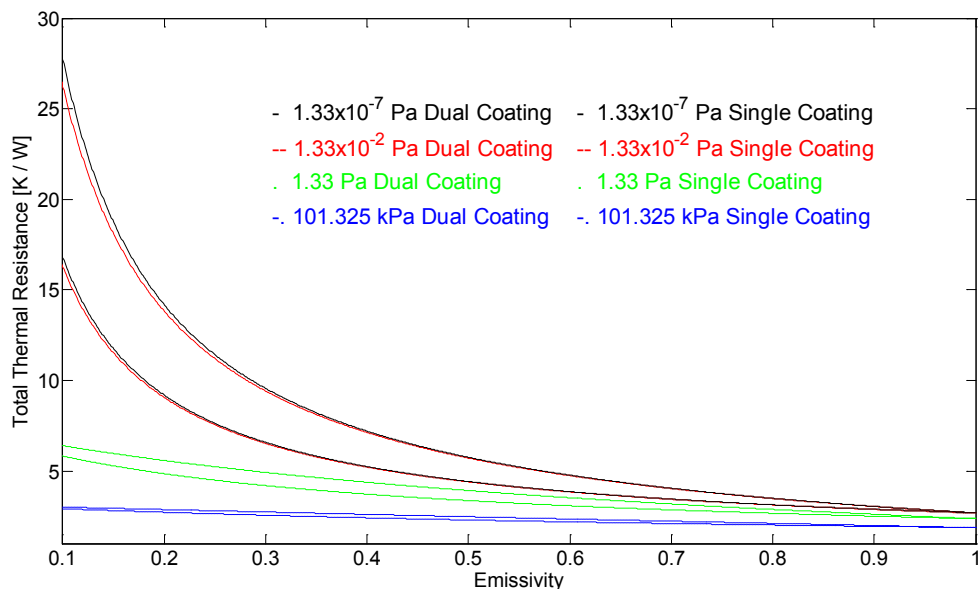


Figure 4-5: Comparison of single and dual-wall effective emissivity coatings for six layer FRPC pipes

resistance is plotted against the effective emissivity, calculated using Eq. [4-15], and shown in Figure 4-5. Note that in Figure 4-5 the single and dual-wall coatings are represented with identical line style and color parameters, but remain distinguishable as the dual-wall coating maintains a larger total thermal resistance at each effective emissivity. A slight increase in total thermal resistance occurs when both surfaces are coated versus only the radiating surface for annulus pressures of 101.325 kPa and 1.33 Pa. Furthermore, the difference in total thermal resistance at pressures of 10^{-2} Pa compared with 10^{-7} Pa is minuscule for the single or dual-wall coatings. However, the total thermal resistance is significantly higher for dual-wall coatings versus single-wall coatings at pressures below 10^{-2} Pa when low emissivity values, i.e., 0.1 or lower, are employed. Note that only the six layer FRPC data is included in the body of text; the four and eight layer FRPC specimen data shows similar trends, and was included in Appendix C.

4.5 Conclusions

In this chapter an analytical thermal model was created for dual-wall specimens that employ vacuum insulation. Model parameters including emissivity, annulus pressure, and number of layers were varied to determine their effect on the overall thermal resistance. The following conclusions were drawn from the resulting model data.

- An analytical model was created to determine the thermal resistance, and heat flux, for dual-wall FRPC pipes of unit length (1 m).

- Thermal resistance increases with decreasing annulus pressure and effective emissivity, although the effect is less significant for pressures that are lower than 1.33×10^{-2} Pa when utilizing an effective emissivity between 0.3 and 1.
- Thermal resistance increases exponentially with decreasing emissivity.
- An annulus pressure of 1.33×10^{-2} Pa, which is the lowest achievable pressure for a mechanical vacuum pump, corresponds to a high thermal resistance.
- The thermal resistance of four, six, and eight layer FRPC specimens are effectively identical.
- The thermal resistance for single and dual-wall emissivity coatings is effectively identical.

The thermal resistance model was used for the economic viability case studies presented in the next chapter. It is an effective way to generate theoretical thermal resistance values for vacuum insulated dual-wall pipes with various working fluids, emissivity coatings, and boundary temperatures. However, the validity of the model should be tested in an experimental setup by measuring the heat flux for various boundary conditions, emissivity coatings, and vacuum pressures.

4.6 References

- [1] Ruhl M, Juss K, Mertiny P. Novel Vacuum-Insulated Dual-Wall Composite Pipe for Cold Environment Applications. Proc. 28th International Conference on Ocean, Offshore and Arctic Engineering; 2009 31 May – 5 June; Honolulu, HI.
- [2] Wolodko J, Mertiny P, Meijer G, Martens M, Ellyin F. Development of a facility for filament winding GFRP tubulars. Proc. 46th International SAMPE Symposium; 2001; Long Beach, CA, pp. 1271-1282.
- [3] Çengel YA. Heat Transfer A Practical Approach. 2nd edition. New York: McGraw Hill; 2003.
- [4] Evseeva LE, Tanaeva SA. Thermal Conductivity of Micro- and Nanostructural Epoxy Composites at Low Temperatures. Mechanics of Composite Materials. 2008;44(1):87-92.
- [5] Gunerhan H, Hepbasli A. Utilization of Basalt Stone as a Sensible Heat Storage Material. Energy Sources. 2005;27:1357-1366.
- [6] Ediss GA. Effect of Vacuum Pressure on the Thermal Loading of the ALMA Cryostat [monograph on the Internet]. ALMA Memo 554; 2006 [cited 2009 Dec 14]. Available from: <http://www.alma.nrao.edu/memos/html-memos/alma554/memo554.pdf>
- [7] Potkay JA, Lambertus GR, Sacks RD, Wise KD. A Low-Power Pressure-and Temperature-Programmable Micro Gas Chromatography Column. J Microelectromech Syst. 2007;16(5):1071-1079.

[8] General Electric Company (US) Corporate Research and Development. Fluid Flow Data Book. May 1982. Section 410.2.

[9] Sit JC. ECE 558 Micro- and nanofabrication topics I. Edmonton: University of Alberta Course Notes; 2005.

5. ECONOMIC ANALYSIS*

Thermal management is required to maintain a working fluid within favorable operating parameters for various applications, such as the transmission of multi-phase fluids (e.g., oil slurries), fuels (e.g., liquefied natural gas (LNG)), and for the containment of liquid nitrogen (LN_2) as a coolant and insulation in high-temperature superconducting (HTS) cables. Vacuum insulation and low emissivity coatings increase a pipes' thermal resistance, which allows for working fluids to be maintained within their optimal temperature range with minimal energy input. FRPC pipes also have beneficial material properties over conventional steels, i.e., corrosion resistance, a high fatigue life, and strength-to-weight ratio. Furthermore, resins, fibers, weave angles, and fiber volume fractions can be customized for each pipe based on the required application, e.g., a near zero-axial thermal expansion pipe for LNG transport.

In Chapter 3 the vacuum holding capability of the lab-tested four, six, and eight layer dual-wall basalt/epoxy FRPC specimens was determined while loaded to 4.5 kN (1000 lb) axial tension. Corresponding findings were used to determine the maximum pipe length that could be serviced by a specific vacuum source (i.e., a dual-stage rotary vane mechanical vacuum pump), at a specific annulus pressure and temperature. Note that only the six layer pipes were analyzed. Based on the SPL, the calculated heat flux from chapter 4, and the case specific temperature

* A version of this chapter was published in the Proceedings of The Canadian Society for Mechanical Engineering Forum (CSME) 2010, June 7-9, 2010, Victoria, British Columbia, Canada [1].

boundary conditions and fluid thermal properties, the economic costs were determined for thermally managing three working fluids, i.e., LNG, LN₂, and 60 °C oil. Furthermore, the example working fluids were studied for two specific dual-wall FRPC pipe cases to test for scaling effects, i.e. small-scale six layer, and larger ‘industrial-sized’ pipes.

A normalized yearly power cost (*NYPC*) was introduced, and is the ratio of the total yearly energy requirement, assuming continuous operation for the pipe under study compared to a single-wall steel pipe (of the same ID) insulated with urethane foam. The *NYPC* was calculated for each pipe configuration in each of the three case studies assuming the energy input is required to (i) power a continuously running vacuum pump to establish a vacuum in the annulus, and (ii) power a heat pump to offset the heat flux for 4°C still air surrounding the pipes. Note the chosen still air temperature corresponds to the average annual temperature of the city of Edmonton, Alberta, Canada. The temperature is unfavorable for vacuum-insulated FRPC pipe, as a larger temperature gradient more strongly favors a vacuum-insulated dual-wall FRPC pipe over a baseline single-wall urethane-insulated steel pipe.

5.1 Specimen Fabrication and Properties

The lab tested six layer FRPC samples were manufactured utilizing an industrial filament winding system and materials delineated in section 2.3, and had fiber volume fractions as described in section 4.1. The thermal conductivity

of the inner and outer FRPC specimens were determined to be 0.950 W/m/k, and 0.935 W/m/K respectively, based on the method from Chapter 4.

For the concentric dual-wall industrial-sized pipe case studies, the geometry and structure were assumed whereby inner and outer concentric tubes were sized by a geometric scaling factor of 12. The inner and outer pipes have inside diameters (ID) of 457.2 mm and 609.6 mm, and a wall thickness of 18.96 mm.

Urethane insulation was employed to compare single-wall insulated AISI-316 stainless steel pipe to the vacuum insulated dual-wall FRPC pipe, in an effort to measure the cost effectiveness of vacuum insulation over a ‘next best’ option. Note the capital costs associated with manufacturing FRPC versus steel pipelines, maintenance of the vacuum insulation, and the application of urethane insulation are ignored to simplify the analysis. In each case study the urethane layer has the same thickness as the vacuum insulated annulus, as an attempt was made to keep the overall pipe diameter comparable for the various case studies. In addition, the thermal conductivity of urethane insulation is 0.026 W/m/K [4], and the thermal conductivity of the steel pipes is 42.7 W/m/K [5].

5.2 Analytical Thermal Analysis

The equations developed in chapter 4 were employed to calculate the heat flux and thermal resistance for concentric dual-wall pipes with varying boundary conditions. The effective emissivity of the radiation resistance component was calculated by assuming that polyurethane liners can be chemically bonded to basalt/epoxy FRPC pipes [6]. In addition, a 60% polyurethane/aluminum flake

powder coating with a thickness of 40 μm has an emissivity of 0.027 [7]. Furthermore, for infinitely long cylinders, the effective emissivity ($\underline{\varepsilon}^*$) of an annulus depends on the radius and emissivity of the radiation emitting and absorbing surfaces, as shown in Eq. [4-15]. Therefore, the application of a 40 μm polyurethane/aluminum coating to both surfaces results in an effective emissivity of 0.015.

5.3 Heat Flux

For comparing the yearly electrical costs between the various case studies, a method was required to add the electrical requirements of the vacuum pump to the heat lost, or gained, by the pipe. A solution was procured by assuming a heat pump provides the necessary heating, or cooling. The rate of heat loss, or gain, \dot{Q} , is converted to the work input power of the heat pump cycle, \dot{W}_{cycle} , by dividing by the heat pumps' maximum theoretical coefficient of performance, γ_{\max} , when reversible processes are utilized [8], as shown in Eq. [5-1].

$$\dot{W}_{\text{cycle}} \geq \frac{\dot{Q}}{\gamma_{\max}} \quad [5-1]$$

The theoretical maximum coefficient of performance for a heat pump is calculated from Eq. [5-2] [8], where T_L is the lower boundary temperature (the surrounding still air at 4 $^{\circ}\text{C}$), and T_H is the upper boundary temperature (the working fluid). Note that T_H and T_L must be given as absolute temperatures, such as on the Kelvin scale [8].

$$\gamma_{\max} = \frac{1}{1 - \frac{T_L}{T_H}} \quad [5-2]$$

5.4 Pump Properties and Serviceable Pipe Length

The vacuum pump employed to evacuate the dual-wall FRPC pipe annulus during the leakage mass flow rate experiments of chapter 3, is a 746 W (1 hp) dual-stage rotary vane mechanical vacuum pump, and has a volumetric flow rate, \dot{V}_{pump} , of 11.9 m³/hr (7 cfm) [9]. The maximum mass flow rate of the vacuum pump, \dot{m}_{pump} , when air is discharged at the minimum achievable annulus pressure of 1.33 Pa (10⁻² Torr) [3], is given by Eq. [5-3] [10].

$$\dot{m}_{\text{pump}} = \frac{M}{RT} p \dot{V}_{\text{pump}} \quad [5-3]$$

Where M is the molar mass of air (28.97 kg/kmol), R is the universal gas constant (8.3145 kJ/kmol/K), T is the absolute temperature of the remaining air in the annulus (K), and p is the target annulus air pressure (Pa). Note the temperature of the annulus air is approximated as the average temperature of the two bounding annular surfaces (2 and 3). Furthermore, note the maximum mass flow rate was also calculated for annulus pressures of 101,325 Pa (760 Torr), 13,332 Pa (10² Torr), 1,333 Pa (10¹ Torr), 133 Pa (1 Torr), 13.3 Pa (10⁻¹ Torr), 1.33×10⁻¹ Pa (10⁻³ Torr), 1.33×10⁻² Pa (10⁻⁴ Torr), and 1.33×10⁻⁷ Pa (10⁻⁹ Torr).

The SPL was calculated for each case study and annulus pressure by employing Eq. [5-4], and utilizing the leakage mass flow rate for the lab-tested six

layer specimens, \dot{m}_{test} , their test length, L_{test} , and the maximum mass flow rate of the vacuum pump, \dot{m}_{pump} , given by Eq. [5-3]. Note that SPL varies directly with annulus pressure and inversely with temperature as shown in Eq. [5-3].

$$L_{max} = \frac{\dot{m}_{pump} L_{test}}{\dot{m}_{test}} \quad [5-4]$$

5.5 Air Flow Characterization

The air flow in an annulus subjected to a vacuum pump falls into three categories, i.e. continuum (Cont), transitional (Tstl), or molecular (Mlcr) [10]. Eq. [5-5] is used to determine whether the flow is continuum or molecular, depending on the calculated air characterization parameter, S , where p is the air pressure, and D_h is the hydraulic diameter of the annulus, given by Eq. [5-6] [10], and where D_o and D_i are the outer and inner diameters, respectively.

$$S = pD_h \quad [5-5]$$

$$D_h = \frac{D_o^2 - D_i^2}{2(D_o + D_i)} \quad [5-6]$$

If S is greater than $6.4 \text{ mbar}\times\text{mm}$ ($1.89\times10^{-1} \text{ Torr}\times\text{in}$) the flow is continuum, and if it is less than $0.0604 \text{ mbar}\times\text{mm}$ ($1.78\times10^{-3} \text{ Torr}\times\text{in}$) the flow is molecular. The air flow characterization for the small and large pipes with oil (60°C) as the working fluid is shown in Table 5-1. Note the LNG and LN₂ tables have slightly different \dot{m}_{pump} values, but identical magnitudes, and are included in Appendix D.

Table 5-1: Air Flow Characteristics for Oil at 60 °C

Annulus Pressure [Pa]	\dot{m}_{pump} [kg/s]	Small Pipe S [mbar×mm]	Label	Large Pipe S [mbar×mm]	Label
101,325	3.822×10^{-3}	4,710	Cont	56,517	Cont
13,332	5.029×10^{-4}	619.7	Cont	7,437	Cont
1,333	5.029×10^{-5}	61.97	Cont	743.7	Cont
133	5.029×10^{-6}	6. 197	Tstl	74.37	Cont
13.3	5.029×10^{-7}	$6. 197 \times 10^{-1}$	Tstl	7.437	Cont
1.33	5.029×10^{-8}	$6. 197 \times 10^{-2}$	Tstl	7.437×10^{-1}	Tstl

5.6 Abbreviations and Equations for Economic Analysis

The total yearly energy requirement, E , for each pipe is shown in Eq. [5-7], and combines the work input power of the heat pump, \dot{W}_{cycle} , and vacuum pump, \dot{W}_{vp} , for a specific pipe length, L . Note that the total yearly energy requirement assumes the heat pump and vacuum pump run continuously for a year. Furthermore, the total yearly energy requirement for all case studies was adjusted for comparison purposes by multiplying by a length factor, i.e., $1000/L$ where L is the SPL for the specific case under study. Thus, the economic analysis was performed for pipes with an effective SPL of 1,000 m.

$$E = (\dot{W}_{\text{cycle}}L + \dot{W}_{\text{vp}}) \times \frac{1000}{L} \quad [5-7]$$

The Normalized Yearly Power Cost, $NYPC$, is the ratio of the total yearly energy requirement for the pipe under study (E_{pipe}) compared with a single-wall urethane-insulated steel pipe (E_{SWU}) of the same ID, shown in Eq. [5-8].

$$NYPc = \frac{E_{\text{pipe}}}{E_{\text{SWU}}} \quad [5-8]$$

Yearly Savings Over Urethane foam insulation (*YSOU*) represents the savings a particular pipe has over a single-wall urethane-insulated steel pipe of the same ID, as shown in Eq. [5-9].

$$YSOU = C_e (E_{\text{SWU}} - E_{\text{pipe}}) \quad [5-9]$$

The heat loss per outer pipe surface area, \dot{Q}/A_s , the work of the heat pump cycle, \dot{W}_{cycle} , the total energy required to run the heat and vacuum pumps continuously for a year, E , the normalized thermal resistance, NR_T , and the yearly savings over a single-wall urethane-insulated steel pipe, *YSOU*, are shown in Table 5-2, Table 5-3, and Table 5-4. Note that the normalized values are compared to a single-wall urethane-insulated steel pipe of the same ID. In addition, the *YSOU* values are calculated assuming the cost of electricity, C_e , is a constant value of \$0.10 per kWhr.

5.7 Case Studies

The cost savings of employing vacuum insulation was examined for three working fluids contained in the inner pipe of dual-wall FRPC piping, i.e. 60 °C oil, LN₂ at 72 K, and LNG at 111 K, for lab-tested and industrial-sized piping. In each case study, the annulus was subjected to the following air pressures: 101,325 Pa, 1.33×10^4 Pa, corresponding to a ‘low vacuum’; 1.33×10^3 Pa, 1.33×10^2 Pa, 1.33×10^1 Pa, 1.33 Pa, 1.33×10^{-1} Pa, corresponding to a ‘medium

vacuum;’ 1.33×10^{-2} Pa corresponding to ‘high vacuum;’ and 1.33×10^{-7} Pa corresponding to ‘ultra-high vacuum.’ Additional parameters specific to each case study are given in the following.

5.7.1 Oil

The thermal conductivity of oil at 60 °C is 0.1404 W/m/K [11].

5.7.2 Liquid Nitrogen

LN_2 at an absolute temperature of 72 K, is the working fluid, and has a thermal conductivity of 5×10^{-3} W/m/K [13]. A target heat flux to area ratio, \dot{Q}/A_s , was calculated for each pipe, and compared with the goal of 5 W/m^2 set by [12].

5.7.3 Liquefied Natural Gas

LNG at an absolute temperature of 111 K is the working fluid. Note that the thermal conductivity of LNG is approximated by that of liquid methane, i.e., 0.1863 W/m/K [11].

5.8 Results and Discussion

In the figures that follow, i.e., Figure 5-1, Figure 5-2, and Figure 5-3, certain acronyms, i.e., 6LDW, 6LDWU, LIDW, LIDWU, SS, SSU, LSS, and LSSU, are used to identify various pipe configurations. The 6LDW acronym represents a small-scale six layer dual-wall FRPC pipe, 6LDWU represents a

6LDW pipe with urethane insulation covering the outer pipe, LIDW represents industrial-sized dual-wall FRPC pipe, LIDWU represents a LIDW pipe with urethane insulation covering the outer pipe, SS represents single-wall steel pipe with the same ID as the small-scale FRPC pipe, SSU represents SS with urethane insulation, LSS represents large industrial-sized single layer steel pipe, and LSSU represents LSS with urethane insulation.

In the results that follow, Table header P indicates the annulus pressure, \dot{Q}/A_s is the heat loss per outer pipe surface area, E is the total energy required to run the heat pump and vacuum pump continuously for one year, NR_T is the normalized total thermal resistance, $YSOU$ is the yearly savings over a single-wall urethane-insulated steel pipe, and E_{vp}/E_{hp} is the ratio of energy required by the vacuum pump to the heat pump.

5.8.1 Oil

The results of the case study for oil containment at 60 °C are summarized in Figure 5-1 and Table 5-2. The data shows that employing a medium annulus pressure (133 and 13.3 Pa) does not make vacuum-insulated dual-wall FRPC pipe economically viable. However, inclusion of an additional layer of urethane insulation to a medium pressure vacuum-insulated dual-wall pipe provides a significant improvement for small-scale and industrial-sized pipe, as shown in Table 5-2. Urethane insulation changes the $YSOU$ from -\$332 to \$396, and from -\$776 to \$956 for small-scale and industrial-sized dual-wall FRPC pipe, respectively, when an annular pressure of 133 Pa is applied. However, for high

and ultra-high vacuum levels the effect of additional urethane insulation on YSOU was negligible, and the achievable gains of \$396 and \$956 per SPL are negligible considering the time and length of pipe involved. Furthermore, for annulus pressures in the high and ultra-high vacuum range, considerably higher annual losses would be realized because the SPL length requires a prohibitive number of vacuum pumps to achieve the required annulus pressure.

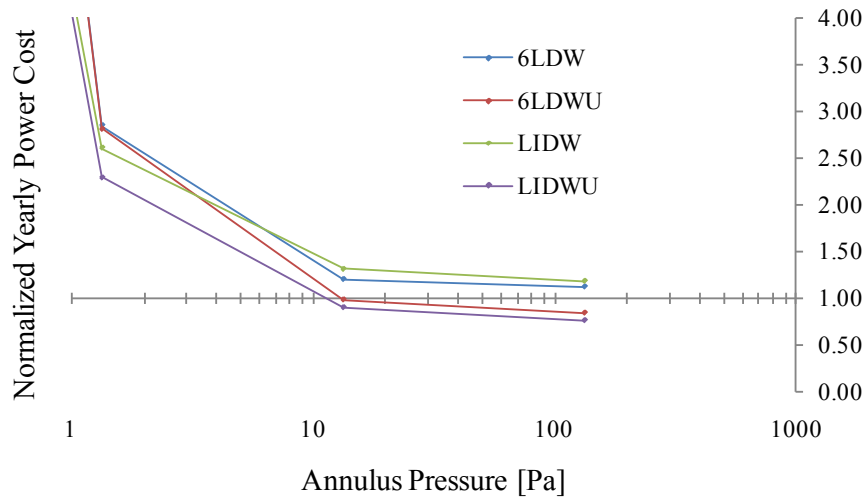


Figure 5-1: NYPC versus model parameter for oil at 60°C

Table 5-2: Data for 60 °C Oil

Case	P [Pa]	\dot{Q}/A_s [W/m ²]	E [kWhr]	NR _T	YSOU [\$]	E _{vp} / E _{hp}
6LDW	133	118.10	30,054	0.91	-332	0.023
6LDWU	133	75.76	22,779	1.21	396	0.030
LIDW	133	16.12	48,781	0.85	-776	0.014
LIDWU	133	8.79	31,465	1.33	956	0.022
6LDW	13.3	102.90	32,193	1.04	-546	0.257
6LDWU	13.3	68.26	26,570	1.34	17	0.334
LIDW	13.3	15.90	54,002	0.86	-1,298	0.138
LIDWU	13.3	8.72	37,184	1.34	384	0.218

Table 5-2 continued... Data for 60 °C Oil

Case	P [Pa]	\dot{Q}/A_s [W/m ²]	E [kWhr]	NR _T	YSOU [\$]	E _{vp} / E _{hp}
6LDW	1.33	47.59	76,260	2.26	-4,952	5.439
6LDWU	1.33	35.95	75,380	2.55	-4,864	6.183
LIDW	1.33	14.07	107,079	0.98	-6,606	1.548
LIDWU	1.33	8.05	94,462	1.45	-5,344	2.350
6LDW	1.33×10^{-1}	10.96	636,023	9.81	-60,929	232.255
6LDWU	1.33×10^{-1}	9.10	637,355	10.06	-61,062	238.837
LIDW	1.33×10^{-1}	7.96	665,284	1.73	-62,426	26.980
LIDWU	1.33×10^{-1}	5.35	670,265	2.19	-62,924	34.747
6LDW	1.33×10^{-2}	4.85	6,312,365	22.16	-628,563	5,231.266
6LDWU	1.33×10^{-2}	4.10	6,318,688	22.37	-629,195	5,285.193
LIDW	1.33×10^{-2}	4.44	6,375,003	3.09	-633,398	479.385
LIDWU	1.33×10^{-2}	3.35	6,443,604	3.50	-640,258	548.913
6LDW	1.33×10^{-7}	4.12	$630,832 \times 10^6$	26.10	$-63,083 \times 10^6$	$615,729 \times 10^3$
6LDWU	1.33×10^{-7}	3.48	$631,370 \times 10^6$	26.29	$-63,137 \times 10^6$	$620,768 \times 10^3$
LIDW	1.33×10^{-7}	3.85	$635,256 \times 10^6$	3.57	$-63,526 \times 10^6$	$55,267 \times 10^3$
LIDWU	1.33×10^{-7}	2.96	$641,581 \times 10^6$	3.96	$-64,158 \times 10^6$	$61,886 \times 10^3$
SS	-	235.38	45,192	0.59	-1,846	-
SSU	-	113.77	26,737	1.00	0	-
LSS	-	44.76	103,126	0.40	-6,210	-
LSSU	-	14.55	41,023	1.00	0	-

5.8.2 Liquid Nitrogen

Figure 5-2 presents results for the case of dual-wall FRPC pipe containing LN₂ (e.g., HTS systems). The data indicates that additional urethane insulation in combination with a low (101.325 kPa, 13.332 kPa) or medium annulus pressure (1.333 kPa, 133 Pa, 13.3 Pa) is required to make vacuum insulation economically viable for small-scale and industrial-sized dual-wall FRPC pipe. Furthermore, data presented in Table 5-3 shows that savings per SPL of \$246 and \$317 can be achieved respectively, for pressures greater than 13.3 kPa and up to atmospheric (101.325 kPa). Note that savings of \$246 and \$317 per SPL are negligible considering the time and length of pipe involved, as was found for oil containment at 60 °C. Data in Table 5-3 also indicates that small-scale FRPC pipe

surpasses the target heat flux to area ratio of 5 W/m^2 for ultra-high vacuum pressures, i.e., $1.33 \times 10^{-7} \text{ Pa}$ (10^{-9} Torr), which is not feasible through the means of only a mechanical pump. Note the minimum achievable pressure for a mechanical vacuum pump is $1.33 \times 10^{-2} \text{ Pa}$ (10^{-4} Torr).

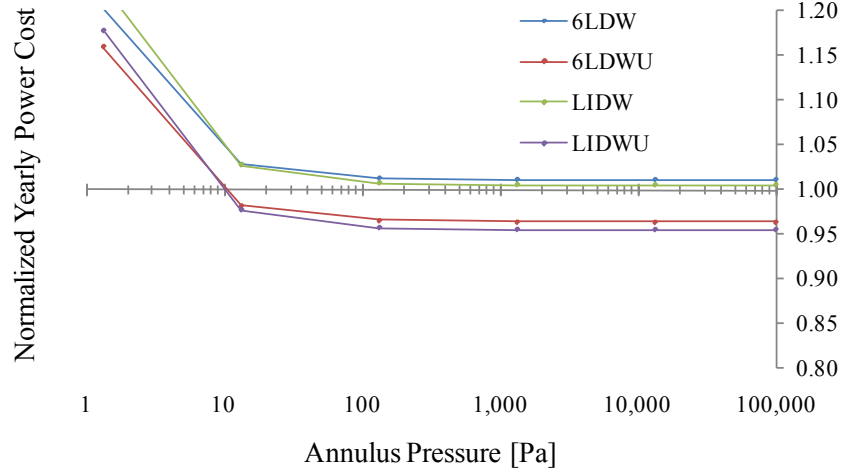


Figure 5-2: NYPC versus annulus pressure for LN_2

Table 5-3: Data for Liquid Nitrogen

Case	P [Pa]	\dot{Q}/A_s [W/m ²]	E [kWhr]	NR _T	YSOU [\$]	E_{vp}/E_{hp}
6LDW	101,325	63.74	69,850	0.99	-77	3.038×10^{-6}
6LDWU	101,325	51.84	66,624	1.04	246	3.173×10^{-6}
LIDW	101,325	5.44	71,538	0.99	-37	2.972×10^{-6}
LIDWU	101,325	4.41	67,990	1.05	317	3.114×10^{-6}
6LDW	13,332	63.74	69,851	0.99	-77	2.309×10^{-5}
6LDWU	13,332	51.84	66,625	1.04	246	2.412×10^{-5}
LIDW	13,332	5.44	71,540	0.99	-38	2.258×10^{-5}
LIDWU	13,332	4.41	67,992	1.05	317	2.367×10^{-5}
6LDW	1,333	63.73	69,862	0.99	-78	2.309×10^{-4}
6LDWU	1,333	51.83	66,636	1.04	245	2.412×10^{-4}
LIDW	1,333	5.44	71,554	0.99	-39	2.258×10^{-4}
LIDWU	1,333	4.41	68,006	1.05	316	2.367×10^{-4}
6LDW	133	63.70	69,971	0.99	-89	2.312×10^{-3}
6LDWU	133	51.81	66,748	1.04	233	2.413×10^{-3}
LIDW	133	5.44	71,697	0.99	-53	2.259×10^{-3}
LIDWU	133	4.41	68,148	1.05	302	2.367×10^{-3}

Table 5-3 continued... Data for Liquid Nitrogen

Case	P [Pa]	\dot{Q} / A_s [W/m ²]	E [kWhr]	NR _T	YSOU [\$]	E _{vp} / E _{hp}
6LDW	13.3	63.37	71,069	0.99	-199	2.339×10^{-2}
6LDWU	13.3	51.55	67,875	1.04	121	2.441×10^{-2}
LIDW	13.3	5.44	73,120	1.00	-196	2.261×10^{-2}
LIDWU	13.3	4.41	69,569	1.05	160	2.369×10^{-2}
6LDW	1.33	60.02	83,043	1.05	-1,396	2.625×10^{-1}
6LDWU	1.33	48.97	80,095	1.10	-1,101	2.726×10^{-1}
LIDW	1.33	5.41	87,443	1.00	-1,628	2.283×10^{-1}
LIDWU	1.33	4.39	83,860	1.05	-1,270	2.391×10^{-1}
6LDW	1.33×10^{-1}	33.72	290,779	1.87	-22,170	6.868
6LDWU	1.33×10^{-1}	28.20	286,948	1.91	-21,787	6.916
LIDW	1.33×10^{-1}	5.17	239,256	1.05	-16,809	2.516
LIDWU	1.33×10^{-1}	4.20	234,924	1.10	-16,376	2.622
6LDW	1.33×10^{-2}	7.45	3,366,817	8.46	-329,773	4.115×10^2
6LDWU	1.33×10^{-2}	6.31	2,355,614	8.52	-228,653	2.895×10^2
LIDW	1.33×10^{-2}	3.35	2,421,963	1.62	-235,080	5.406×10^1
LIDWU	1.33×10^{-2}	2.77	1,943,163	1.67	-187,200	4.449×10^1
6LDW	1.33×10^{-7}	3.31	$349,011 \times 10^6$	19.04	$-34,901 \times 10^6$	9.621×10^7
6LDWU	1.33×10^{-7}	2.81	$348,606 \times 10^6$	19.16	$-34,861 \times 10^6$	9.667×10^7
LIDW	1.33×10^{-7}	1.57	$302,552 \times 10^6$	3.45	$-30,255 \times 10^6$	1.468×10^7
LIDWU	1.33×10^{-7}	1.30	$301,014 \times 10^6$	3.55	$-30,101 \times 10^6$	1.500×10^7
SS	-	87.44	73,927	0.93	-484	-
SSU	-	66.76	69,082	1.00	0	-
LSS	-	7.51	76,221	0.93	-506	-
LSSU	-	5.73	71,164	1.00	0	-

5.8.3 Liquefied Natural Gas

Data for the case of LNG transmission pipes is given in Figure 5-3 and Table 5-4, and shows that small-scale and industrial-size dual-wall FRPC pipe utilizing vacuum insulation with medium pressures in the annulus are economically viable. Considerable savings per SPL, i.e. approximately \$11,800 can be realized with the small-scale pipe at this pressure level (1.33 Pa), and if a layer of urethane foam insulation is added, savings per SPL increase to approximately \$14,500. If the annulus pressure is further decreased to the range of

high vacuum levels (1.33×10^{-2} Pa), a loss of approximately \$367,000 is achieved.

For industrial-size pipe a medium quality vacuum insulation (1.33×10^{-1} Pa)

achieves a loss of approximately \$2,300 per SPL while addition of a layer of urethane foam insulation produces a savings of approximately \$13,700.

Furthermore, application of high quality vacuum insulation (1.33×10^{-2} Pa)

realizes losses of over \$353,000 per SPL.

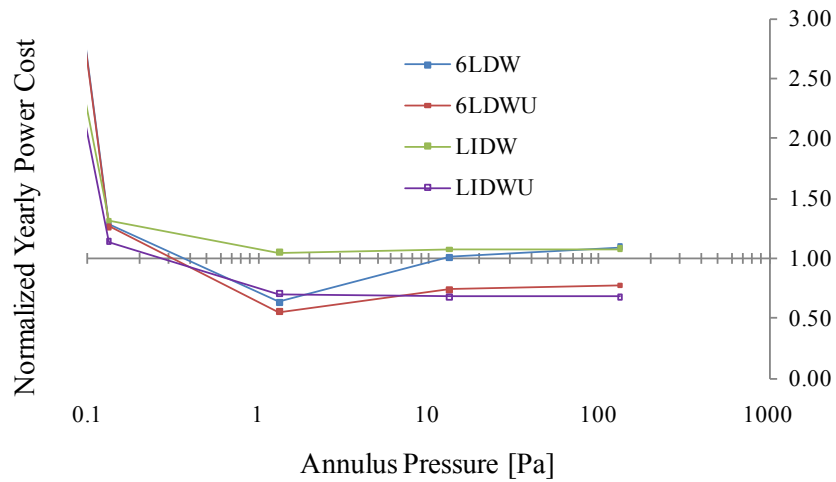


Figure 5-3: NYPC versus annulus pressure for LNG

Table 5-4: Data for Liquefied Natural Gas

Case	P [Pa]	\dot{Q} / A_s [W/m ²]	E [kWhr]	NR _T	YSOU [\$]	E _{vp} /E _{hp}
6LDW	133	412.04	361,293	0.91	-3,198	0.001
6LDWU	133	249.33	256,467	1.29	7,285	0.001
LIDW	133	48.27	507,798	0.92	-3,913	0.001
LIDWU	133	25.88	319,443	1.47	14,922	0.001
6LDW	13.3	377.67	334,109	1.00	-479	0.010
6LDWU	13.3	235.70	245,161	1.36	8,416	0.012
LIDW	13.3	47.80	505,944	0.93	-3,728	0.007
LIDWU	13.3	25.74	320,427	1.48	14,824	0.010
6LDW	1.33	199.60	210,449	1.88	11,887	0.204
6LDWU	1.33	146.67	184,195	2.19	14,512	0.222
LIDW	1.33	43.50	492,525	1.02	-2,386	0.077
LIDWU	1.33	24.37	331,592	1.56	13,707	0.104

Table 5-4 continued... Data for Liquefied Natural Gas

Case	P [Pa]	\dot{Q}/A_s [W/m ²]	E [kWhr]	NR _T	YSOU [\$]	E _{vp} / E _{hp}
6LDW	1.33×10^{-1}	36.13	422,695	10.40	-9,338	12.354
6LDWU	1.33×10^{-1}	30.06	417,004	10.66	-8,769	12.499
LIDW	1.33×10^{-1}	23.15	617,965	1.93	-14,930	1.539
LIDWU	1.33×10^{-1}	15.70	536,547	2.42	-6,788	1.772
6LDW	1.33×10^{-2}	7.15	3,999,412	52.59	-367,010	637.728
6LDWU	1.33×10^{-2}	6.04	3,989,809	53.05	-366,049	641.770
LIDW	1.33×10^{-2}	6.61	4,006,014	6.74	-353,735	56.612
LIDWU	1.33×10^{-2}	5.08	3,888,196	7.49	-341,953	61.107
6LDW	1.33×10^{-7}	3.68	$400,544 \times 10^6$	102.02	$-40,054 \times 10^6$	$124,087 \times 10^3$
6LDWU	1.33×10^{-7}	3.12	$400,063 \times 10^6$	102.73	$-40,006 \times 10^6$	$124,801 \times 10^3$
LIDW	1.33×10^{-7}	3.52	$397,434 \times 10^6$	12.68	$-39,743 \times 10^6$	$10,752 \times 10^3$
LIDWU	1.33×10^{-7}	5.08	$391,419 \times 10^6$	13.86	$-39,142 \times 10^6$	$11,579 \times 10^3$
SS	-	1096.97	741,416	0.44	-41,210	-
SSU	-	487.24	329,317	1.00	0	-
LSS	-	196.13	1,590,748	0.29	-112,208	-
LSSU	-	47.21	468,663	1.00	0	-

5.9 Conclusions

Data was amalgamated to provide information regarding the suitability of vacuum-insulated dual-wall piping for various case studies. The analysis was based on the vacuum holding capability of six layer dual-wall FRPC pipe subjected to an axial traction load of 4.45 kN (1000 lbs), thermal resistance equations for modeling pipe performance, and the thermal conductivity of air in a vacuum [14]. The case studies considered pipes containing oil at 60 °C, liquefied natural gas, and liquid nitrogen. In addition, two pipe configurations were utilized for the analysis, i.e., the laboratory tested small-scale pipe, and industrial-size pipe with a geometric scaling factor of 12. For economic comparison of the various case studies, a heat pump was employed to maintain the working fluid at its operating temperature, and resulting energy requirements were combined with

the electrical consumption of a continuously operating vacuum pump. Resulting data for each case was compared to a single-wall steel pipe, of the same inner diameter, with external urethane foam insulation. The following conclusions were drawn from the results:

- An optimum annulus pressure exists for maximizing the economic viability of vacuum insulated dual-wall FRPC pipe, by comparing YSOU values for a specific SPL.
- Further application of urethane foam insulation to an already vacuum-insulated dual-wall FRPC pipe has a greater effect for medium vacuum compared with high and ultra-high vacuum pressures.
- For oil flowing at 60 °C, a small-scale dual-wall FRPC pipe with medium vacuum pressure (1.33 Pa) and a layer of urethane foam insulation will not provide any significant savings (i.e., \$396 per SPL, while industrial-size pipe will save \$956).
- For LN₂, small-scale and industrial-size pipe require vacuum and urethane foam insulation to realize economic viability, although significant savings are not achieved, i.e., a small-scale dual-wall FRPC pipe with a low quality vacuum (13.3 kPa) will save \$246 per SPL, while industrial-size pipe will save \$317.
- For LNG, small-scale or industrial-size pipe is economically viable for medium quality vacuum insulation. A small-scale dual-wall

FRPC pipe with medium quality vacuum insulation (1.33 Pa) combined with urethane foam insulation will save \$14,500 per SPL while industrial-size pipe will save \$13,700.

- LNG with an annulus pressure of 1.33 Pa is the only application that achieves significant economic benefits over urethane foam insulated steel pipe, when using the current dual-wall vacuum-insulated basalt/epoxy design.

Depending on the application, vacuum insulation technology may, or may not be, economically viable. It was shown that LNG holds the most potential for economic viability, compared with LN₂ or oil applications, based on the current vacuum holding and leakage rate capability of basalt/epoxy dual-wall FRPC pipe. However, economic savings are possible for each of the three case studies if the leakage mass flow rate is significantly reduced, or larger vacuum pumps are employed to utilize economies of scale.

5.10 References

- [1] Ruhl M, Mertiny P. The economic benefit of dual-wall FRPC piping: a case study. Proc. of The Canadian Society for Mechanical Engineering Forum; Victoria; 2010.
- [2] Wolodko J, Mertiny P, Meijer G, Martens M, Ellyin F. Development of a facility for filament winding GFRP tubulars. Proc. 46th International SAMPE Symposium; 2001; Long Beach, CA, pp. 1271-1282.
- [3] Ruhl M, Mertiny P. Diffusion and leakage in vacuum-insulated dual-wall composite piping. Proc. International SAMPE Symposium; 2010; Seattle, WA.
- [4] Çengel YA. Heat Transfer A Practical Approach. 2nd edition. New York: McGraw Hill; 2003.
- [5] eFunda: Properties of Alloy Steel AISI 4140 [homepage on the Internet]. Sunnyvale, CA: eFunda, Inc. c2010 [cited 2010 Feb 10]. Available from: http://www.efunda.com/materials/alloys/alloy_steeels/show_alloy.cfm?ID=AISI_4140&prop=all&Page_Title=AISI%204140
- [6] Juss K, Mertiny P. Fabrication and Performance of a Novel Polyurethane-Lined Fibre-Reinforced Composite Pipe. Proc. Canadian Society for Mechanical Engineering Forum; Ottawa; 2008.
- [7] Yan X, Xu G. Corrosion and mechanical properties of polyurethane/Al composite coatings with low infrared emissivity. J Alloys Compd. 2010;491:649-653.

- [8] Moran MJ, Shapiro HN. Fundamentals of Engineering Thermodynamics. 5th ed. John Wiley & Sons, Inc.; 2004.
- [9] Leybold D8 D8A Trivac Rotary Vane Dual Stage Mechanical Vacuum Pump Rebuilt Refurbished [homepage on the Internet]. [cited 2010 Jan 7]. Available from: <http://www.pchendlabs.com/product.asp?pid=649>
- [10] Chambers A. Modern Vacuum Physics. Boca Raton: CRC Press LLC; 2005.
- [11] Çengel YA. Heat Transfer A Practical Approach. 2nd edition. New York: McGraw Hill; 2003.
- [12] Schippl K. Very Low Loss Cryogenic Envelope for long HTS-cables [homepage on the Internet]. [cited 2010 Jan 26]. Available from: <http://www.cryo-schippl.de/Transmag.pdf>
- [13] Lemmon EW, Jacobsen RT. Viscosity and Thermal Conductivity Equations for Nitrogen, Oxygen, Argon, and Air. International Journal of Thermophysics. 2004;25(1):21-69.
- [14] Potkay JA, Lambertus GR, Sacks RD, Wise KD. A Low-Power Pressure-and Temperature-Programmable Micro Gas Chromatography Column. J Microelectromech Syst. 2007;16(5):1071-1079.

6. CONCLUSIONS

This thesis consisted of an introduction, and four paper-based chapters, i.e., Experimental Setup, Permeability, Thermal Analysis, and Economic Analysis. The Experimental Setup chapter described the testing arrangements and loading scenarios, i.e., a benchtop configuration for long-term testing of single-wall fiber-reinforced composite tubes, and a mechanical loading scenario for dual-wall tubes, to measure minimum achievable annulus pressures and the corresponding leakage rates. In addition, the vacuum system and properties of the four, six, and eight layer specimens were also highlighted. In the Permeability chapter, leakage data for the single and dual-wall pipe was presented for the two testing scenarios, and equations for the intrinsic permeability coefficients were derived. In the Thermal Analysis chapter, a model was created to determine the thermal resistivity and heat flux for unit length (1 m) dual-wall specimens. The model parameters, i.e., annulus pressure, wall thickness, working fluid thermal properties, and the surrounding environmental air temperature, were made adjustable to facilitate various scenarios. The effect of modifying the model parameters was presented, as differences in the thermal resistance. In the Economics chapter, the heat flux data was used to calculate the heat pump work, which was added to the energy requirements of a continuously running mechanical vacuum pump, to determine the economic viability of three case studies, i.e., 60 °C oil, LN₂, and LNG. The data was presented, the results were analyzed, and the suitability of vacuum insulation to each application was

compared. The following conclusions were summarized for the test setup, and the viability of vacuum insulation for dual-wall FRPC pipes, utilizing low emissivity coatings.

6.1 Experimental Setup:

- The dual-wall flanged end-connection test setup enables measuring the minimum achievable annulus pressure, and air leakage rate, for FRPC specimens, under various loading scenarios.
- The single-wall benchtop arrangement enables the assessment of the minimum achievable holding pressure, and air leakage rate, for undamaged FRPC specimens
- Considering the time required for specimen manufacture, end connection assembly, depressurization and testing (either dual-wall or single-wall) each test requires approximately two weeks.
- The thermocouple and capacitance manometer gauges cooperatively measure annulus pressure over a range from 1.33×10^{-1} Pa (10^{-3} Torr) to 133.3 kPa (1000 Torr).
- A large variation in fiber volume fraction was found for the four layer specimens. An excess cover of resin remaining on the specimen surface is non-uniform, which causes the FVF measurements to be strongly affected for specimens with low fiber mass, i.e. the four layer specimens [1].

- The applied pressure rise rates of 12.23 kPa/s (1.77 psi/s) for the four layer dual-wall specimen, 10.53 kPa/s (1.53 psi/s) for the six layer specimen, and 7.02 kPa/s (1.02 psi/s) for the eight layer specimen were all within the range specified by [2], which allows for comparison with historical FRPC test data.

6.2 Permeability:

- Leakage mass flow rates were used to determine intrinsic permeability coefficients for single-wall tubes in the benchtop configuration. It was proven experimentally that FRPC tubular specimens are capable of holding a vacuum, but it decays slowly with time.
- The minimum achievable pressure for basalt/epoxy FRPC tubes is on the order of 1.33 Pa (10^{-2} Torr), which corresponds to a ‘medium’ vacuum level.
- Leakage mass flow rates for dual-wall FRPC specimens were used to determine intrinsic permeability coefficients under mechanical loading. The specimens exhibited significant leakage and pressure rise (vacuum decay) when axial tension loadings caused polymer matrix cracking, at transverse strains (to the fiber direction) above 0.3%.
- A slight drop in leakage flow rate was detected for subsequent increases in mechanical loading, below 0.3% transverse strain, for

each specimen tested. Further analysis is required to explain this phenomenon.

6.3 Thermal Analysis:

- An analytical model was created to determine the thermal resistance, and heat flux, for dual-wall FRPC pipes of unit length (1 m).
- Thermal resistance changes with annulus pressure and emissivity.
- Thermal resistance increases exponentially with decreasing emissivity.
- The thermal resistance for annulus pressures of 1.33×10^{-2} Pa (10^{-4} Torr) and 1.33×10^{-7} Pa (10^{-9} Torr) are effectively identical.
- An annulus pressure of 1.33×10^{-2} Pa (10^{-4} Torr), which is the lowest achievable pressure for a mechanical vacuum pump, corresponds to a high thermal resistance.
- The thermal resistance of four, six, and eight layer FRPC specimens are effectively identical.
- The thermal resistance for single and dual-wall emissivity coatings is effectively identical.

6.4 Economics Conclusions:

Note that in each of the compared examples, the working fluid flows through the center of the pipe, which is loaded with 4.5 kN (1000 lbs) of axial

tension, and the expressed savings component is compared to a urethane-insulated single-wall AISI-316 stainless steel pipe of the same ID as the FRPC pipe, for the six layer and industrial-sized examples.

- An optimum annulus pressure exists for maximizing the economic viability of vacuum insulated dual-wall FRPC pipe, by comparing YSOU values for a specific SPL.
- Further application of urethane foam insulation to an already vacuum-insulated dual-wall FRPC pipe has a greater effect for medium vacuum compared with high and ultra-high vacuum pressures.
- For oil flowing at 60 °C, a small-scale dual-wall FRPC pipe with medium vacuum pressure (1.33 Pa) and a layer of urethane foam insulation will not provide any significant savings (i.e., \$396 per SPL, while industrial-size pipe will save \$956).
- For LN₂, small-scale and industrial-size pipe require vacuum and urethane foam insulation to realize economic viability, although significant savings are not achieved, i.e., a small-scale dual-wall FRPC pipe with a low quality vacuum (13.3 kPa) will save \$246 per SPL, while industrial-size pipe will save \$317.
- For LNG, small-scale or industrial-size pipe is economically viable for medium quality vacuum insulation. A small-scale dual-wall FRPC pipe with medium quality vacuum insulation (1.33 Pa)

combined with urethane foam insulation will save \$14,500 per SPL while industrial-size pipe will save \$13,700.

- LNG with an annulus pressure of 1.33 Pa is the only application that achieves significant economic benefits over urethane foam insulated steel pipe, when using the current dual-wall vacuum-insulated basalt/epoxy design.

6.5 Contributions

The present study is not a validation of a specific FRPC dual-wall design for a particular application. Depending on the application, vacuum insulation technology may, or may not be economically viable. However, the designed end connections can be utilized with the experimental cart and methodology outlined in this thesis to determine the economic viability of various FRPC materials for insulated pipeline applications.

6.6 Suggested Future Work

The measured vacuum holding capability of basalt/epoxy FRPC specimens is encouraging, and further investigation into the feasibility of dual-wall pipes for insulation is prudent. Three possible avenues to increase the effectiveness of vacuum insulation are: (a) altering the FRPC materials, (b) utilizing high-density intrinsically-bonded coatings, and (c) development of a predictive numerical model, with the goal of decreasing the minimum achievable pressure beyond 1.33 Pa (10^{-2} Torr). An extensive numerical model that allows for leakage rate

predictions based on various parameters, i.e., pipe dimensions, material properties, fiber weave angle, FVF's, manufacturing and baking temperatures, initial crack densities, applied loads, and application boundary conditions would be useful in conjunction with experimental data. Furthermore, reference [3] found that thermally cycling carbon/polymer composites between LN₂ temperature (111 K) and 120 °C or 177 °C, and adding a hold period at the elevated temperature led to micro-crack initiation after fewer cycles and increased the micro-crack density of all samples tested. Thus, if a prospective pipeline is to be cycled between hot and cold temperatures, it is critical to utilize FRPC pipes with a high mode I fracture toughness [3], amongst other considerations.

6.7 References

- [1] Ruhl M, Mertiny P. Diffusion and leakage in vacuum-insulated dual-wall composite piping. Proc. International SAMPE Symposium; 2010; Seattle, WA.
- [2] Mertiny P, Gold A. Quantification of leakage damage in high-pressure fiber reinforced polymer composite tubular vessels. Polymer Testing. 2007;26:172-179.
- [3] Bechel VT, Camping JD, Kim RY. Cryogenic/elevated temperature cycling induced leakage paths in PMCs. Composites: Part B. 2005;36:171-182.

A. APPENDIX

A.1 Pressure Rise Data

The pressure rise data is included for the single-wall benchtop (BT) and dual-wall (DW) multi-axial testing scenarios.

A.1.1 Single-Wall Benchtop

The single-wall benchtop pressure rise data corresponds with the leakage data in section D.1.

A.1.1.1 Four-layer FRPC Specimen

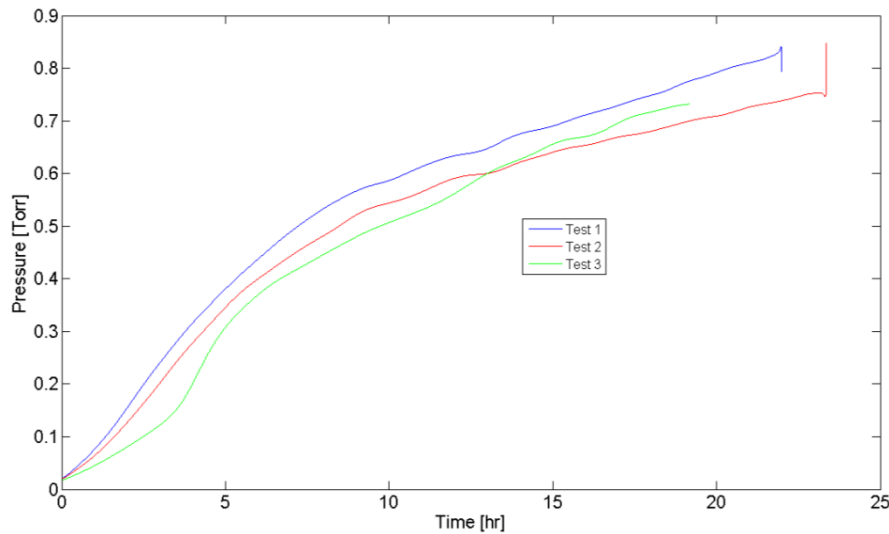


Figure A-1: Four-layer FRPC specimen BT pressure rise data

A.1.1.2 Six-layer FRPC Specimen

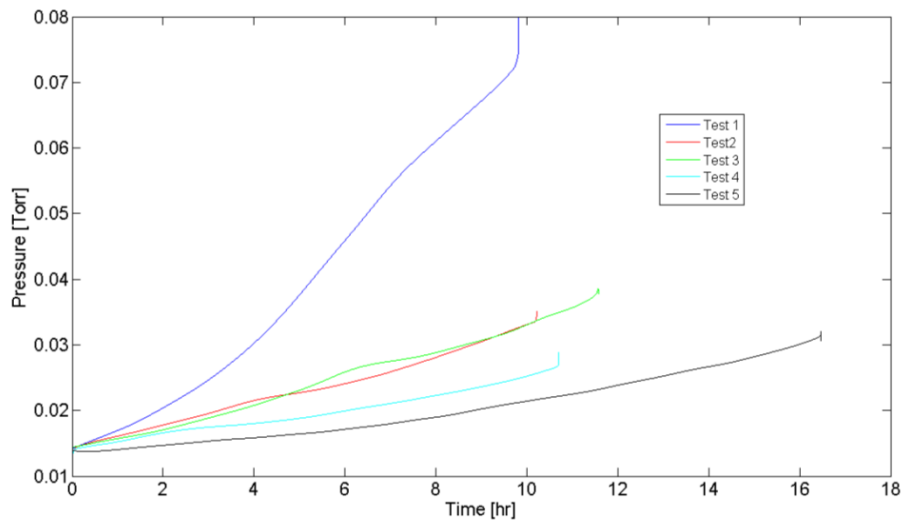


Figure A-2: Six-layer FRPC specimen BT pressure rise data

A.1.1.3 Eight-layer FRPC Specimen

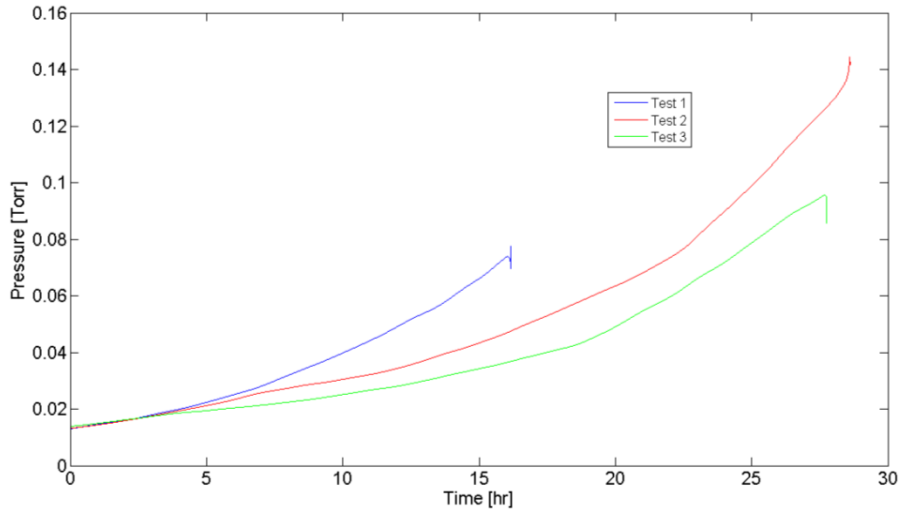


Figure A-3: Eight-layer FRPC specimen BT pressure rise data

A.1.2 Dual-Wall

The dual-wall pressure rise data corresponds with the leakage data in Section D.2.

A.1.2.1 Four-layer FRPC Specimen Without the 3000 Pound Scenario

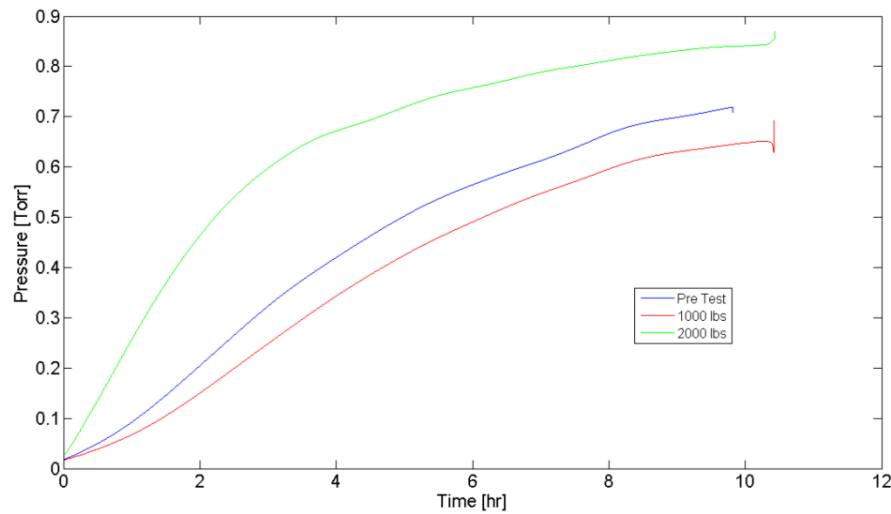


Figure A-4: Four-layer FRPC specimen DW pressure rise data

A.1.2.2 Four-layer FRPC Specimen With the 3000 Pound Scenario

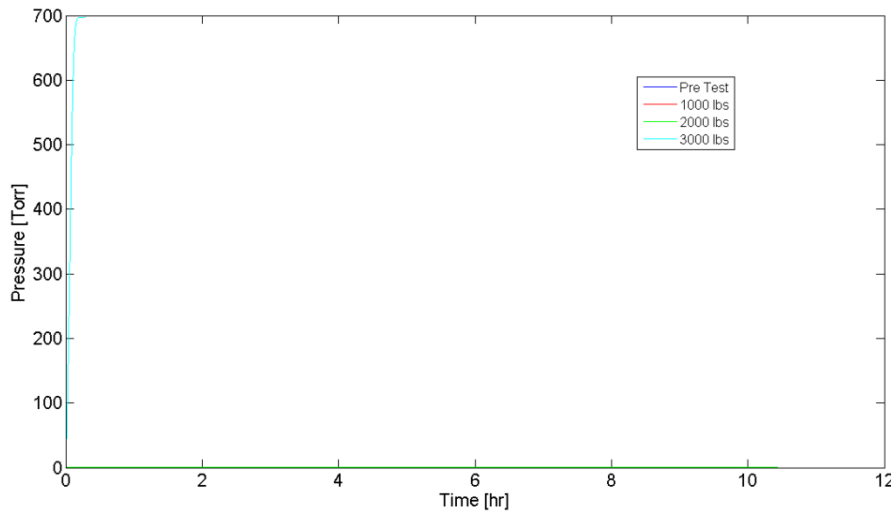


Figure A-5: Four-layer FRPC specimen DW pressure rise data

A.1.2.3 Six-layer FRPC Specimen Without the 3000 Pound Scenario

Scenario

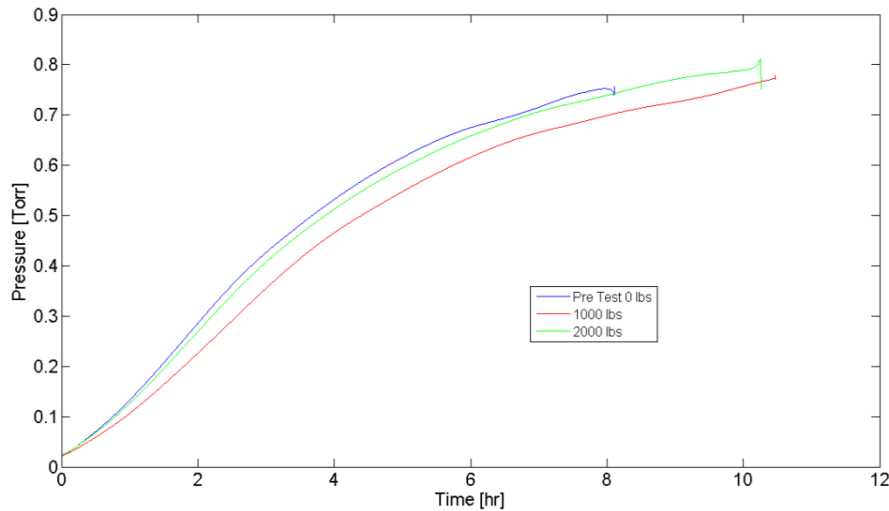


Figure A-6: Six-layer FRPC specimen DW pressure rise data

A.1.2.4 Six-layer FRPC Specimen With the 3000 Pound Scenario

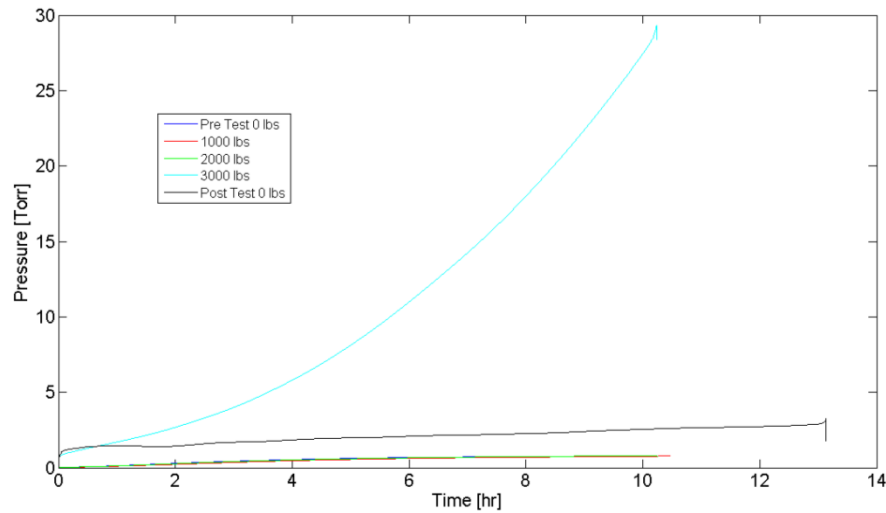


Figure A-7: Six-layer FRPC specimen DW pressure rise data

A.1.2.5 Eight-layer FRPC Specimen

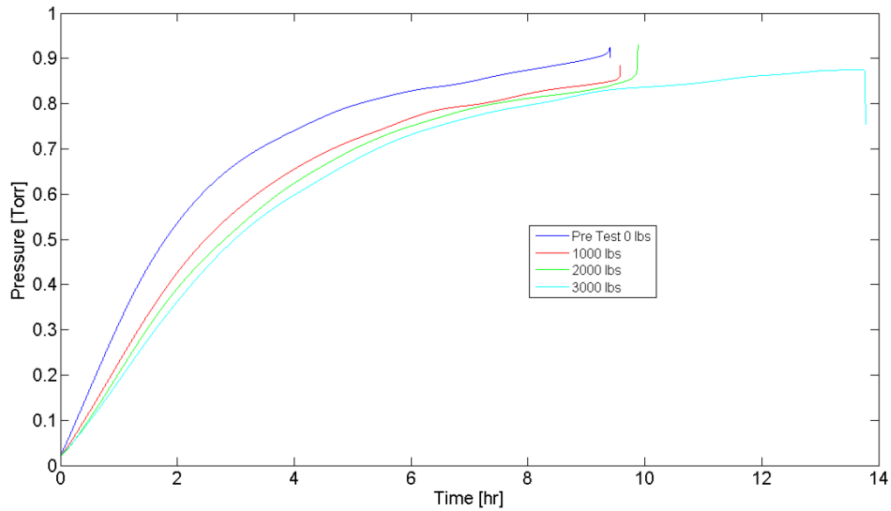


Figure A-8: Eight-layer FRPC specimen DW pressure rise data

A.1.3 Dual-Wall Puncture Test

After successfully acquiring the leakage rate data for a tensile load of 13.345 kN (3000 lbs), the dual-wall specimen was unloaded and depressurized. As the pressure rise data was being recorded, a rotary saw was used to puncture a hole in the outer pipe of the dual-wall specimens. Note that the puncture test was not performed for the four-layer dual-wall specimen, as it failed during the 13.345 kN loading scenario.

A.1.3.1 Six-layer Puncture Test

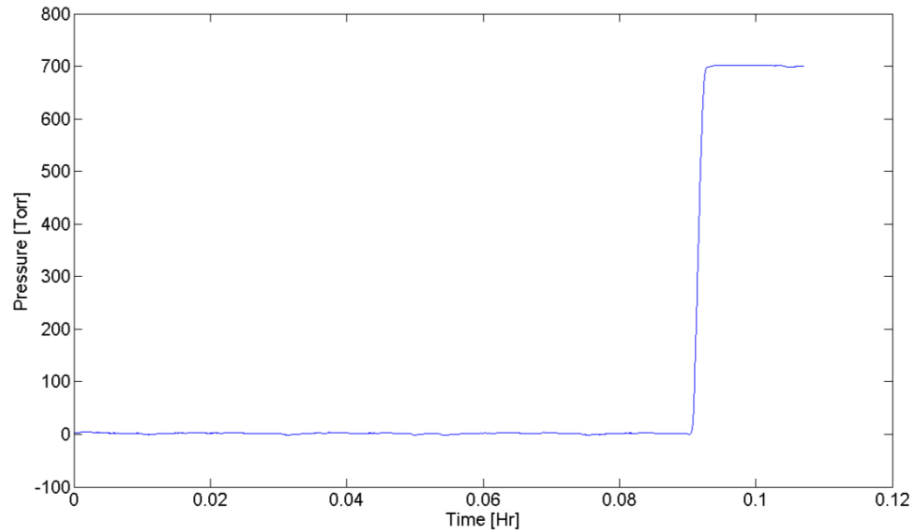


Figure A-9: Six-layer DW FRPC puncture test data

A.1.3.2 Eight-layer Puncture Test

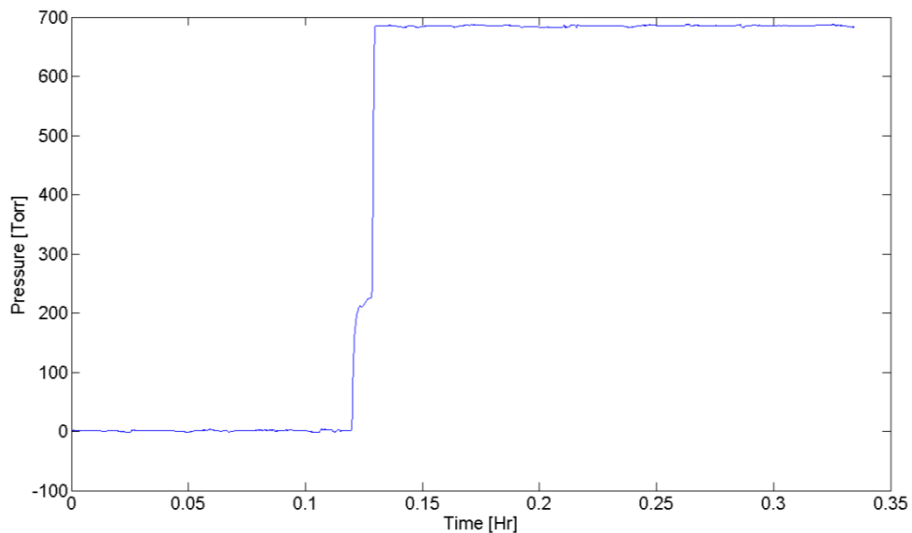


Figure A-10: Eight-layer DW FRPC puncture test data

B. PRESSURE AND TIME PARAMETER

DATA TABLES

For the following data tables, the initial pressure, P_o , and end pressure, P_f , are shown for each test scenario. Note that BT represents benchtop and DW the dual-wall configuration.

B.1 Benchtop

Note that the star on the first set of data for Table B-2 indicates the data is an outlier, as the calculated mass flow rate, diffusion, and intrinsic permeability are greater than one standard deviation (including all five test points) away from the nearest included point.

Table B-1: BT pressure and time parameters for the four-layer specimen

Test	Pump Time [Hr]	Test Time [Hr]	$P_o [10^{-2} \text{ Torr}]$	$P_f [\text{Torr}]$
1	63.5	22.0	1.94	0.8
2	23.5	23.3	1.79	0.72
3	8.5	19.5	1.38	0.72
Average	31.8	21.6	1.70	0.75

Table B-2: BT pressure and time parameters for the six-layer specimen

Test	Pump Time [Hr]	Test Time [Hr]	$P_o [10^{-2} \text{ Torr}]$	$P_f [10^{-2} \text{ Torr}]$
1*	65.2	9.8	1.31	7.00
2	42.2	10.2	1.21	3.25
3	10.4	11.6	1.4	3.75
4	16.2	10.7	1.18	2.60
5	17.1	16.5	1.38	3.10
Average	30.2	11.8	1.30	3.94

Table B-3: BT pressure and time parameters for the eight-layer specimen

Test	Pump Time [Hr]	Test Time [Hr]	P_o [10^{-2} Torr]	P_f [10^{-2} Torr]
1	42.8	16.2	1.31	7.20
2	32.0	28.6	1.29	14.0
3	23.4	27.8	1.37	9.50
Average	32.7	24.2	1.32	10.2

B.2 Dual-Wall

Table B-4: DW pressure and time parameters for the four-layer specimen

Load [lbs]	Pump Time [Hr]	Test Time [Hr]	P_o [10^{-2} Torr]	P_f [Torr]
0	46.0	9.8	1.60	0.72
1000	13.2	10.4	1.38	0.64
2000	13.0	10.4	2.22	0.83
3000	13.2	0.3	6.60	697.83

Table B-5: DW pressure and time parameters for the six-layer specimen

Load [lbs]	Pump Time [Hr]	Test Time [Hr]	P_o [10^{-2} Torr]	P_f [Torr]
0	41.2	8.1	1.91	0.75
1000	12.2	10.5	1.68	0.77
2000	13.4	10.3	2.14	0.8
3000	13.2	10.2	2.41	29

Table B-6: DW pressure and time parameters for the eight-layer specimen

Load [lbs]	Pump Time [Hr]	Test Time [Hr]	P_o [10^{-2} Torr]	P_f [Torr]
0	41.4	9.4	2.19	2.1
1000	13.9	9.6	2.12	1.7
2000	14.1	9.9	1.87	1.7
3000	12.9	13.8	1.80	1.9

C. THERMODYNAMIC ANALYSIS DATA

C.1 Thermal Resistance versus Effective Emissivity

C.1.1 Four-layer Pipe Thermal Resistance Versus Effective Emissivity

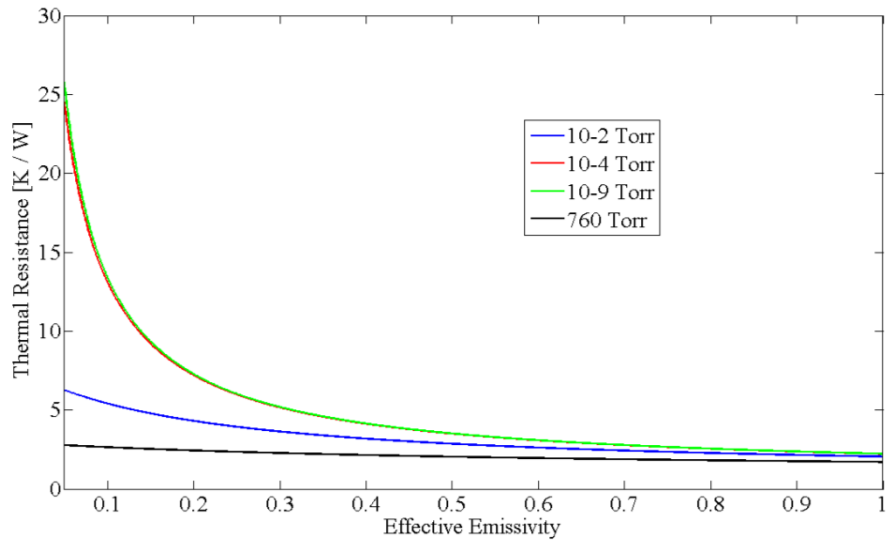


Figure C-1: Four-layer FRPC thermal resistance versus effective emissivity

C.1.2 Eight-layer Pipes Thermal Resistance Versus Effective Emissivity

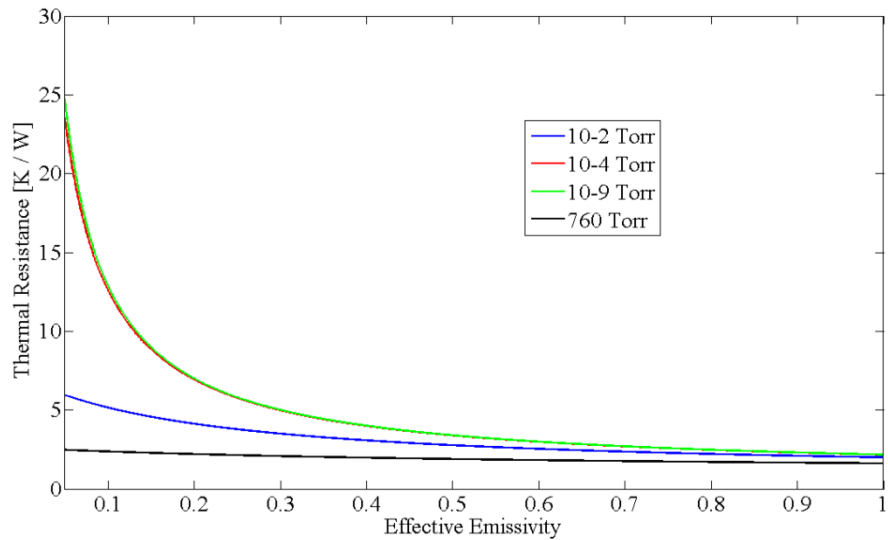


Figure C-2: Eight-layer FRPC thermal resistance versus effective emissivity

C.1.3 10^{-4} Torr Annulus Pressure Thermal Resistance Versus Effective Emissivity

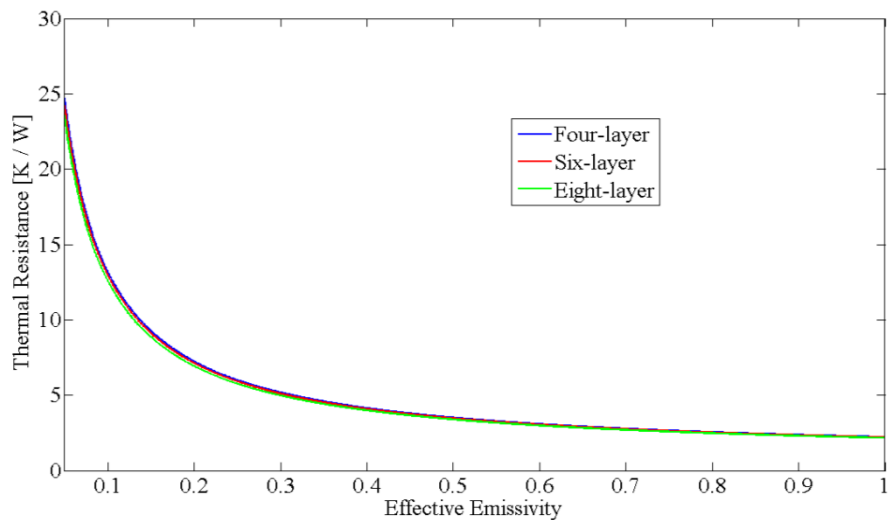


Figure C-3: Thermal resistance versus effective emissivity for a 10^{-4} Torr

C.1.4 10^{-9} Torr Annulus Pressure Thermal Resistance Versus Effective Emissivity

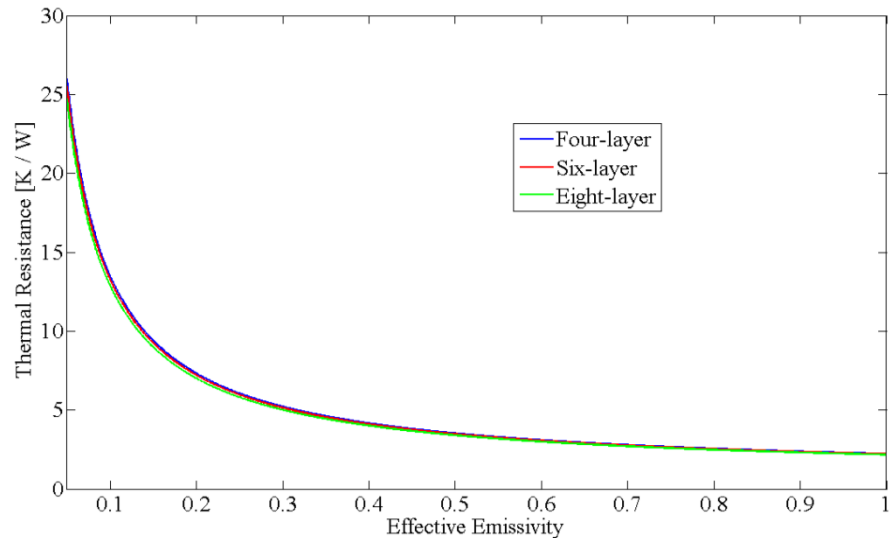


Figure C-4: Thermal resistance versus effective emissivity for a 10^{-9} Torr

C.1.5 760 Torr Annulus Pressure Thermal Resistance Versus Effective Emissivity

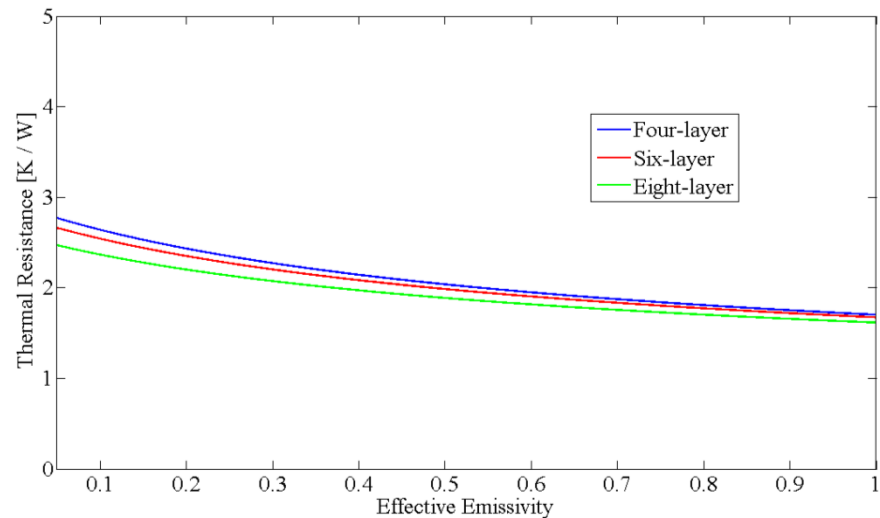


Figure C-5: Thermal resistance versus effective emissivity for a 760 Torr

C.2 Low Emissivity Coatings on One or Both Surfaces

This section was examining the benefit of coating both of the annular bounding surfaces instead of only one, for the dual-wall pipes.

C.2.1 Comparison of Dual or Single-Wall Effective Emissivity Coatings for Four-Layer Pipes

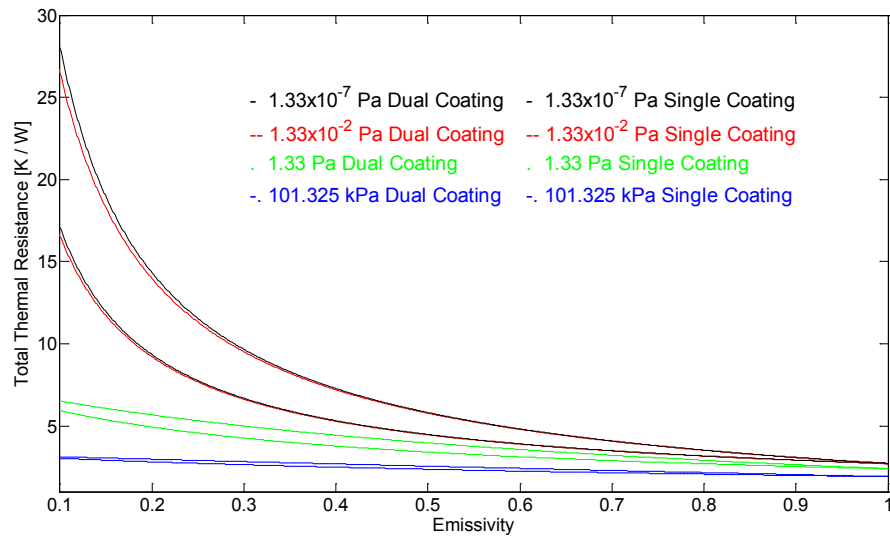


Figure C-6: Four-layer DW FRPC thermal resistance versus emissivity

C.2.2 Comparison of Dual or Single-Wall Effective Emissivity Coatings for Eight-Layer Pipes

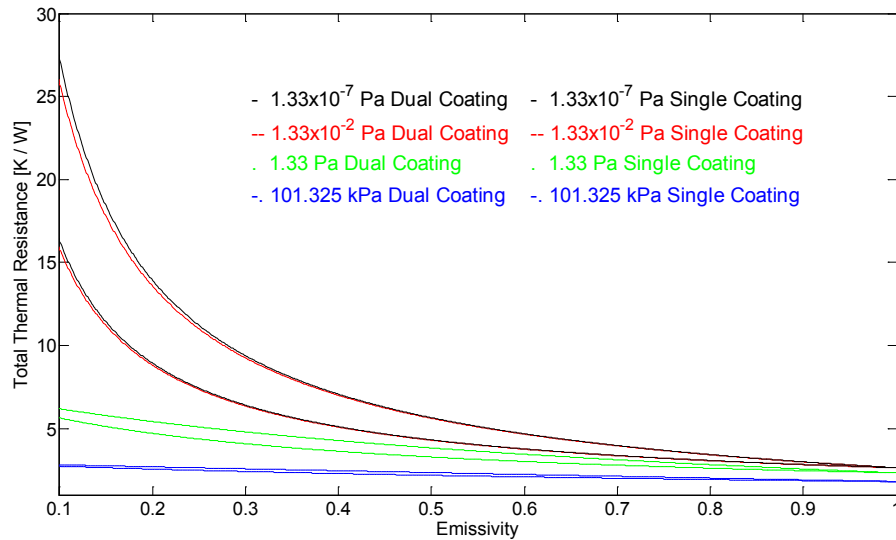


Figure C-7: Eight-layer DW FRPC thermal resistance versus emissivity

D. AIR FLOW CHARACTERISTICS

Table D-1: Air Flow Characteristics for LNG at 111 K

Annulus Pressure [Pa]	\dot{m}_{pump} [kg/s]	Small Pipe S [mbar×mm]		Large Pipe S [mbar×mm]	
Label				Label	
101,325	5.876×10^{-3}	4,710	Cont	56,517	Cont
13,332	7.863×10^{-4}	619.7	Cont	7,437	Cont
1,333	7.863×10^{-5}	61.97	Cont	743.7	Cont
133	7.863×10^{-6}	6. 197	Tstl	74.37	Cont
13.3	7.863×10^{-7}	$6. 197 \times 10^{-1}$	Tstl	7.437	Cont
1.33	7.863×10^{-8}	$6. 197 \times 10^{-2}$	Tstl	7.437×10^{-1}	Tstl
1.33×10^{-1}	7.863×10^{-9}	$6. 197 \times 10^{-3}$	Mlcr	7.437×10^{-2}	Tstl
1.33×10^{-2}	7.863×10^{-10}	$6. 197 \times 10^{-4}$	Mlcr	7.437×10^{-3}	Mlcr
1.33×10^{-7}	7.863×10^{-15}	6.197×10^{-9}	Mlcr	7.437×10^{-8}	Mlcr

Table D-2: Air Flow Characteristics for LN₂ at 72 K

Annulus Pressure [Pa]	\dot{m}_{pump} [kg/s]	Small Pipe S [mbar×mm]		Large Pipe S [mbar×mm]	
Label				Label	
101,325	6.678×10^{-3}	4,710	Cont	56,517	Cont
13,332	8.786×10^{-4}	619.7	Cont	7,437	Cont
1,333	8.786×10^{-5}	61.97	Cont	743.7	Cont
133	8.786×10^{-6}	6. 197	Tstl	74.37	Cont
13.3	8.786×10^{-7}	$6. 197 \times 10^{-1}$	Tstl	7.437	Cont
1.33	8.786×10^{-8}	$6. 197 \times 10^{-2}$	Tstl	7.437×10^{-1}	Tstl
1.33×10^{-1}	8.786×10^{-9}	$6. 197 \times 10^{-3}$	Mlcr	7.437×10^{-2}	Tstl
1.33×10^{-2}	8.786×10^{-10}	$6. 197 \times 10^{-4}$	Mlcr	7.437×10^{-3}	Mlcr
1.33×10^{-7}	8.786×10^{-15}	6.197×10^{-9}	Mlcr	7.437×10^{-8}	Mlcr

E. FILTERING 95% CONFIDENCE INTERVAL COEFFICIENTS

These data tables include the coefficients for the linear approximation of the pressure versus time data, shown in section B.1, along with their 95% confidence intervals.

E.1 Benchtop Configuration

Table E-1: Four-layer 95% confidence interval fitting coefficients

Test	A [Torr/hr]	B [Torr]	A ₉₅₊ [Torr/hr]	B ₉₅₊ [Torr]	A ₉₅₋ [Torr/hr]	B ₉₅₋ [Torr]	R ²
1	0.03335	0.1798	0.03337	0.1801	0.03333	0.1795	0.91
2	0.02907	0.1722	0.02909	0.1725	0.02905	0.1719	0.89
3	0.03858	0.07334	0.0386	0.07358	0.03856	0.0731	0.95

Table E-2: Six-layer 95% confidence interval fitting coefficients

Test	A [Torr/hr]	B [Torr]	A ₉₅₊ [Torr/hr]	B ₉₅₊ [Torr]	A ₉₅₋ [Torr/hr]	B ₉₅₋ [Torr]	R ²
1	0.006441	0.00793	0.006444	0.007946	0.006438	0.007915	0.98
2	0.001786	0.01407	0.001787	0.01407	0.001785	0.01406	0.99
3	0.001985	0.01333	0.001986	0.01334	0.001985	0.01333	0.99
4	0.001067	0.01398	0.001068	0.01398	0.001067	0.01398	0.98
5	0.00103	0.01183	0.001031	0.01184	0.00103	0.01183	0.97

Table E-3: Eight-layer 95% confidence interval fitting coefficients

Test	A [Torr/hr]	B [Torr]	A ₉₅₊ [Torr/hr]	B ₉₅₊ [Torr]	A ₉₅₋ [Torr/hr]	B ₉₅₋ [Torr]	R ²
1	0.003696	0.005905	0.003698	0.00592	0.003694	0.005888	0.96
2	0.003776	-0.00239	0.003779	-0.00235	0.003774	-0.00243	0.90
3	0.002673	0.002505	0.002675	0.00254	0.002671	0.002474	0.88

Table E-4: System calibration 95% confidence interval fitting coefficients

Test	A [Torr/hr]	B [Torr]	A_{95+} [Torr/hr]	B_{95+} [Torr]	A_{95-} [Torr/hr]	B_{95-} [Torr]	R^2
1	0.01033	0.07045	0.01034	0.07051	0.01033	0.07039	0.94
2	0.001021	0.01592	0.001022	0.01593	0.001021	0.01592	0.96
3	0.000598	0.0145	0.000598	0.0145	0.000598	0.0145	0.94
4	0.000334	0.01319	0.000334	0.01319	0.000334	0.01318	0.86
5	0.000104	0.01389	0.000105	0.01389	0.000104	0.01389	0.70

E.2 Dual-Wall Configuration

Table E-5: Four-layer 95% confidence interval fitting coefficients

Load [lbs]	A [Torr/hr]	B [Torr]	A_{95+} [Torr/hr]	B_{95+} [Torr]	A_{95-} [Torr/hr]	B_{95-} [Torr]	R^2
0	0.07558	0.0692	0.03337	0.06948	0.07553	0.06891	0.962
1000	0.06786	0.03992	0.0679	0.04016	0.06782	0.03969	0.9686
2000	0.065	0.304	0.0651	0.3046	0.0649	0.3034	0.8066
3000	2430	190.5	2457	194.9	2403	186.1	0.7521

Table E-6: Six-layer 95% confidence interval fitting coefficients

Load [lbs]	A [Torr/hr]	B [Torr]	A_{95+} [Torr/hr]	B_{95+} [Torr]	A_{95-} [Torr/hr]	B_{95-} [Torr]	R^2
0	0.09472	0.09121	0.0948	0.09158	0.09464	0.09084	0.9508
1000	0.07401	0.1048	0.07395	0.1044	0.07408	0.1052	0.9358
2000	0.07679	0.1323	0.07686	0.1327	0.07672	0.1319	0.9243
3000	2.657	-3.019	2.659	-3.006	2.655	-3.031	0.9435

Table E-7: Eight-layer 95% confidence interval fitting coefficients

Load [lbs]	A [Torr/hr]	B [Torr]	A_{95+} [Torr/hr]	B_{95+} [Torr]	A_{95-} [Torr/hr]	B_{95-} [Torr]	R^2
0	0.07514	0.3324	0.07526	0.333	0.07501	0.3317	0.8023
1000	0.07764	0.2453	0.07774	0.2459	0.07753	0.2447	0.8582
2000	0.07754	0.2205	0.07764	0.2211	0.07744	0.22	0.8769
3000	0.05314	0.2961	0.05321	0.2966	0.05307	0.2955	0.8124

Table E-8: System calibration 95% confidence interval fitting coefficients

Test	A [Torr/hr]	B [Torr]	A_{95+} [Torr/hr]	B_{95+} [Torr]	A_{95-} [Torr/hr]	B_{95-} [Torr]	R^2
1	0.000990	0.02025	0.000990	0.02026	0.000989	0.02024	0.965
2	0.000612	0.01303	0.000612	0.01303	0.000612	0.01302	0.979
3	0.000481	0.01216	0.000481	0.01217	0.000480	0.01216	0.8422

F.DUMMY CLAMP DRAWINGS

REVISION HISTORY

REV	DESCRIPTION	BY	DATE	APPR
0	Prototype Release	MR	24-Feb-09	

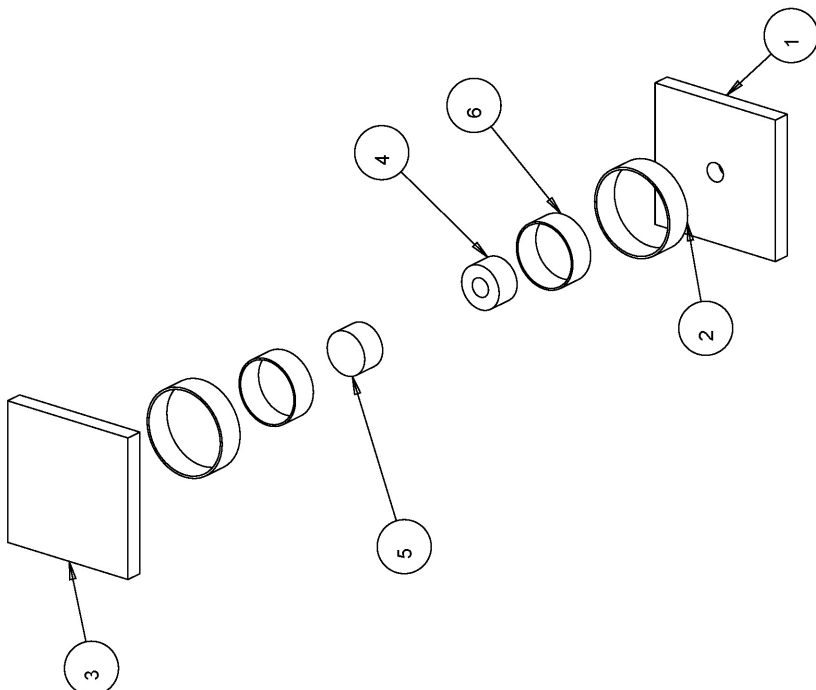
SECTION A-A

TYPE	ALSO PROPOSED	INFORMATION CONTAINED IN THIS DRAWING IS THE SOLE PROPERTY OF THE DEPARTMENT OF MECHANICAL ENGINEERING, UNIVERSITY OF ALBERTA, AND IS HEREBY EXPRESSEDLY UNDERSTOOD TO BE PROPRIETARY INFORMATION OF THE DEPARTMENT OF MECHANICAL ENGINEERING, UNIVERSITY OF ALBERTA. IT IS NOT TO BE COPIED OR DISCLOSED EXCEPT AS AUTHORIZED BY THE DEPARTMENT OF MECHANICAL ENGINEERING, UNIVERSITY OF ALBERTA.	DEPARTMENT OF MECHANICAL ENGINEERING UNIVERSITY OF ALBERTA	TITLE
TOOLING SPECIFICATIONS				
TOOLING SURFACES				
UNSPECIFIED SURFACES				
MATERIAL				
INTEGRIC				
METRIC				

REVISION HISTORY		1			
REV	DESCRIPTION	BY	DATE	APPR	
0	Prototypes Release	MR	24-Feb-00		

INDEX		DESCRIPTION	VENDOR	VENDOR PART NO.	QTY
6	1.5 HOLDER	MERP_005_002	-	-	2
5	ROUND NO-HOLE	MERP_005_003	-	-	1
4	ROUND	MERP_005_005	-	-	1
3	PLATE NO-HOLE	MERP_005_004	-	-	1
2	2.0 HOLDER	MERP_005_003	-	-	2
1	PLATE	MERP_005_001	-	-	1

B	Third Angle Projection		DEPARTMENT OF MECHANICAL ENGINEERING UNIVERSITY OF ALBERTA		A				
The information contained in this drawing is the sole property of the University of Alberta. Reproduction in part or whole without the written permission of the Department of Mechanical Engineering, University of Alberta is prohibited.									
SHEET 2 OF 2									
TOOLTIPS	UNITS: INCHES	DRAWN BY	TITLE	DRAWN BY	TITLE				
TOLERANCES	SURFACE FINISH	MR	DATE	MR	DATE				
Unless otherwise specified	Unfurnished	CUST APPR	DRAWN BY	CUST APPR	DRAWN BY				
NOTES	Angular = $\pm 0.5^\circ$	Material = Machined	24-Feb-00	MERP_005_005	MERP_005_005				
INCHES	0.000 ± 0.005	$R = 0.32$ $\sqrt{0.005} = 0.01$	EWS APPR	FILE NAME: MERP_005_005	FILE NAME: MERP_005_005				
METRIC	5.00 ± 0.05	± 0.05 ± 0.01	Mfg APPR	SIZE: 240x300	SIZE: 240x300				
			Relief/Cut/Forged	SCALE: 1:100	SCALE: 1:100				
			2	1	1				
			3						
			4						
			5						
			6						



Front View

Front View dimensions:

- Total width: 4.00
- Slot width: 2.00
- Slot depth: 5.0
- Base thickness: 2.00

Top View

Top View dimensions:

- Side length: 4.00
- Hole diameter: Ø .54 (1/4" NPT)

Side View

Side View dimensions:

- Height: 4.00
- Slot depth: 5.0

MATERIAL: Steel

CONDITION: -

FINISH: -

REV: 0

DESCRIPTION: Prototype Release

BY: MR

DATE: 24-Feb-09

AFPR: 0

REVISION HISTORY

1	
2	
3	
4	
5	
6	

**DEPARTMENT OF MECHANICAL ENGINEERING
UNIVERSITY OF ALBERTA**

Plate

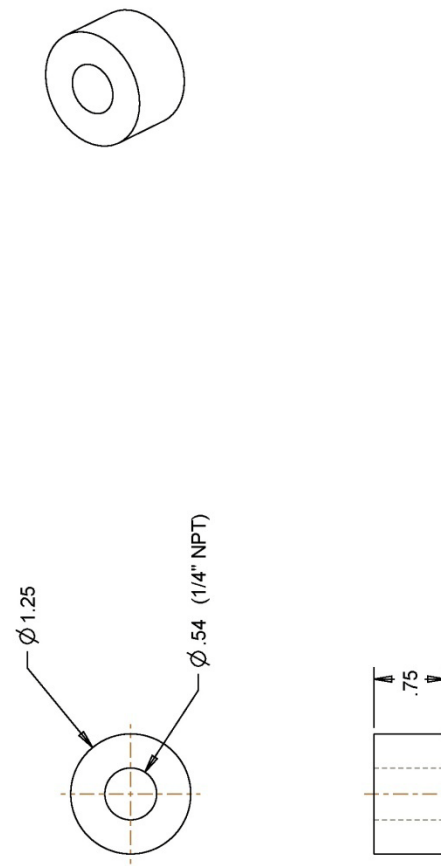
Third Year Project	The information contained in this drawing is the sole property of THE DEPARTMENT OF MECHANICAL ENGINEERING, UNIVERSITY OF ALBERTA, AND IS EXCLUSIVELY FOR INTERNAL USE ONLY. IT IS THE PROPERTY OF THE UNIVERSITY OF ALBERTA, AND IS NOT TO BE COPIED OR REPRODUCED.	24-Feb-09	MR	MR	MRP_005_001	0
TOLERANCES	Un-specified	0.015	0.012	0.010	0.008	0.005
UNITS	Specified	Inches	Millimetres	Millimetres	Millimetres	Millimetres
GENERAL	Drawn by	U.S./AFPR	U.S./AFPR	U.S./AFPR	U.S./AFPR	U.S./AFPR
	Date	Date	Date	Date	Date	Date
	FILE NAME	FILE NAME	FILE NAME	FILE NAME	FILE NAME	FILE NAME
	SIZE	SIZE	SIZE	SIZE	SIZE	SIZE
	SCALE	SCALE	SCALE	SCALE	SCALE	SCALE
	UNITS	UNITS	UNITS	UNITS	UNITS	UNITS
	1	1	1	1	1	1

		6		5		4		3		2		1			
		MATERIAL	CONDITION	FINISH								REVISION HISTORY			
		DONI Steel	-									REV	DESCRIPTION	BY	DATE
												0	Prototype Release	MR	24-Feb-00
2" Drawn Over Mandrel Steel Tubing		2.500" OD	2.370" ID			0.065" Wall		Available from Metal Supermarkets							
D															
C															
B															
A															

6		5		4		3		2		1	
MATERIAL	CONDITION	FINISH	-	-	-	-	-	-	-	-	-
1018/1020	-	-	-	-	-	-	-	-	-	-	-

D	C	B	A

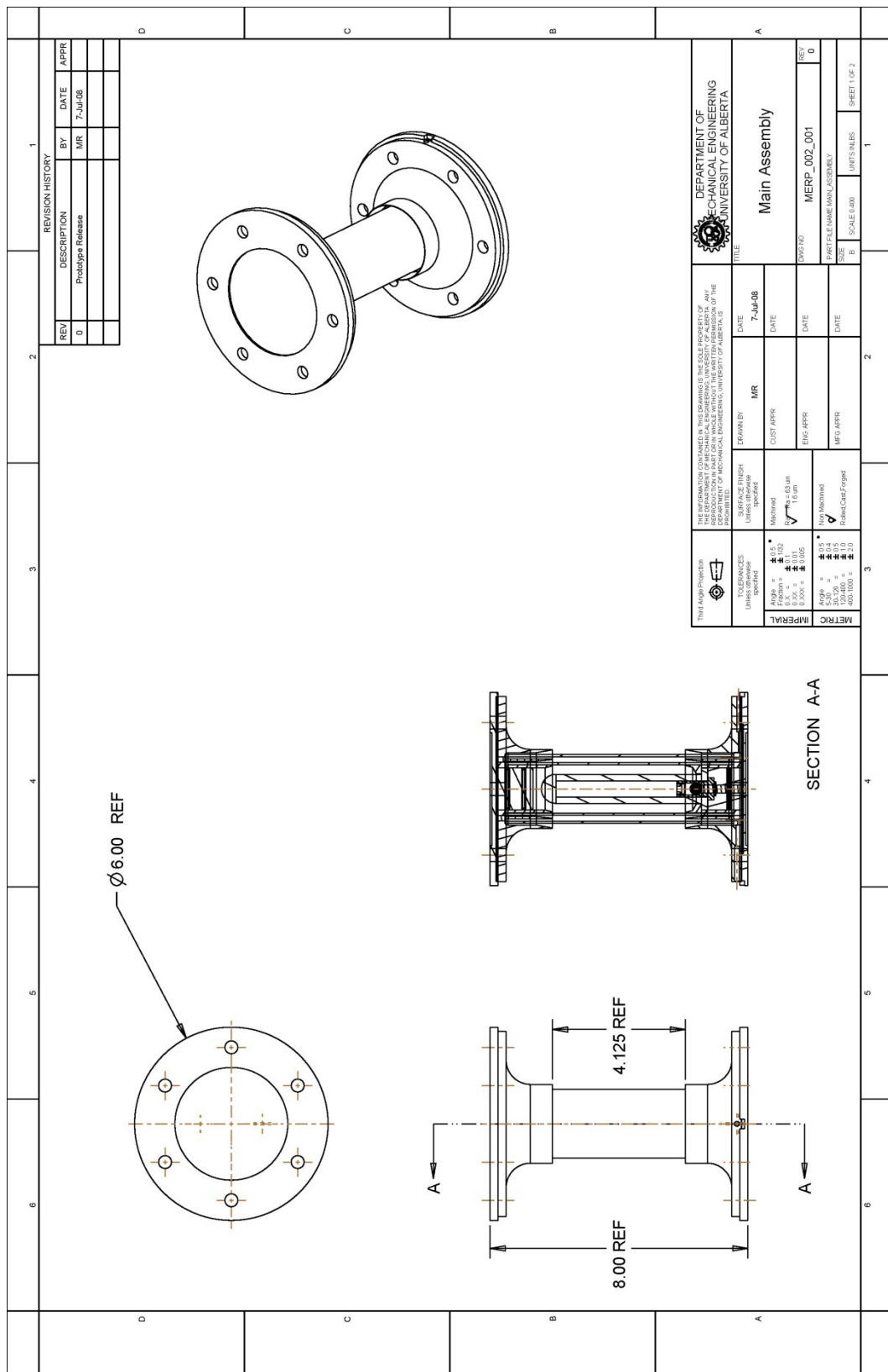
Third Angle Projection

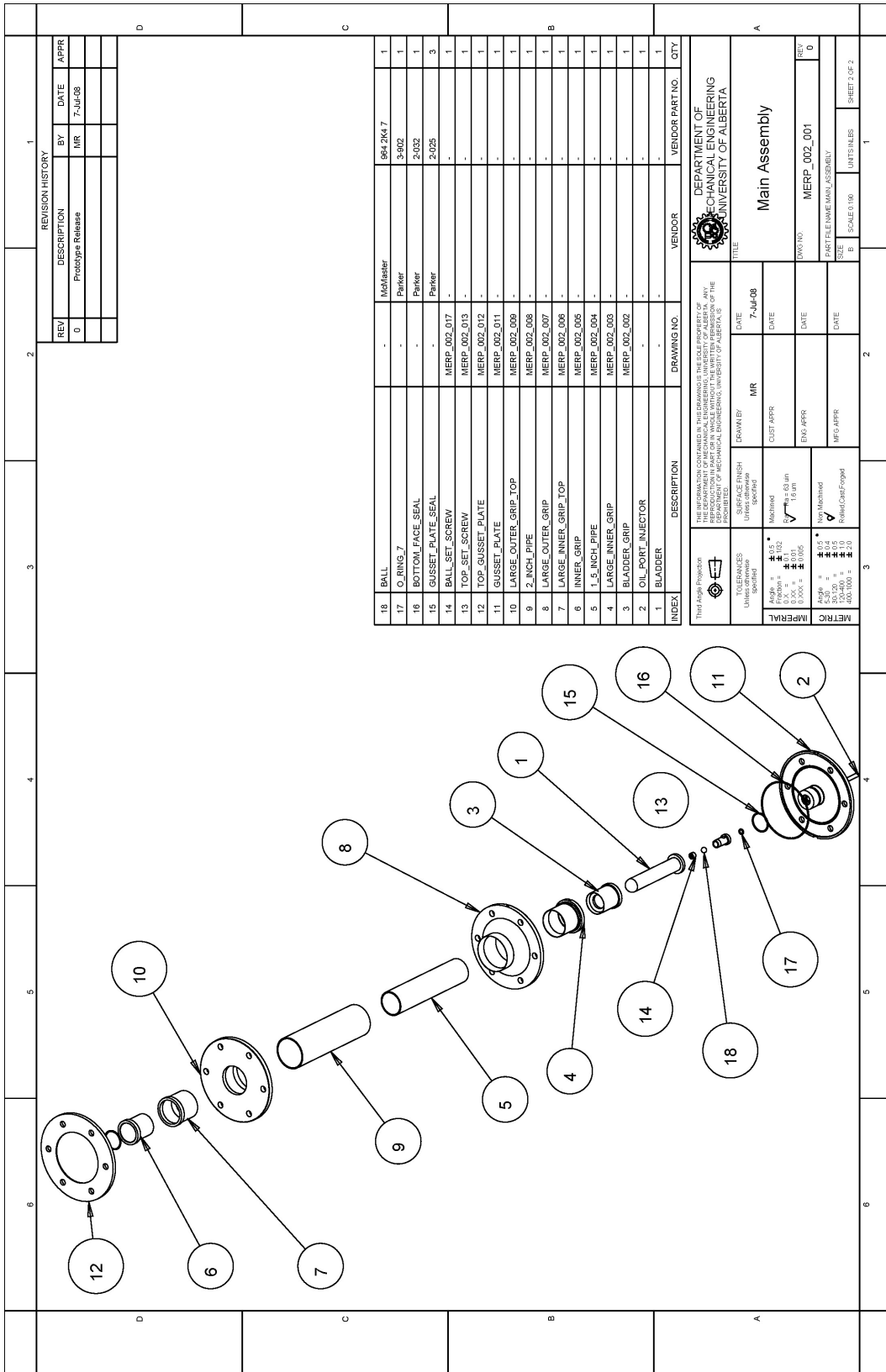


1.25" Steel Round

DEPARTMENT OF MECHANICAL ENGINEERING UNIVERSITY OF ALBERTA		TITLE	
DRAWN BY	MR	DATE	24-Feb-09
SUPERVISOR	CUST APPR	DATE	
Unlabeled spec'd	Machined	EHS APPROV	
Angle = $\pm 0.5^\circ$ Tolerance = 0.000 ± 0.005	R = 6.35 mm $\sqrt{16} = 4$ mm	Mr. G. APPR	
INCHES		MM	
Angle = $\pm 0.5^\circ$ Tolerance = 0.000 ± 0.005	No Machined	MRP_005_006	0
METRIC		INCHES	
Angle = $\pm 0.5^\circ$ Tolerance = 1.00 ± 0.10	Relief/Cant Forged	SIZE	SCALE 1:100
50.000 ± 0.000	Ø 20	2	UNITS IN MM
46.000 ± 0.000		3	SHEET 1 OF 1
40.000 ± 0.000		4	1
35.000 ± 0.000		5	
30.000 ± 0.000		6	

**G. DUAL-WALL FLANGED END
CONNECTION DRAWINGS**





Large Inner Grip

Detail A

Section A-A

Section B-B

Detail A
SCALE 3.000

Revision History

REV	DESCRIPTION	BY	DATE	APPR
0	Prototype Release	MR	20-Jun-08	

**Department of Mechanical Engineering
University of Alberta**

Large Inner Grip

Detail A

Section A-A

Section B-B

Detail A
SCALE 3.000

Revision History

REV	DESCRIPTION	BY	DATE	APPR
0	Prototype Release	MR	20-Jun-08	

Large Inner Grip

Detail A

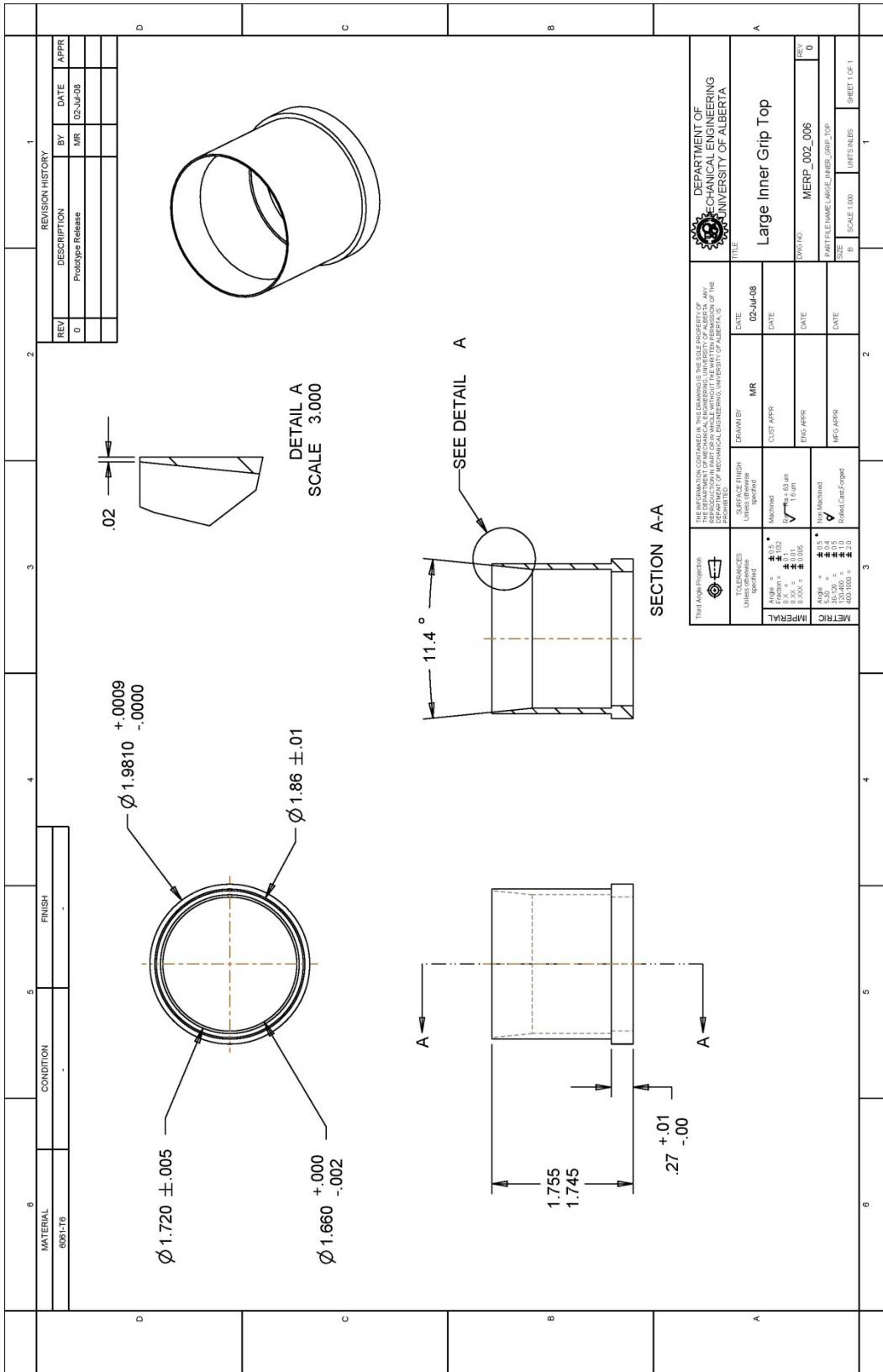
Section A-A

Section B-B

Detail A
SCALE 3.000

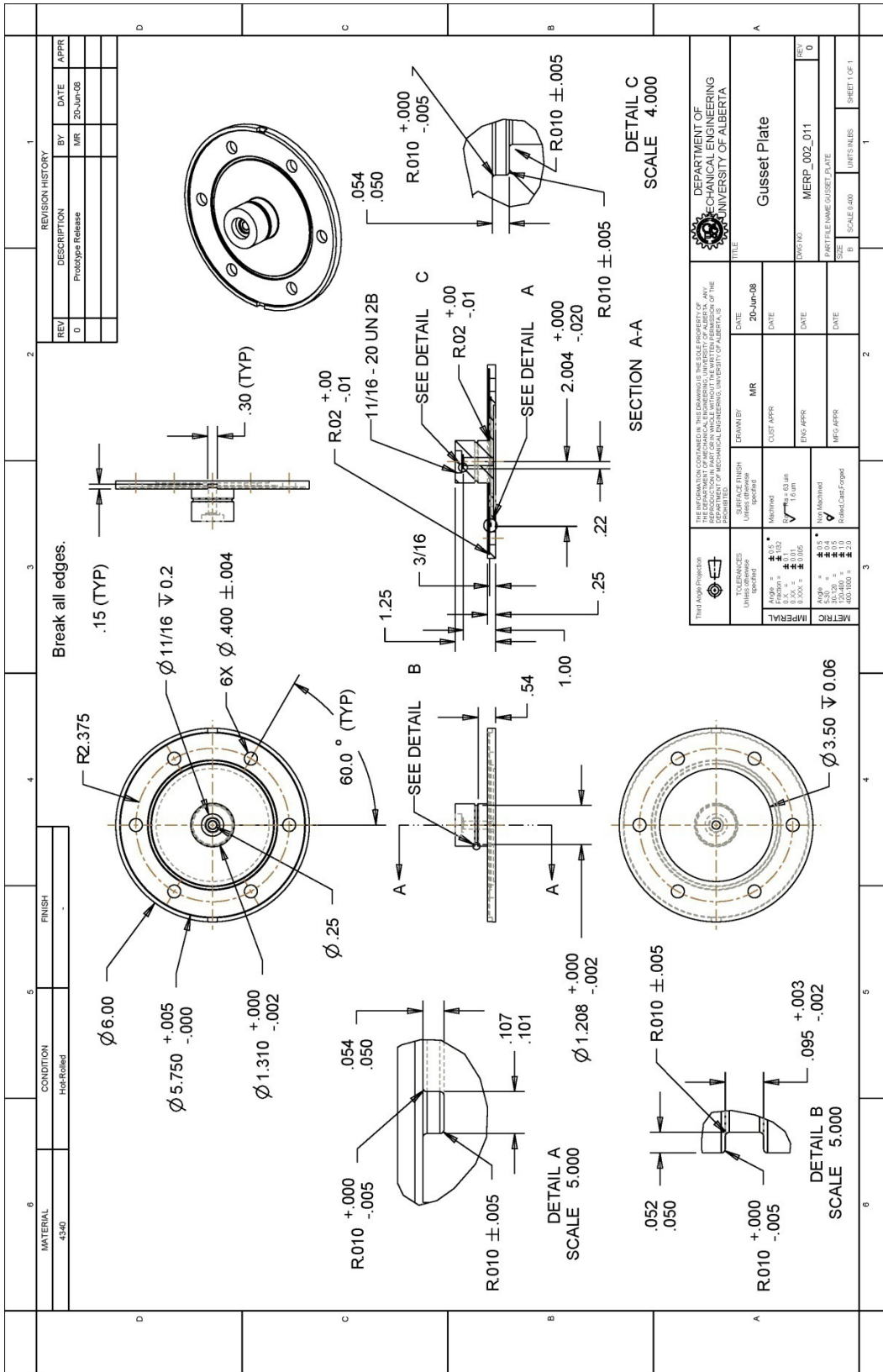
Revision History

REV	DESCRIPTION	BY	DATE	APPR
0	Prototype Release	MR	20-Jun-08	

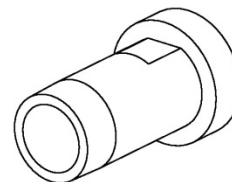
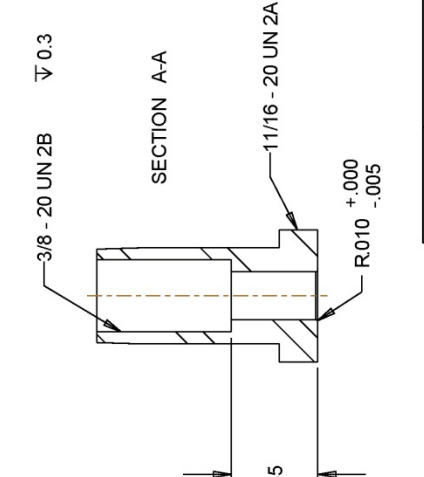
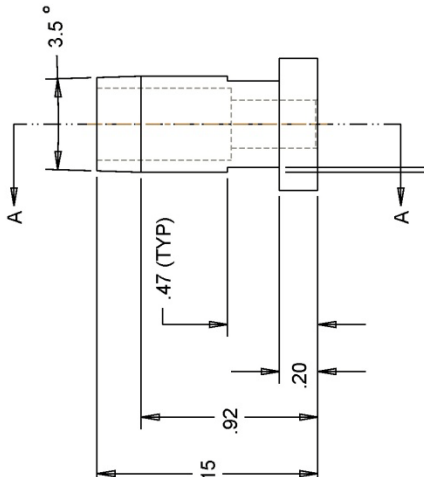
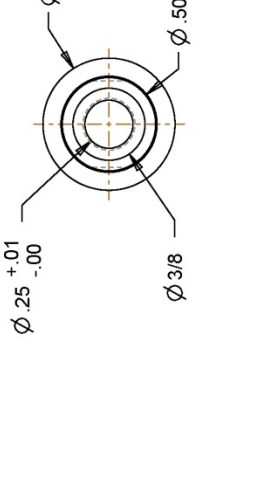
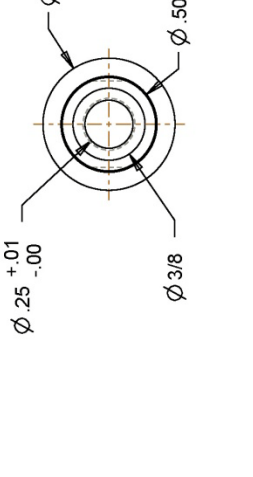
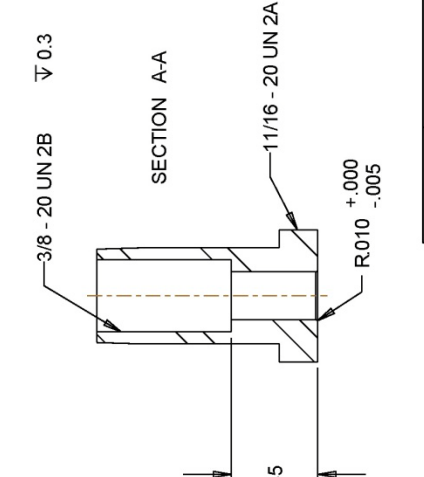
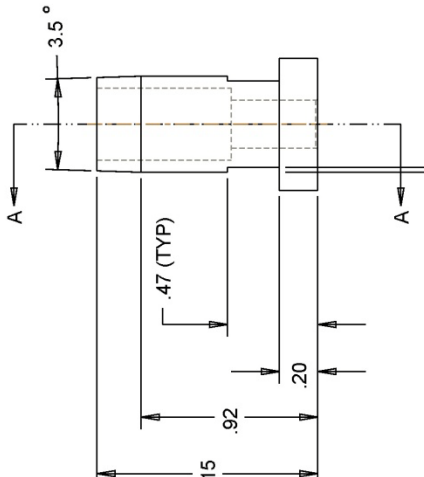
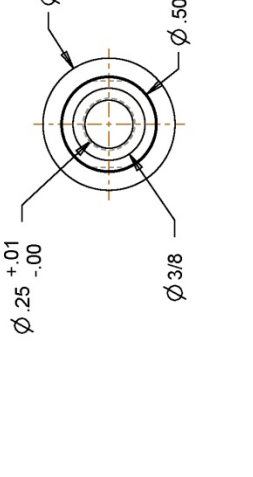
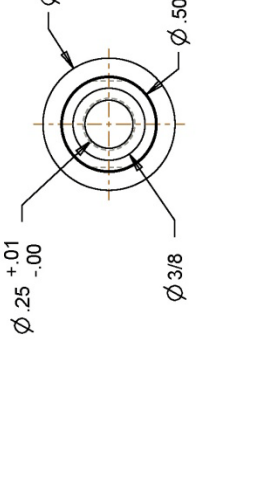
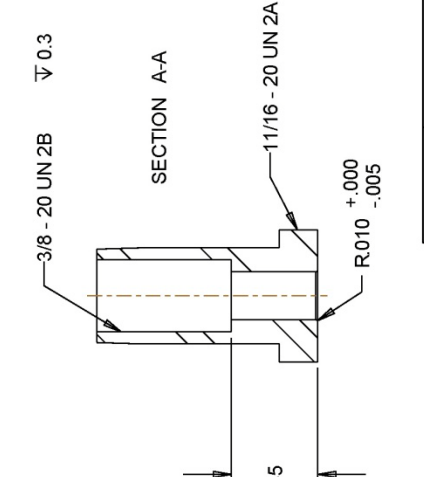
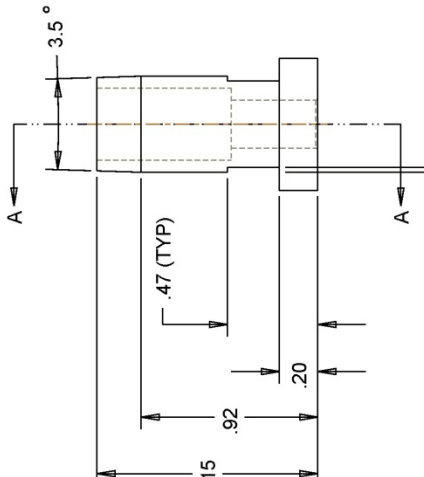
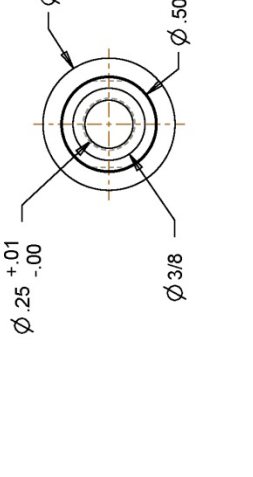
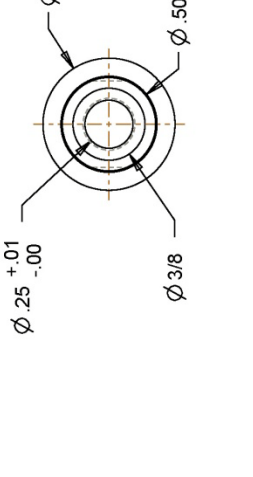
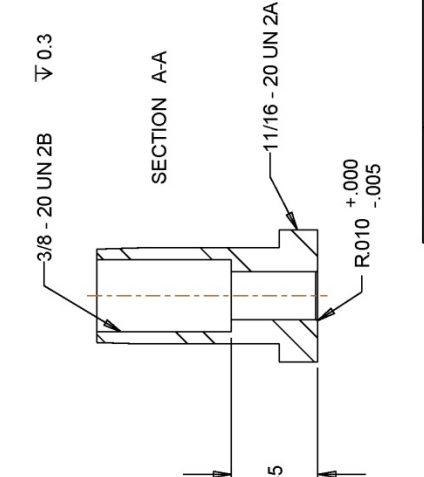
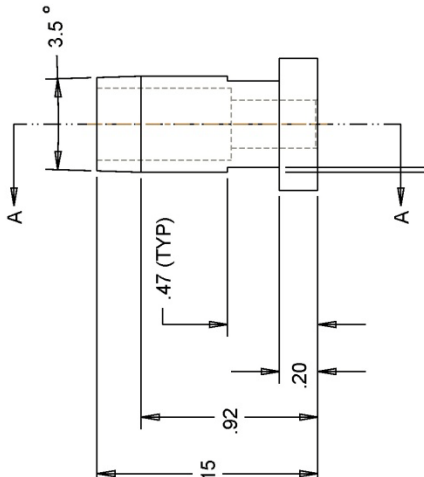
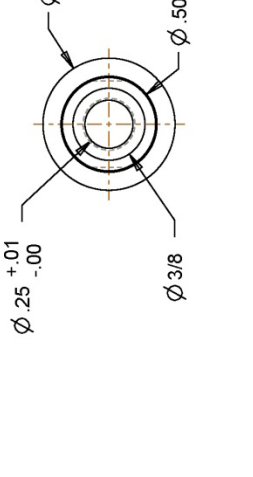
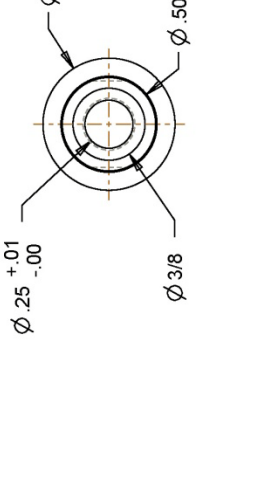
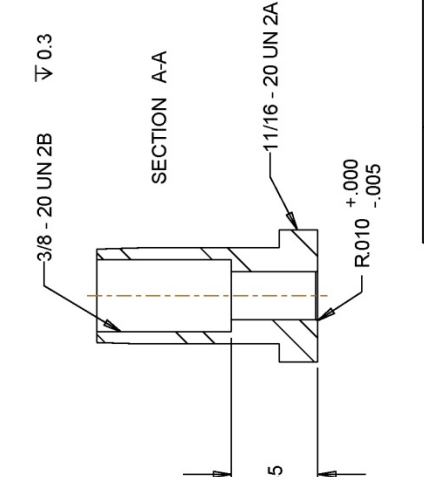
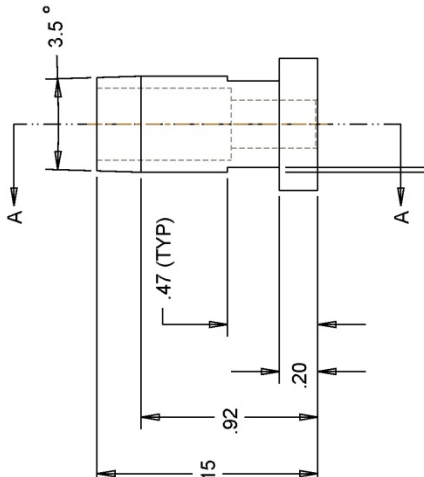
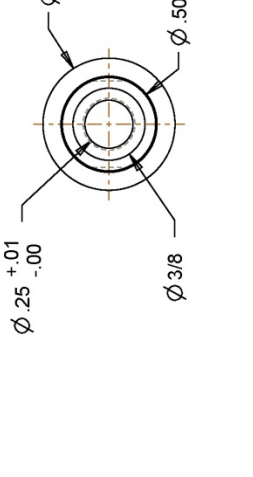
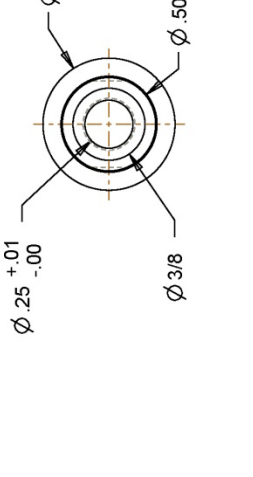
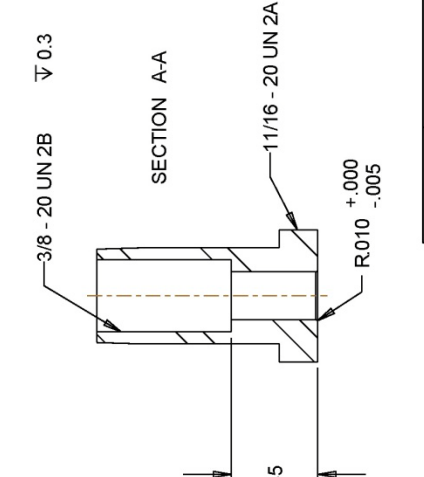
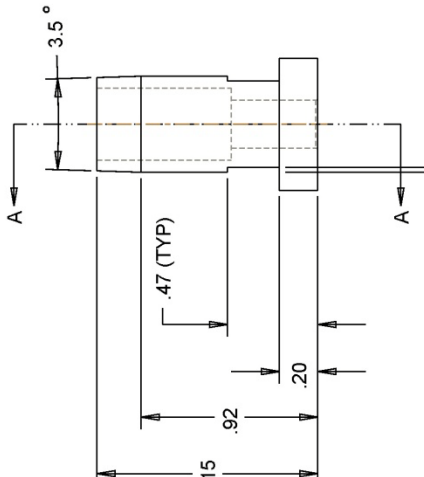
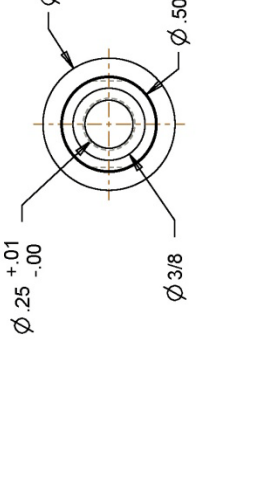
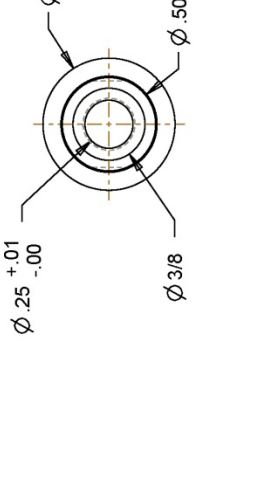
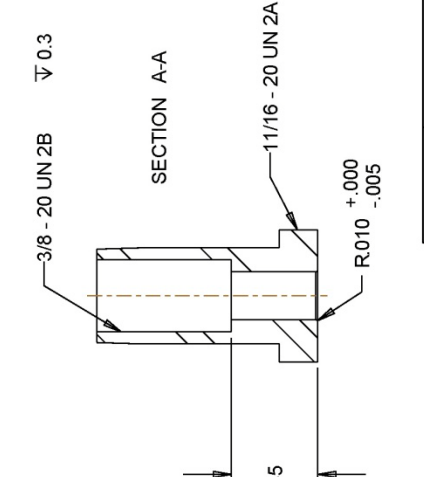
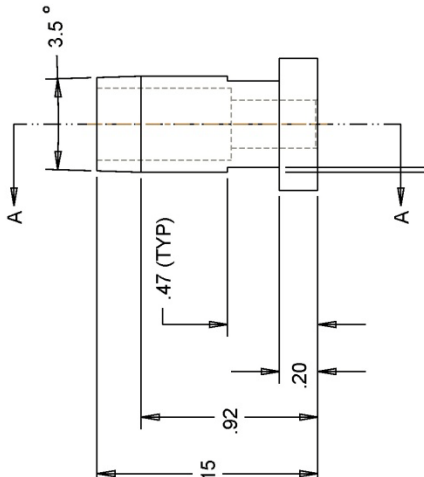
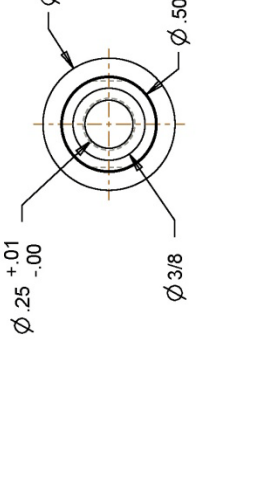
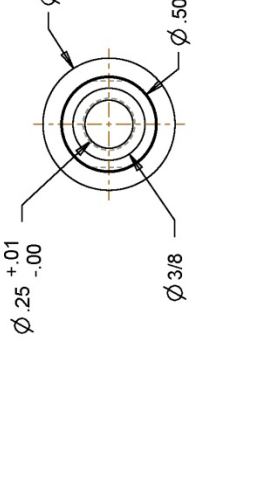
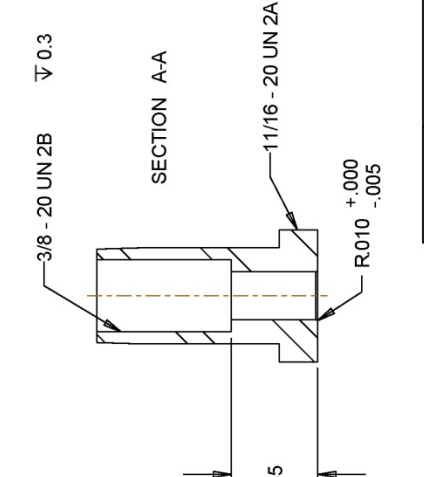
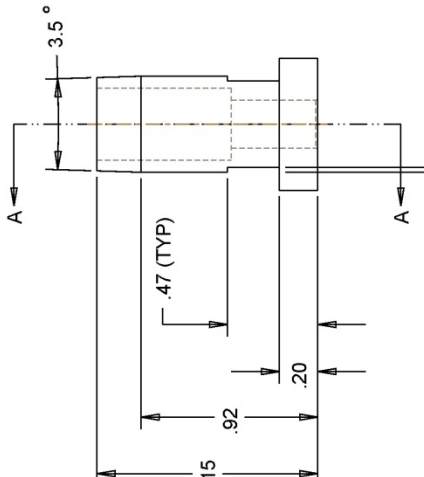
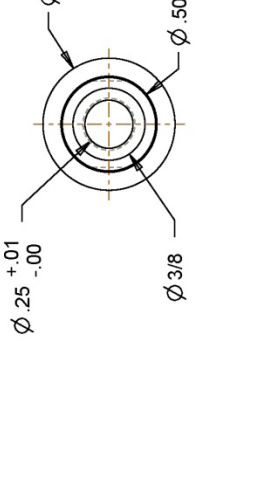
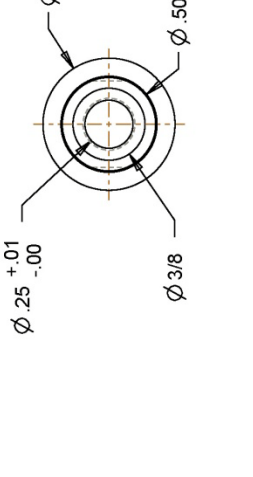
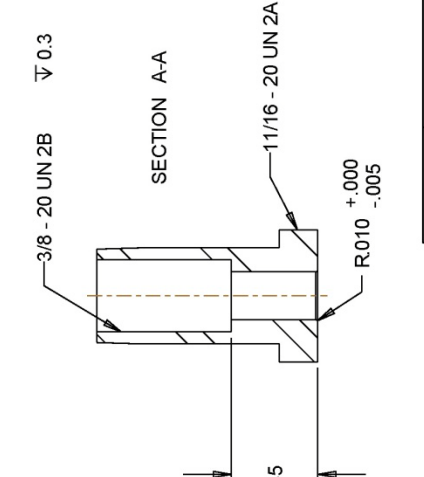
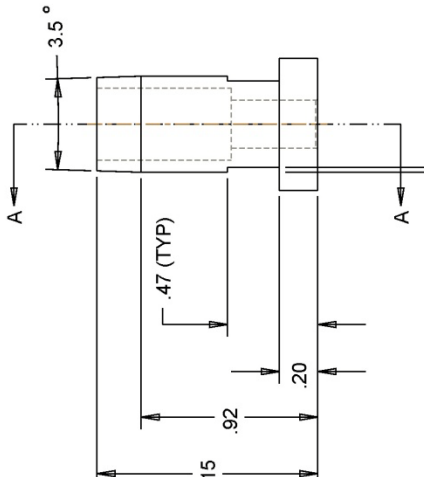
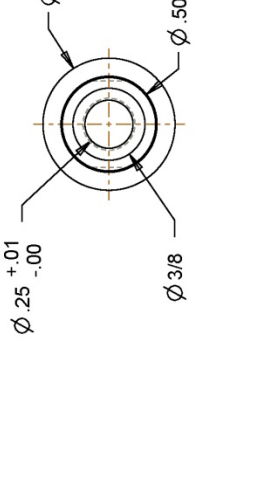
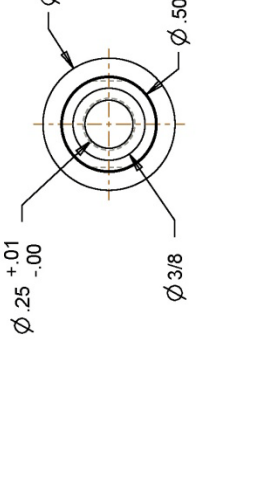
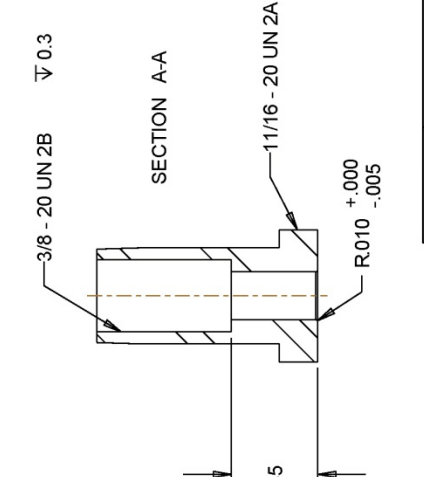
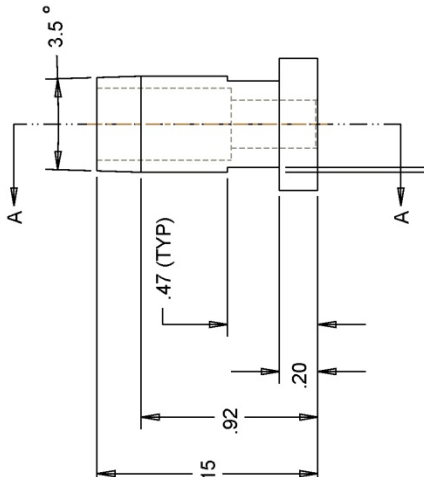
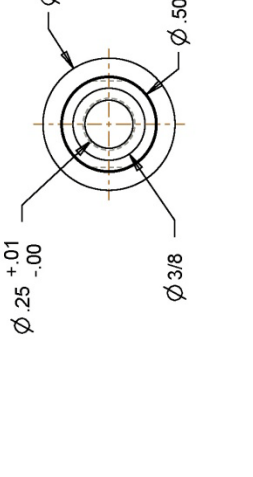
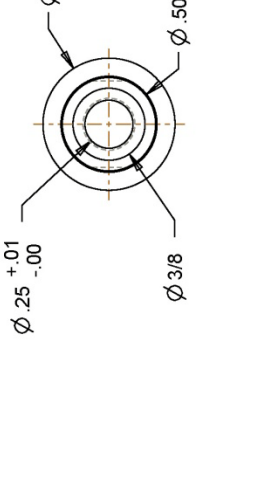
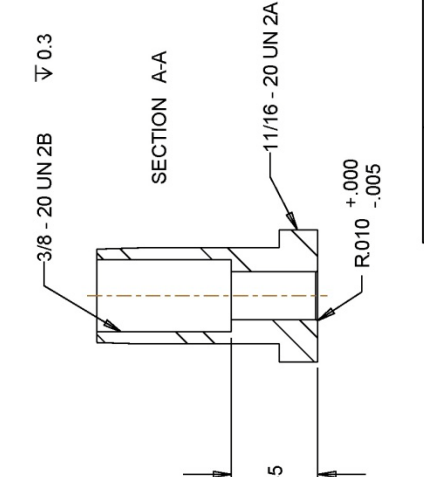
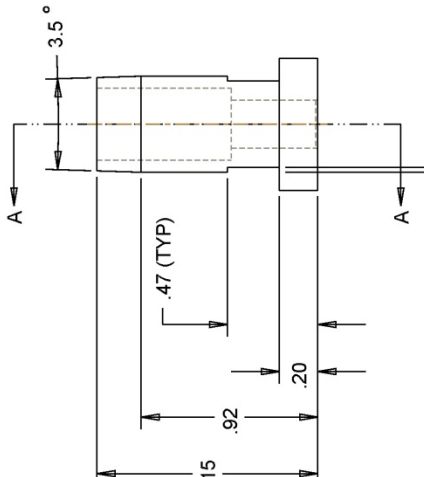
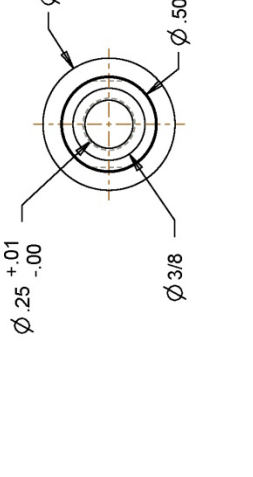
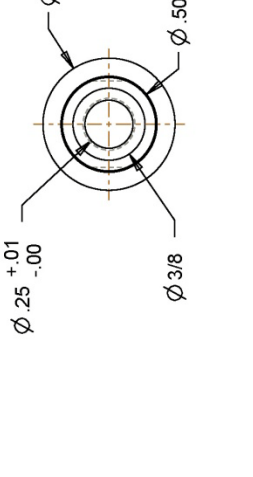
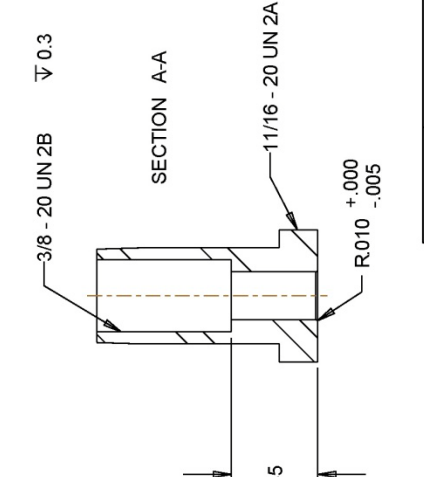
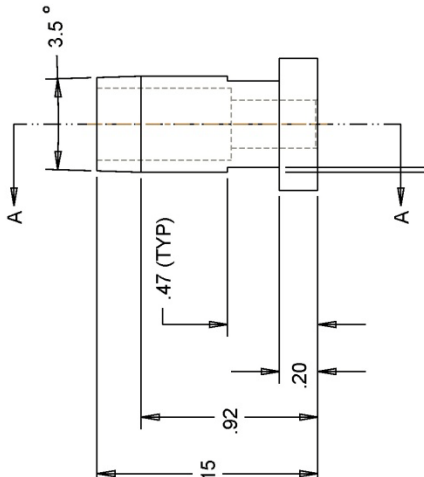
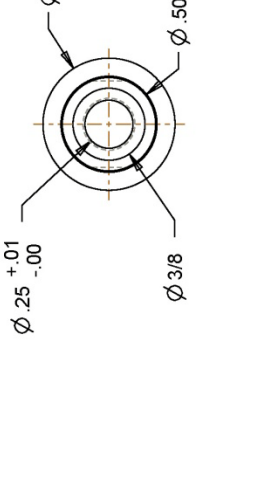
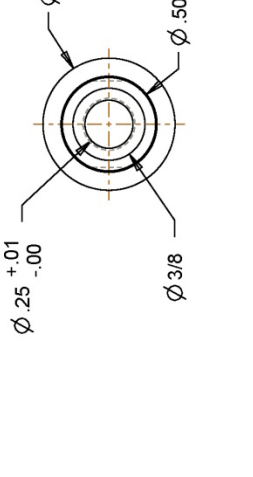
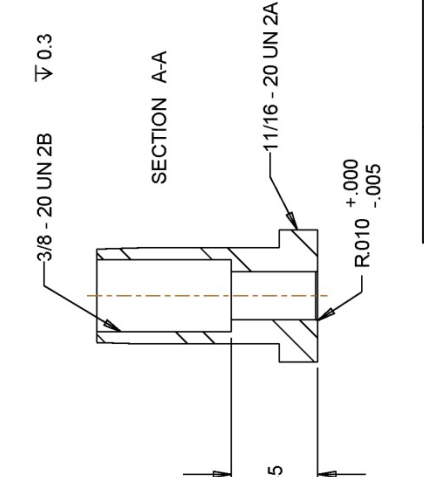
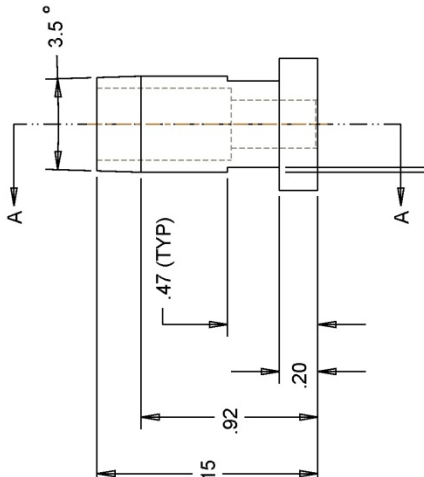
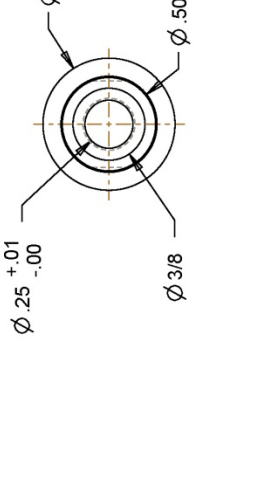
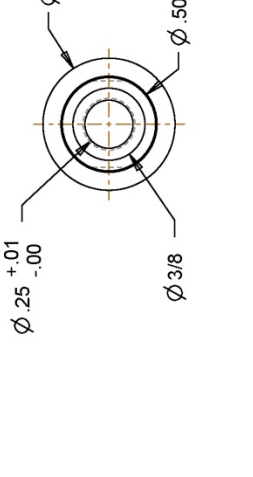
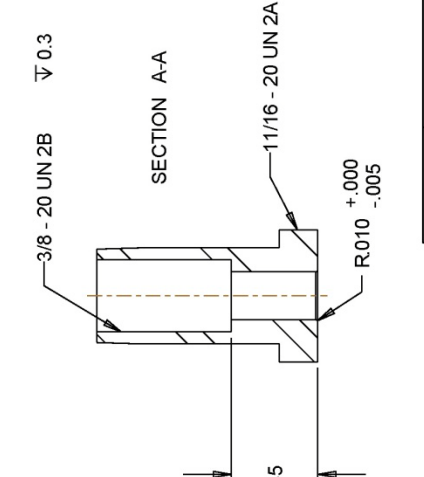
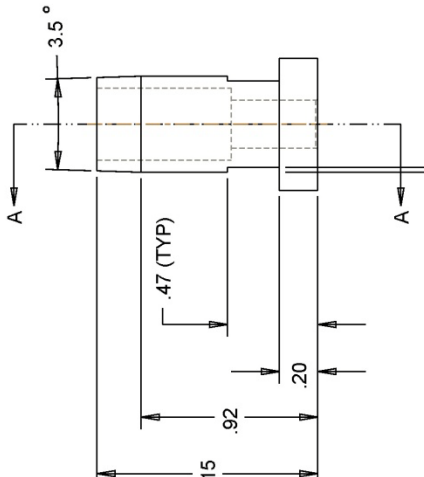
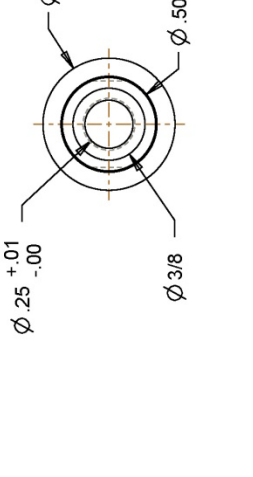
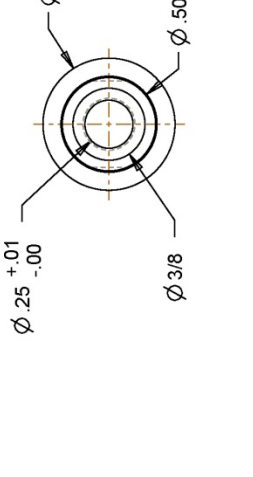
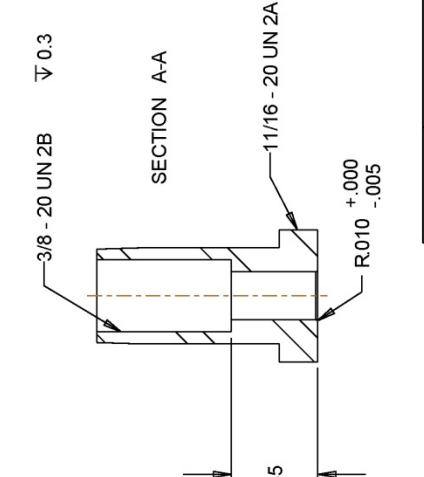
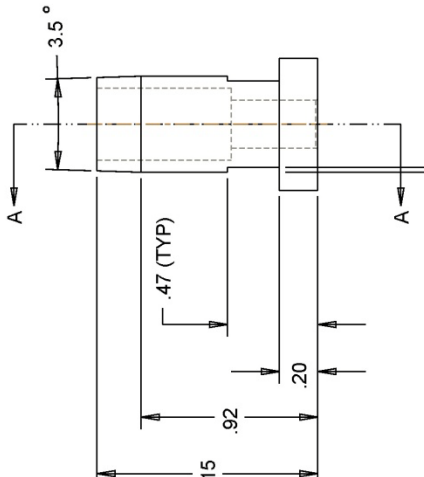
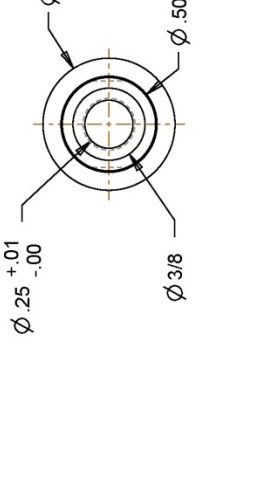
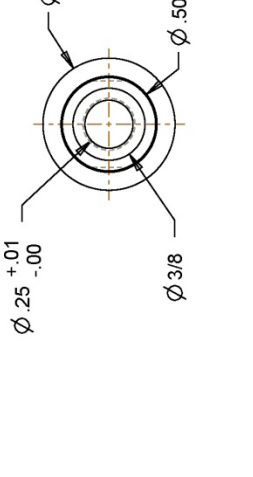
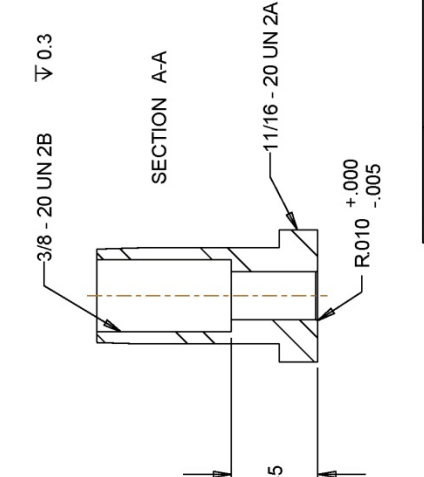
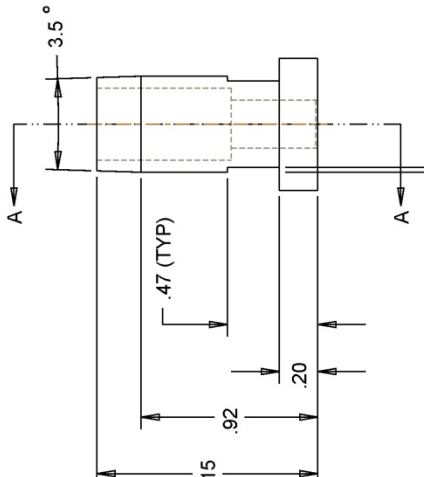
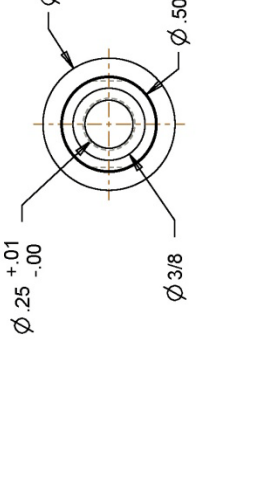
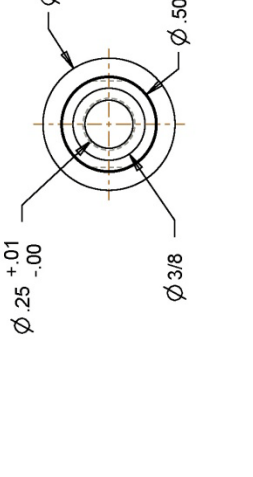
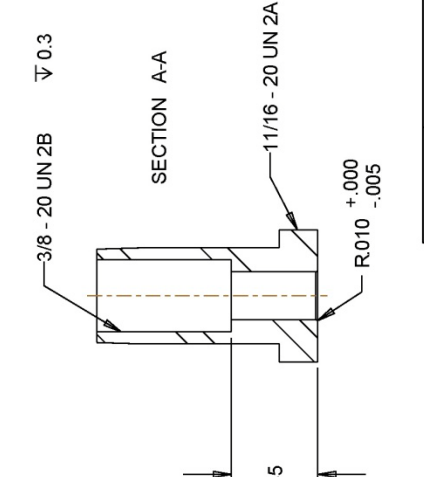
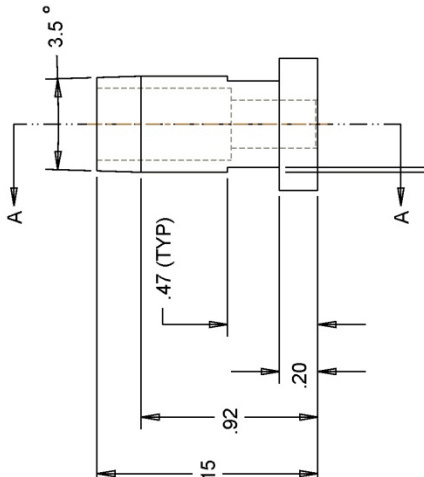
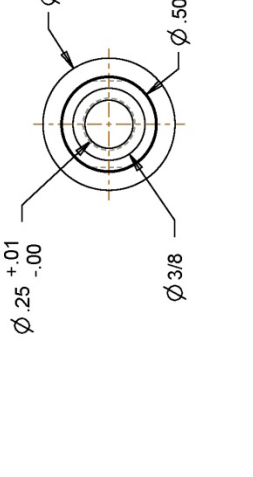
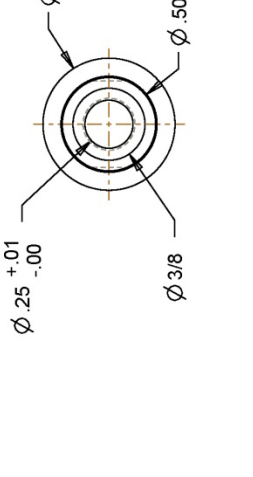
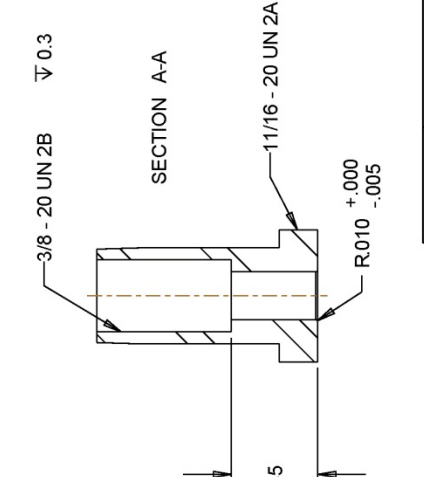
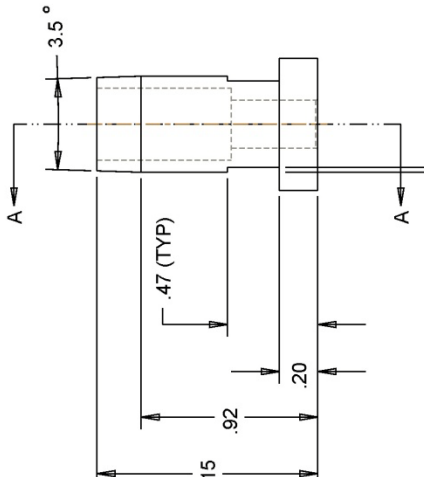
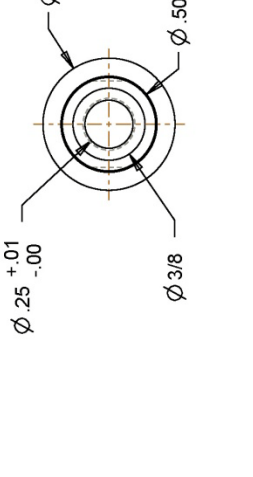
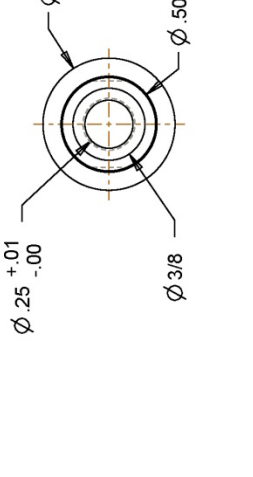
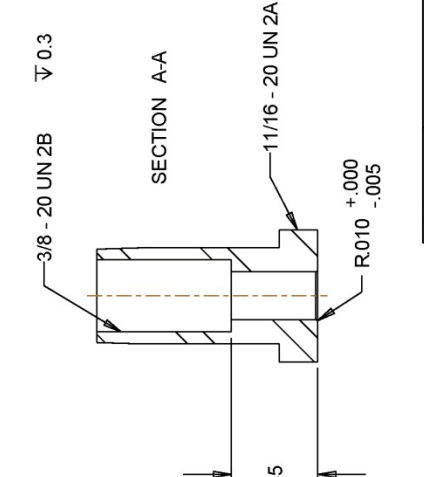
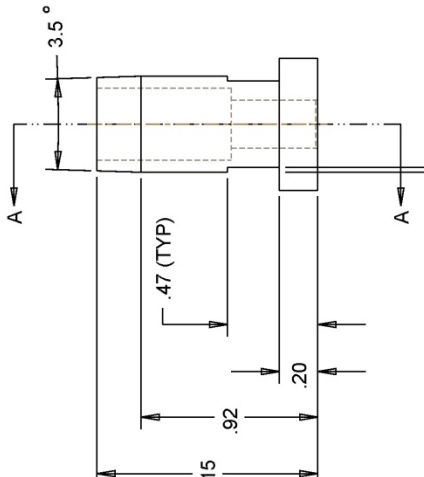
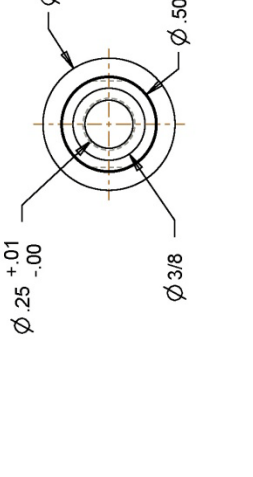
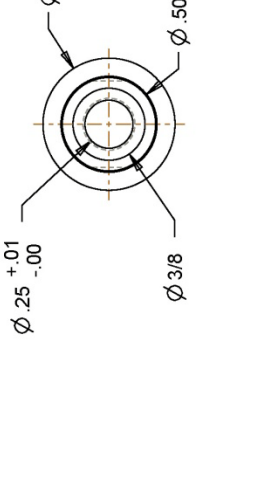
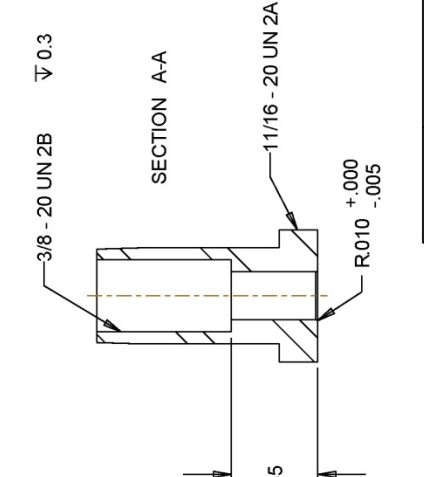
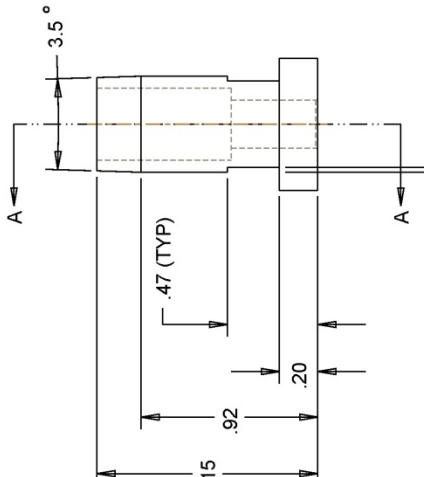
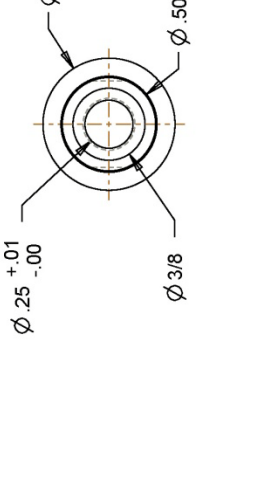
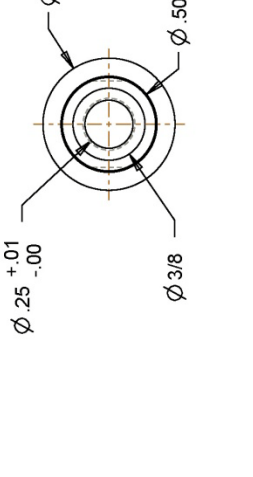
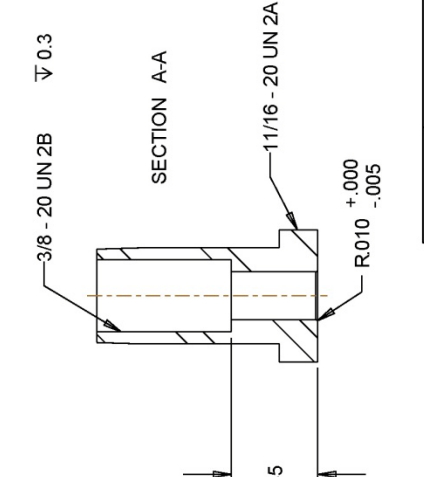
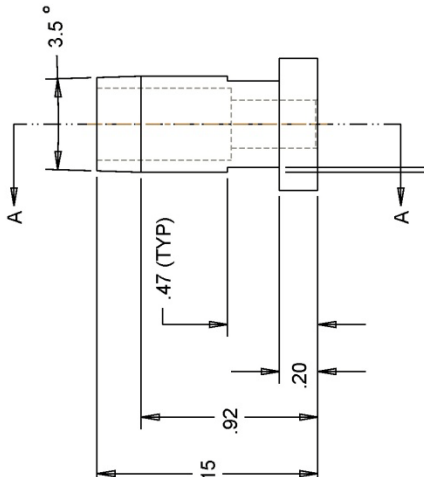
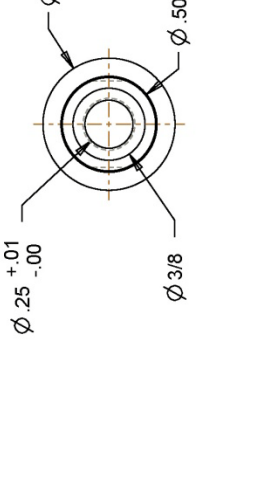
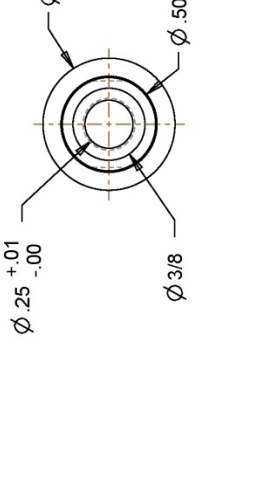
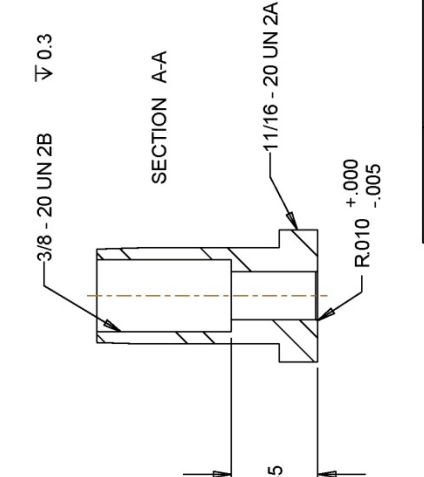
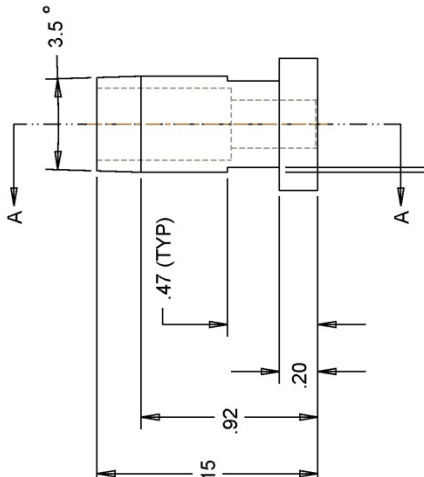
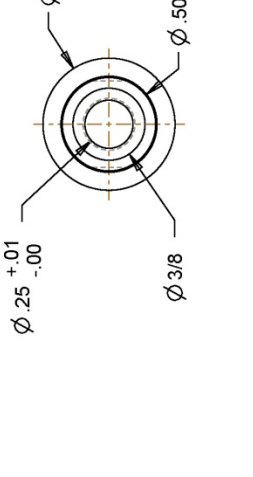
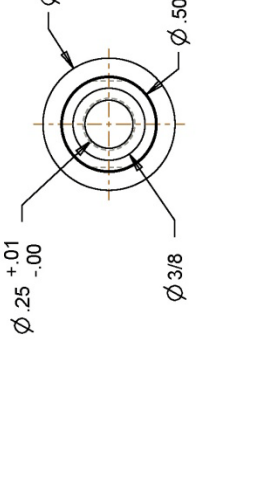
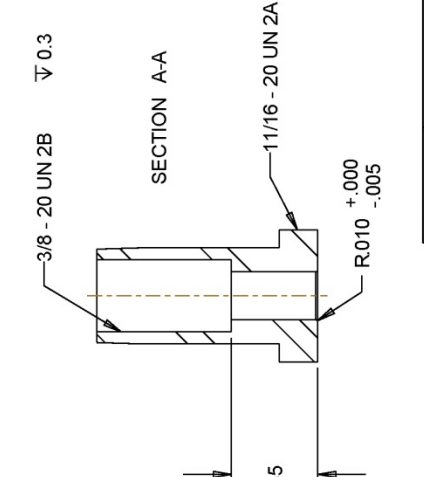
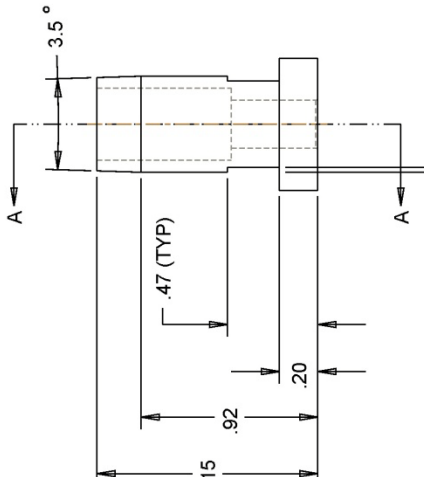
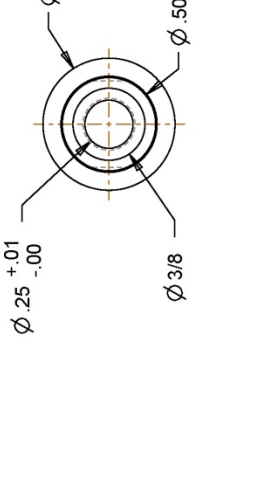
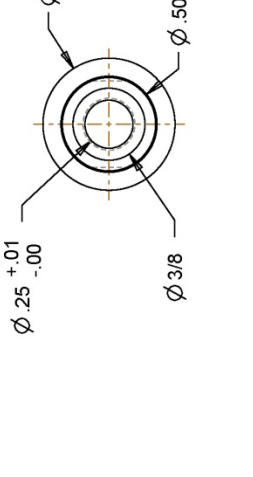
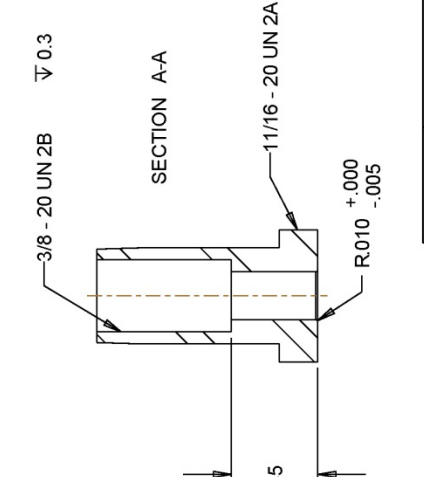
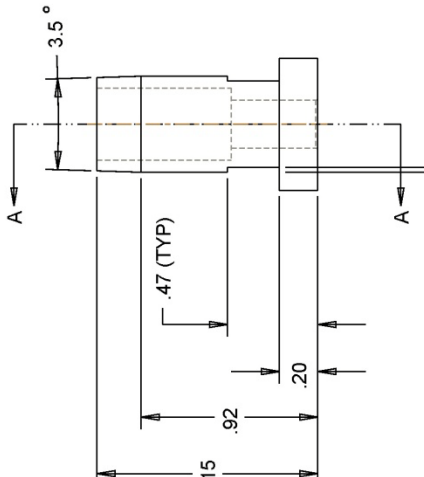
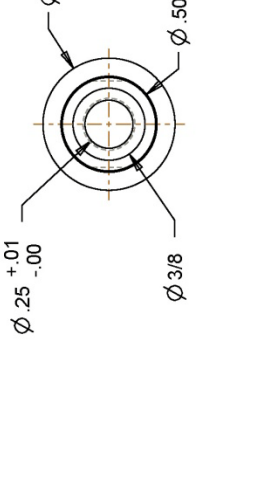
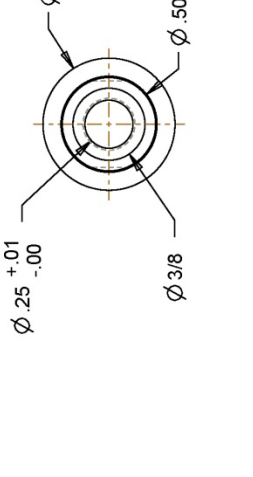
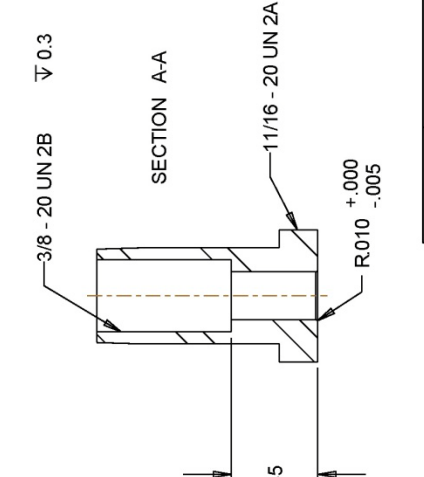
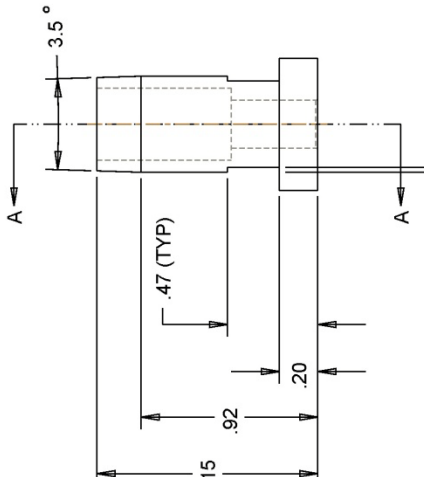
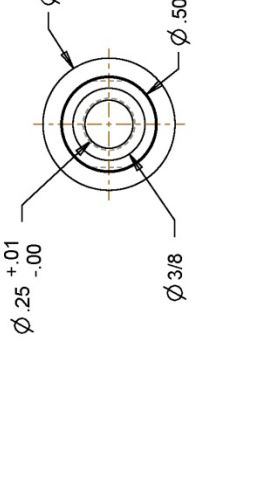
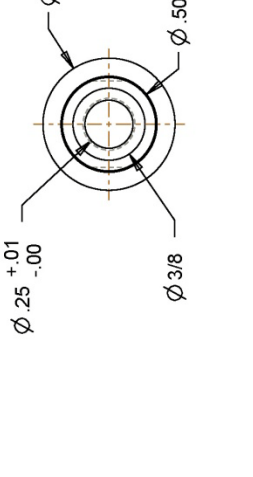
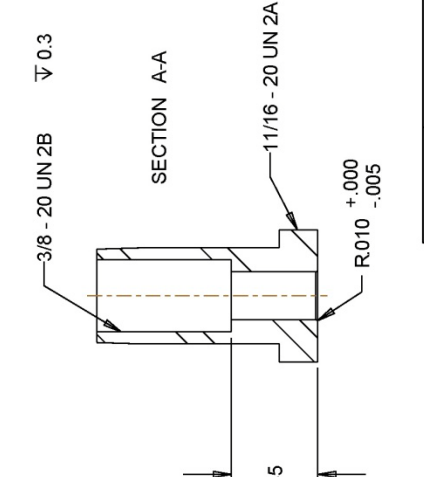
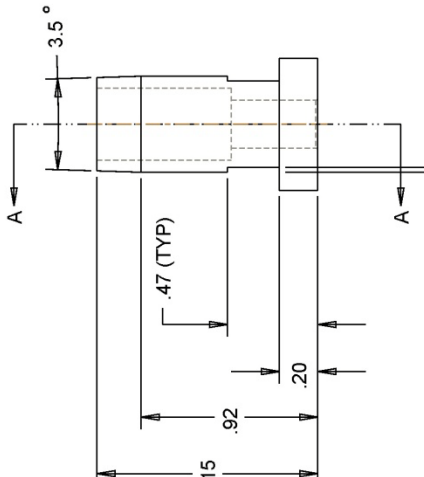
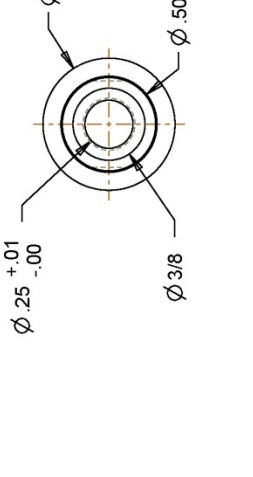
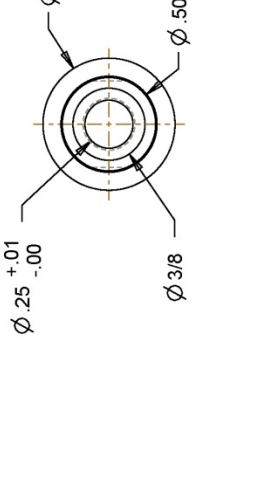
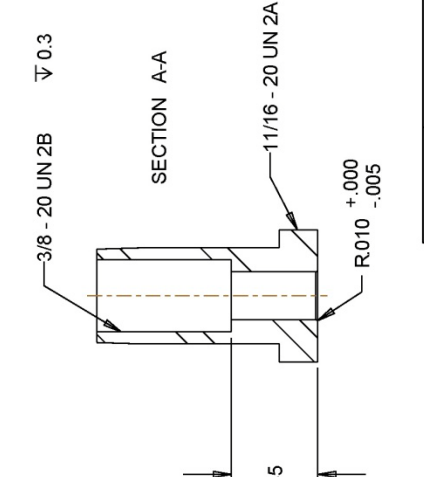
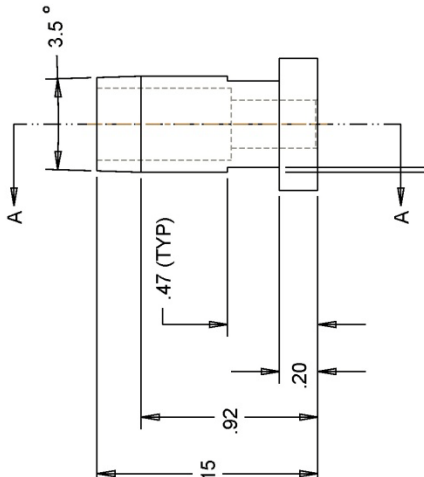
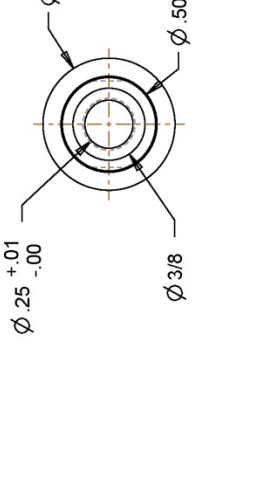
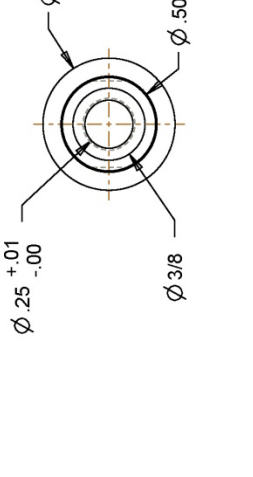
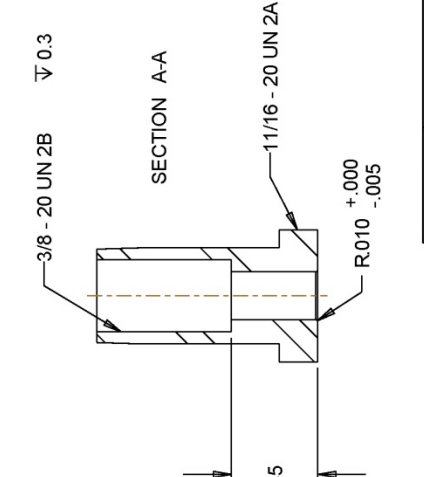
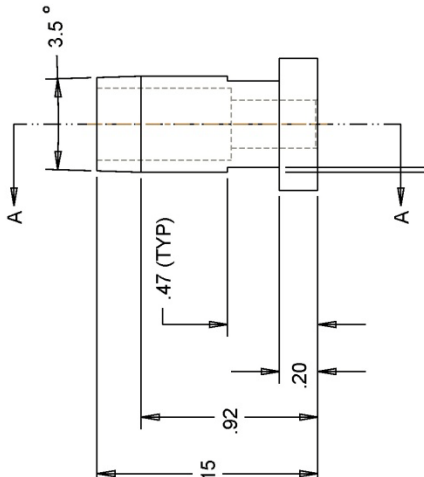
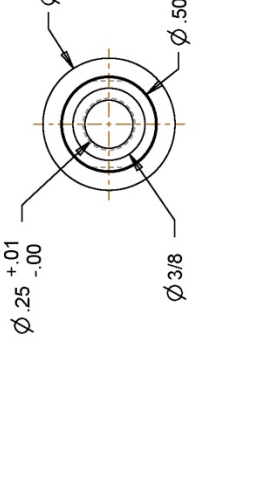
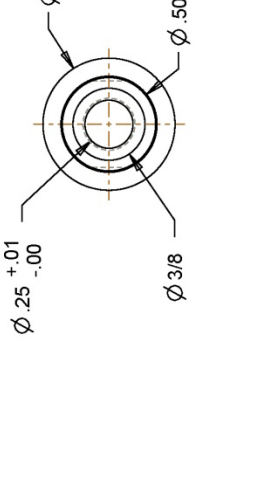
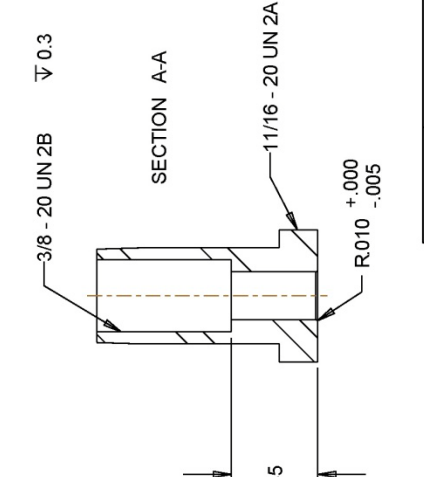
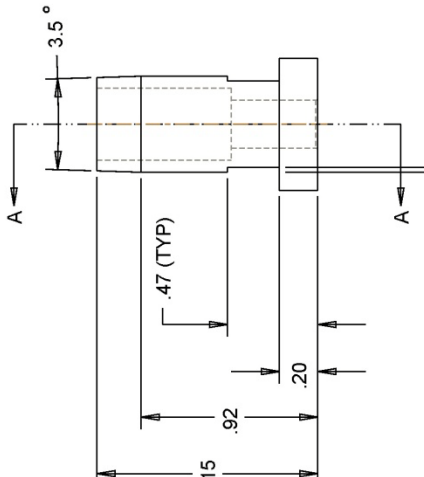
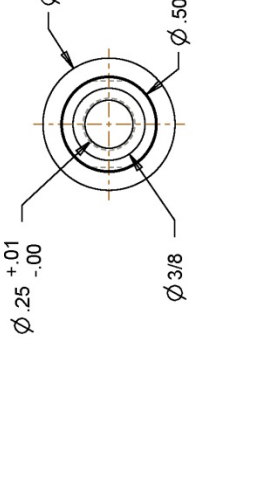
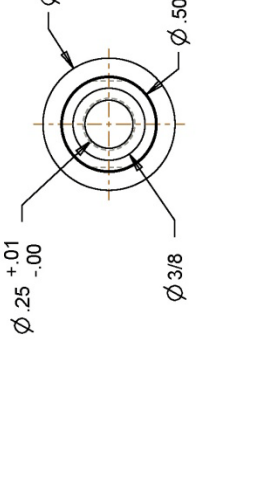
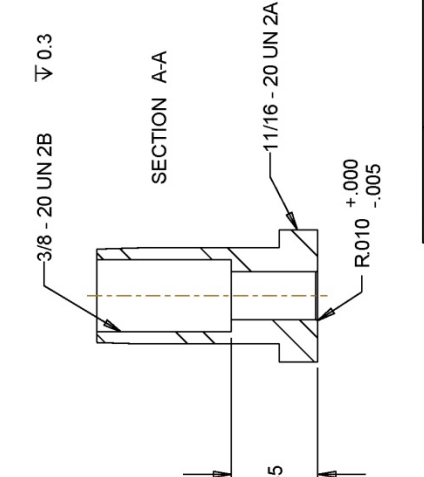
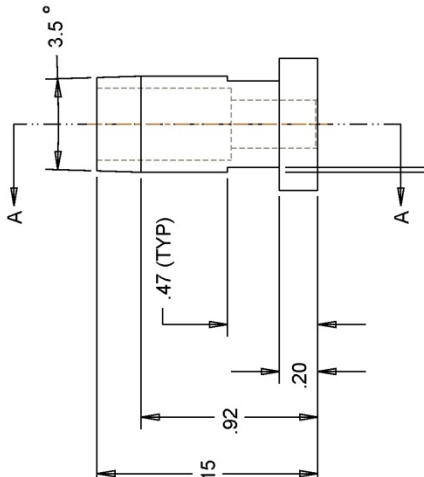
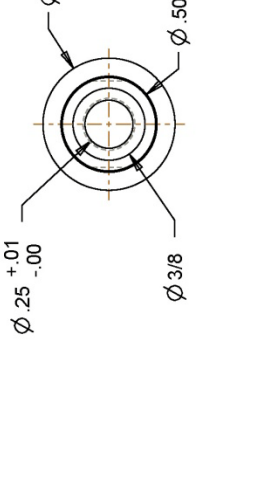
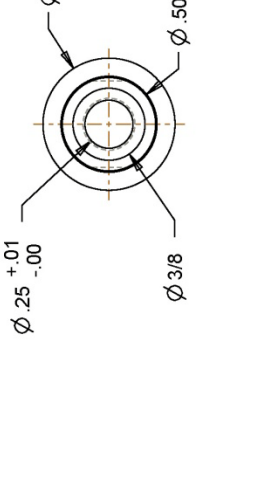
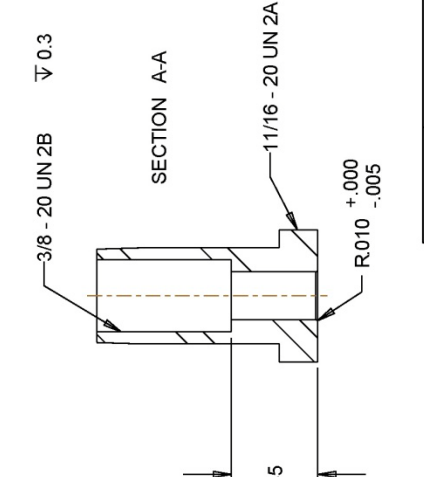
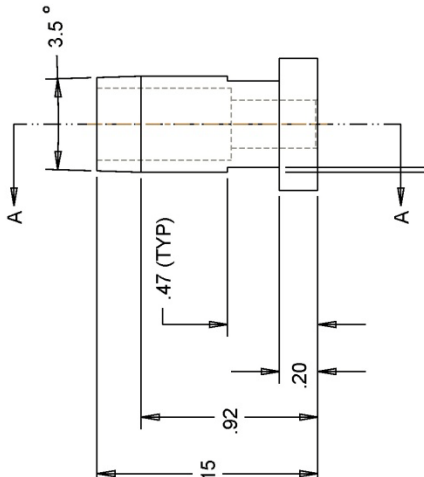
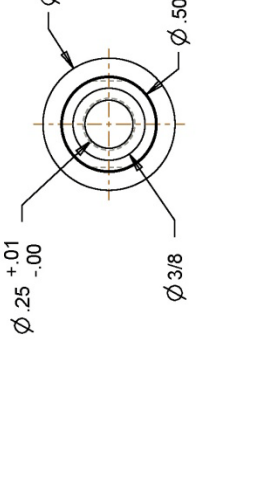
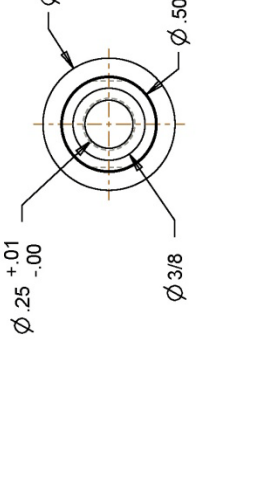
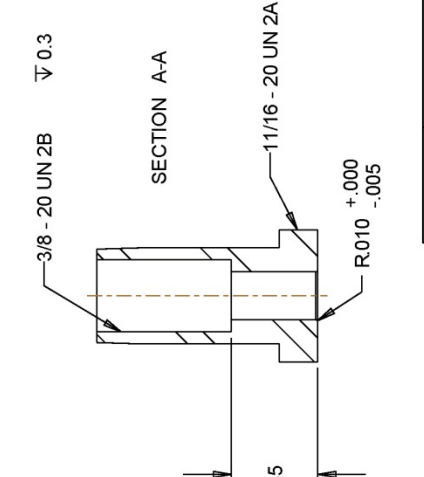


This technical drawing consists of several views:

- Front View:** Shows the part's overall shape, featuring a central hole with a diameter of $\phi 3.95$ REF, a shoulder of $\phi 5.750^{+.000}_{-.005}$, and a flange with a radius of $R2.375$. The outer diameter is $6X \phi .400 \pm .004$. A note specifies "Break all edges".
- Section A-A:** A longitudinal cross-section showing internal features like a shoulder of $R1.06$, a shoulder of $R.75^{+.015}_{-.00}$, and a shoulder of $R.02^{+.01}_{-.00}$. It also shows a shoulder of $R10$ and a shoulder of $\phi 2.45$.
- Detail A:** An enlarged view of the top edge of the flange, showing a shoulder of $\phi 2.250^{+.000}_{-.001}$ and a shoulder of $\phi 1.9800^{+.0000}_{-.0009}$.
- Revision History:** A table showing the revision history with columns for REV, DESCRIPTION, BY, DATE, and APFR.
- Departmental Information:** Includes the department name, university, and file number.
- Dimensions:** Overall dimensions include $5/16^{+.1/32}_{-.0}$ for the outer width, 1.755 and 1.745 for shoulder widths, and 1.06 for the shoulder height.



1

						REVISION HISTORY	
						REV	DESCRIPTION
						0	Prototype Release
							MR
							07-Jul-08
D	$\phi .25^{+.01}_{-.00}$	$\phi 3/8$	$\phi 11/16$	$\phi .50$	$.92$	$.47 \text{ (TYP)}$	$.20$
C							
B							
A							
O							
C							
B							
A							
O							
C							
B							
A							
O							
C							
B							
A							
O							
C							
B							
A							
O							
C							
B							
A							
O							
C							
B							
A							
O							
C							
B							
A							
O							
C							
B							
A							
O							
C							
B							
A							
O							
C							
B							
A							
O							
C							
B							
A							
O							
C							
B							
A							
O							
C							
B							
A							
O							
C							
B							
A							
O							
C							
B							
A							
O							
C							
B							
A							
O							
C							
B							
A							
O							
C							
B							
A							
O							
C							
B							
A							
O							
C							
B							
A							
O							
C							
B							
A							
O							
C							
B							
A							
O							
C							
B							
A							
O							
C							
B							
A							
O							
C							
B							
A							
O							
C							
B							
A							
O							
C							
B							
A							
O							
C							
B							
A							
O							
C							
B							
A							
O							
C							
B							
A							
O							
C							
B							
A	<img alt="Front view showing overall dimensions 1.15, .92						

SECTION A-A

REV	DESCRIPTION	BY	DATE
0	Prototype Release	MR	07-Jul-08

FRONT VIEW

CROSS SECTION

SECTION A-A

MATERIAL: 1018
CONDITION: As-rolled

FINISH: -

DIMENSIONS:

- Outer Diameter: $\phi 32$ (+0.00, -0.01)
- Shoulder Diameter: $\phi 20$ (+0.10, -0.05)
- Shoulder Height: .10 (TYP)
- Counterbore Diameter: $2 \times \phi 38$
- Break all edges

TOLERANCES:

UNITS	SPECIFIED	APPLIED
INCHES	0.015	0.015
MM	0.382	0.382
INCHES	0.001	0.001
MM	0.025	0.025
INCHES	0.005	0.005
MM	0.127	0.127
INCHES	0.000	0.000
MM	0.000	0.000

SURFACE FINISH:

SPECIFIED	APPLIED
Unspecified	Unspecified
Specified	Specified

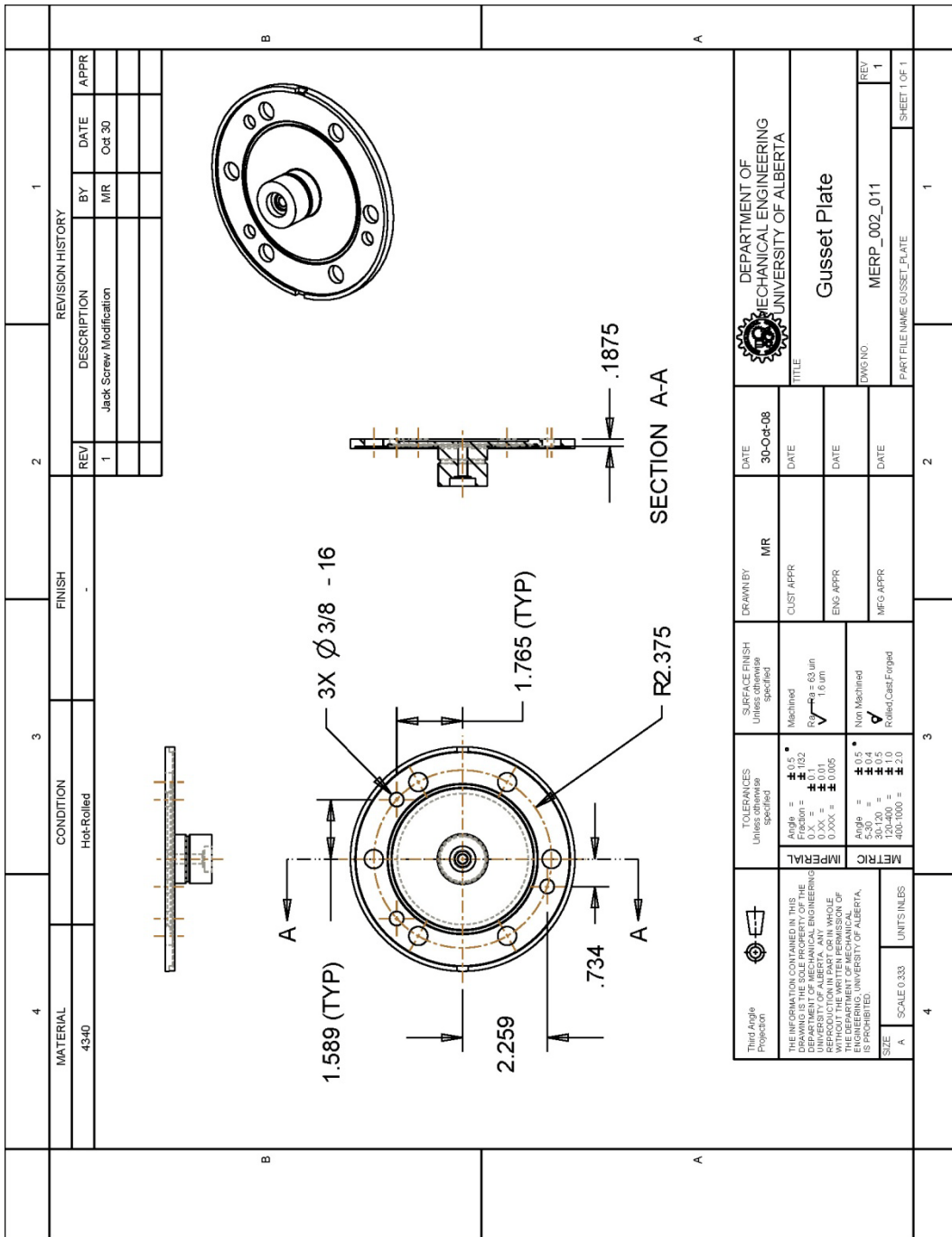
DRAWN BY: MR
DATE: 07-Jul-08

**DEPARTMENT OF MECHANICAL ENGINEERING
THE UNIVERSITY OF ALBERTA**

Ball Set Screw

ITEM NO.	NAME	REV
0	MRP_002_017	0

SCALE: 1:100
UNITS: MM
SHEET 1 OF 1



H. MATLAB CODE

H.1 \dot{m} , D, and k'

```
%%%%%%  
%Six-Layer - 1000 Pounds  
%%%%%  
%Read in the data  
[vec]=dlmread('ma_6L_dc1000_929.lvm');  
cutoff=10; %Remove the first 10 sample points  
vec1=vec(cutoff:length(vec),:);  
clear vec;  
  
%%%%%  
%Separate pressure data into columns  
%%%%%  
%Time  
time1=vec1(:,1);  
time1=time1/3600; %[hr]  
clear time;  
  
%Thermocouple Gauge  
therm1=vec1(:,2);  
therm1=0.0027*exp(3.0489*therm1); %Convert voltage into Torr  
  
%Capacitance Manometer  
cap1=vec1(:,3);  
cap1=cap1*100; %Convert voltage into Torr  
  
%Validyne DP15  
DP1=vec1(:,4);  
DP1=(760/101.325)*(DP1-0.0679)/0.0913; %Convert voltage into Torr
```

```

%%%%%%%%%%%%%
%Temperature
%%%%%%%%%%%%%

%Environmental Temperature
temp1=vec1(:,5);

%Convert Temperature Voltage Signal to Celsius (Green Sensor)
temp1=-1481.96+sqrt(2.1961*10^6+(1.8639-temp1)/(3.88*10^(-6)));

%DDelete everything that is <= 20 C
for (i=1:length(temp1))
    if (temp1(i)<=20)
        temp1(i)=0;
    end;
end;

%DDelete everything that is above 30 C
for (i=1:length(temp1))
    if (temp1(i)>=30)
        temp1(i)=0;
    end;
end;
clear i;

%Remove 0 C temperatures, and average the remaining
t=find(temp1);
tempf1(1:length(t),:)=0;
tempf1(1:length(t),:)=temp1(t);
clear temp1;

```

```

temp1=mean(tempf1);
clear t tempf1;

%%%%%%%%%%%%%
%Filter the data
%%%%%%%%%%%%%

%FastsSmooth filter
thermy1=fastsSmooth(therm1,30000,3,1); %Thermocouple gauge
capy1=fastsSmooth(cap1,30000,3,1); %Capacitance manometer
DPy11=fastsSmooth(DP1,30000,3,1); %Validyne DP15
DPy1=mean(DPy11); %Assume the environmental pressure is constant

%Butterworth filter (for comparison purposes only)
[b,a]=butter(4,0.0002);
thermf1=filterfilt(b,a,therm1);
capf1=filterfilt(b,a,cap1);
DPf1=filterfilt(b,a,DP1);

%%%%%%%%%%%%%
%Properties
%%%%%%%%%%%%%
T1=temp1+273.15; %Environmental temperature [K]
V1=1034583.128/(1000^3); %System volume [m^3]
M1=28.97; %Molar Mass of Air [kg/kmol]
R1=8.315; %Universal Gas Constant [kJ/K/kmol]

L1=0.06711; %Strain gauge compensated for loading [m]
ri1=1*25.4; %Pipe inner radius [mm]
ro1=1.059*25.4; %Pipe outer radius [mm]

u11=1.80e-5; %Dynamic Viscosity of Air at 20 C [Pa s]

```

```

den11=1.20; %Density of air at 20 C [kg/m^3]
di11=ri1*2*25.4/1000; %Inner diameter of 2 inch pipe [m]

%%%%%%%%%%%%%
%Linear curve fit calculations
%%%%%%%%%%%%%

%Linear model Poly1:
%    f(x) = p1*x + p2
%Coefficients (with 95% confidence bounds):
%    p1 = 0.07401 (0.07395, 0.07408)
%    p2 = 0.1048 (0.1044, 0.1052)

%Goodness of fit:
% SSE: 1292
% R-square: 0.9358
% Adjusted R-square: 0.9358
% RMSE: 0.05856

%Linear curve fit coefficients
A11=0.07401;
B11=0.1048;

%Linear curve fit lower 95% confidence interval coefficients
A110=0.07395;
B110=0.1044;

%Linear curve fit upper 95% confidence interval coefficients
A1100=0.07408;
B1100=0.1052;

%%%%%%%%%%%%%
%Pressure versus time linear curve fit
%%%%%%%%%%%%%

```

```

P11=A11.*time1+B11; %Pressure versus time linear fit curve
P110=A110.*time1+B110; %Lower boundary linear fit curve
P1100=A1100.*time1+B1100; %Upper boundary linear fit curve

%%%%%%%%%%%%%%%
%First derivative of pressure versus time curve fit
%%%%%%%%%%%%%%%

%The linear fit derivative dP/dt
dPdt11=A11; %[Torr/hr]

%%%%%%%%%%%%%%
%Mass flow rate, diffusion, and intrinsic permeability
%%%%%%%%%%%%%%

%Mass flow rate
mfr11=V1*M1/R1/T1.*dPdt11*101.325/760/3600-2.9791e-13; %[kg/s]
%Note: 2.9791e-13 kg/s is the system calibration from the multi-axial tube + plug
%data set

%Diffusion
DD11(1:length(time1),1)=0;
DD11(1:length(time1),1)=mfr11.*(ri1-
ro1).*R1.*T1./(2.*pi().*ri1.*L1.*M1.*((P11-DPy1)*101325./760).*1000;
%[m^2/s]

%Velocity
vel11=mfr11./(pi()./4*di11.^2.*den11); %[m/s]

%Intrinsic Permeability
k11=u11.*mfr11.*R1.*T1./M1.*((ro1-
ri1)./(2.*pi().*ri1.*L1).*2./((DPy1.*101325./760).^2-
(P11.*101325./760).^2)*1000; %Intrinsic Permeability [m^2]

```

```

%%%%%%%%%%%%%%%
%Plots
%%%%%%%%%%%%%%%

%Comparison of Unfiltered to Butterworth and FastsSmooth filtered data
axes1 = axes('Parent','figure','FontSize',16,'FontName','Arial');
box(axes1,'on');
hold(axes1,'all');
hold on;
plot(uftime1,uftherm1,'b'); %Unfiltered Data
plot(time1,thermf1,'r'); %4th Order Low-Pass Butterworth filter
plot(time1,thermy1,'k'); %FastsSmooth filter
xlabel('Time [hr]', 'fontsize',16,'fontname','arial')
ylabel('Pressure [Torr]', 'fontsize',16,'fontname','arial');
h=legend('Unfiltered','4th Order Low-Pass Butterworth','FastsSmooth');
set(h,'fontsize',12,'fontname','arial','location','Best');
hold on;
clear h;

%Comparison of FastsSmooth filtered to 95% Upper and Lower Bounds for 6th
Order Polynomial
axes1 = axes('Parent','figure','FontSize',16,'FontName','Arial');
box(axes1,'on');
hold(axes1,'all');
hold on;
plot(time1,thermy1,'b'); %FastsSmooth filter
plot(time1,P10,'r'); %95% Lower Boundary
plot(time1,P100,'k'); %95% Upper Boundary
xlabel('Time [hr]', 'fontsize',16,'fontname','arial')
ylabel('Pressure [Torr]', 'fontsize',16,'fontname','arial');
h=legend('FastsSmooth Filtered','Lower 95% Confidence Boundary','Upper 95%
Confidence Boundary');

```

```

set(h,'fontsize',12,'fontname','arial','location','Best');
hold on;
clear h;

%Plot of Mass Flow Rate versus time
axes1 = axes('Parent',figure,'FontSize',16,'FontName','Arial');
box(axes1,'on');
hold(axes1,'all');
plot(time1,mfr1,'b');
xlabel('Time [hr]', 'fontsize',16,'fontname','arial')
ylabel('Mass Flow Rate [kg/s]', 'fontsize',16,'fontname','arial');

%Plot of 6th Order Diffusion versus time
axes1 = axes('Parent',figure,'FontSize',16,'FontName','Arial');
box(axes1,'on');
hold(axes1,'all');
plot(time1,DD1,'b');
xlabel('Time [hr]', 'fontsize',16,'fontname','arial')
ylabel('Diffusion [m^2/s]', 'fontsize',16,'fontname','arial');

%Plot fastsmooth filtered data with curve fit boundaries for Linear Fit
axes1 = axes('Parent',figure,'FontSize',16,'FontName','Arial');
box(axes1,'on');
hold(axes1,'all');
hold on;
plot(time1,thermy1,'b');
plot(time1,P110,'r');
plot(time1,P1100,'k');
xlabel('Time [hr]', 'fontsize',16,'fontname','arial')
ylabel('Pressure [Torr]', 'fontsize',16,'fontname','arial');
h=legend('Fastsmooth Filtered','Lower 95% Confidence Boundary','Upper 95% Confidence Boundary');
set(h,'fontsize',12,'fontname','arial','location','Best');

```

```

hold on;
clear h;

%Plot Linear Diffusion versus time with constant DPy1
axes1 = axes('Parent',figure,'FontSize',16,'FontName','Arial');
box(axes1,'on');
hold(axes1,'all');
plot(time1,DD11,'b');
xlabel('Time [hr]', 'fontsize',16,'fontname','arial')
ylabel('Diffusion [m^2/s]', 'fontsize',16,'fontname','arial');

%Plot Linear Permeability versus time with constant DPy1
axes1 = axes('Parent',figure,'FontSize',16,'FontName','Arial');
box(axes1,'on');
hold(axes1,'all');
plot(time1,k11,'b');
xlabel('Time [hr]', 'fontsize',16,'fontname','arial')
ylabel('Permeability [m^2]', 'fontsize',16,'fontname','arial');

```

H.2 Stress and Strain

```
%%%%%%  
%Six Layer Strain  
%%%%%  
  
%Read in the data  
[vec1]=dlmread('mark6L1000.dat');  
  
%%%%%  
%Separate the data into columns  
%%%%%  
  
%Load  
load=vec1(:,1);  
load=load*500;  
  
%External Pipe Axial Strain  
ext_axial=vec1(:,2);  
  
%External Pipe Hoop Strain  
ext_hoop=vec1(:,3);  
  
%Internal Pipe Axial Strain  
int_axial=vec1(:,4);  
  
%Internal Pipe Hoop Strain  
int_hoop=vec1(:,5);  
  
%Time  
time=vec1(:,6); %Sampled at 100 Hz  
time=time/3600; %[hr]
```

```
%%%%%%  
%Adjust the time, load, and strain data to show a continuous reading  
%instead of three sets of data starting at time 0  
%%%%%%%%%
```

%Overall Time

```
time(185821:371640)=time(185821:371640)+time(185820);  
time(371641:length(time))=time(371641:length(time))+time(371640);
```

%Time for each test

```
time1(1:185820,1)=time(1:185820,1);  
time2(1:185820,1)=time(185821:371640);  
time3(1:185820,1)=time(371641:length(time));
```

%Load for each test

```
load1(1:185820,1)=load(1:185820,1);  
load2(1:185820,1)=load(185821:371640);  
load3(1:185820,1)=load(371641:length(load));
```

%External Pipe Axial Strain for each test

```
ext_axial=ext_axial-ext_axial(1); [% Strain] 5V=5%  
ext_axial1(1:185820,1)=ext_axial(1:185820,1);  
ext_axial2(1:185820,1)=ext_axial(185821:371640);  
ext_axial3(1:185820,1)=ext_axial(371641:length(ext_axial));
```

%External Pipe Hoop Strain for each test

```
ext_hoop=ext_hoop-ext_hoop(1);  
ext_hoop1(1:185820,1)=ext_hoop(1:185820,1);  
ext_hoop2(1:185820,1)=ext_hoop(185821:371640);  
ext_hoop3(1:185820,1)=ext_hoop(371641:length(ext_hoop));
```

%Internal Pipe Axial Strain for each test

```
int_axial=int_axial-int_axial(1);
```

```

int_axial1(1:185820,1)=int_axial(1:185820,1);
int_axial2(1:185820,1)=int_axial(185821:371640);
int_axial3(1:185820,1)=int_axial(371641:length(int_axial));

%Internal Pipe Hoop Strain for each test
int_hoop=int_hoop-int_hoop(1);
int_hoop1(1:185820,1)=int_hoop(1:185820,1);
int_hoop2(1:185820,1)=int_hoop(185821:371640);
int_hoop3(1:185820,1)=int_hoop(371641:length(int_hoop));

%Number of data samples in each set
t=1:length(time);

%%%%%%%%%%%%%
%Convert Strain Data to Longitudinal and Transverse Strain
%%%%%%%%%%%%%

%Longitudinal Strain - External Tube
str1_ext(1,length(ext_axial))=0;
str1_ext=0.25*ext_axial+0.75*ext_hoop;

str1_ext1(1:185820,1)=str1_ext(1:185820,1);
str1_ext2(1:185820,1)=str1_ext(185821:371640);
str1_ext3(1:185820,1)=str1_ext(371641:length(str1_ext));

%Transverse Strain - External Tube
str2_ext(1,length(ext_axial))=0;
str2_ext=0.75*ext_axial+0.25*ext_hoop;

str2_ext1(1:185820,1)=str2_ext(1:185820,1);
str2_ext2(1:185820,1)=str2_ext(185821:371640);
str2_ext3(1:185820,1)=str2_ext(371641:length(str2_ext));

```

```

%Longitudinal Strain - Internal Tube
str1_int(1,length(int_axial))=0;
str1_int=0.25*int_axial+0.75*int_hoop;

str1_int1(1:185820,1)=load(1:185820,1);
str1_int2(1:185820,1)=load(185821:371640);
str1_int3(1:185820,1)=load(371641:length(str1_int));

%Transverse Strain - Internal Tube
str2_int(1,length(int_axial))=0;
str2_int=0.75*int_axial+0.25*int_hoop;

str2_int1(1:185820,1)=str2_int(1:185820,1);
str2_int2(1:185820,1)=str2_int(185821:371640);
str2_int3(1:185820,1)=str2_int(371641:length(str2_int));

%%%%%%%%%%%%%
%Load versus time, and strain versus time plots
%%%%%%%%%%%%%

%Test 1 load versus time (0 - 1000 pounds)
subplot(2,3,1,'FontSize',16,'FontName','Arial'),plot(time1,load1,'b');
xlim([0 0.5167]);
ylim([0 4000]);
ylabel('Load [lbs]', 'FontSize',16,'FontName','Arial');

%Test 1 strain versus time (0 - 1000 pounds)
subplot(2,3,4,'FontSize',16,'FontName','Arial'),plot(time1,ext_axial1,'r');
xlim([0 0.5167]);
ylim([-0.2 0.7]);
hold on;
subplot(2,3,4,'FontSize',16,'FontName','Arial'),plot(time1,ext_hoop1,'g');

```

```

subplot(2,3,4,'FontSize',16,'FontName','Arial'),plot(time1,int_axial1,'c');
subplot(2,3,4,'FontSize',16,'FontName','Arial'),plot(time1,int_hoop1,'m');
subplot(2,3,4,'FontSize',16,'FontName','Arial'),plot(time1,str2_int1,'b');
subplot(2,3,4,'FontSize',16,'FontName','Arial'),plot(time1,str2_ext1,'k');
ylabel('% Strain','FontSize',16,'FontName','Arial');

%Test 2 load versus time (1000 - 2000 pounds)
subplot(2,3,2,'FontSize',16,'FontName','Arial'),plot(time2,load2,'b');
xlim([0.5167 1.033]);
ylim([0 4000]);

%Test 2 strain versus time (1000 - 2000 pounds)
subplot(2,3,5,'FontSize',16,'FontName','Arial'),plot(time2,ext_axial2,'r');
xlim([0.5167 1.033]);
ylim([-0.2 0.7]);
hold on;
subplot(2,3,5,'FontSize',16,'FontName','Arial'),plot(time2,ext_hoop2,'g');
subplot(2,3,5,'FontSize',16,'FontName','Arial'),plot(time2,int_axial2,'c');
subplot(2,3,5,'FontSize',16,'FontName','Arial'),plot(time2,int_hoop2,'m');
subplot(2,3,5,'FontSize',16,'FontName','Arial'),plot(time2,str2_int2,'b');
subplot(2,3,5,'FontSize',16,'FontName','Arial'),plot(time2,str2_ext2,'k');
xlabel('Time [Hr]','FontSize',16,'FontName','Arial');

%Test 3 load versus time (2000 - 3000 pounds)
subplot(2,3,3,'FontSize',16,'FontName','Arial'),plot(time3,load3,'b');
xlim([1.033 1.55]);
ylim([0 4000]);

%Test 3 strain versus time (2000 - 3000 pounds)
subplot(2,3,6,'FontSize',16,'FontName','Arial'),plot(time3,ext_axial3,'r');
xlim([1.033 1.55]);
ylim([-0.2 0.7]);
hold on;

```

```

subplot(2,3,6,'FontSize',16,'FontName','Arial'),plot(time3,ext_hoop3,'g');
subplot(2,3,6,'FontSize',16,'FontName','Arial'),plot(time3,int_axial3,'c');
subplot(2,3,6,'FontSize',16,'FontName','Arial'),plot(time3,int_hoop3,'m');
subplot(2,3,6,'FontSize',16,'FontName','Arial'),plot(time3,str2_int3,'b');
subplot(2,3,6,'FontSize',16,'FontName','Arial'),plot(time3,str2_ext3,'k');

%Plot legend, and axis labels
h=legend('Ext Axial','Ext Hoop','Int Axial','Int Hoop','Int Transverse','Ext Transverse');
set(h,'fontsize',12,'fontname','arial','Position',[0.1874 0.3149 0.1258 0.1833]);
hold on;
clear h;

%%%%%%%%%%%%%
%Stress versus strain plots
%%%%%%%%%%%%%

%Tube Diameters
do_int=1.628; %Internal pipe outer diameter [in]
di_int=1.5; %Internal pipe inner diameter [in]
A_int=pi()*di_int*(do_int-di_int)/2;

do_ext=2.122; %External pipe outer diameter [in]
di_ext=2; %External pipe inner diameter [in]
A_ext=pi()*di_ext*(do_ext-di_ext)/2;

Ratio_int=A_int/(A_int+A_ext);
Ratio_ext=A_ext/(A_int+A_ext);

%Internal Tube Axial Stress
stress_int1(1:185820,1)=Ratio_int.*load(1:185820,1)./0.22481./A_int; %[MPa]
stress_int2(1:185820,1)=Ratio_int.*load(185821:371640)./0.22481./A_int;
%[MPa]

```

```
stress_int3(1:185820,1)=Ratio_int.*load(371641:length(load))./0.22481./A_int;
%[MPa]
```

```
%External Tube Axial Stress
```

```
stress_ext1(1:185820,1)=Ratio_ext.*load(1:185820,1)./0.22481./A_ext; %[MPa]
```

```
stress_ext2(1:185820,1)=Ratio_ext.*load(185821:371640)./0.22481./A_ext;
%[MPa]
```

```
stress_ext3(1:185820,1)=Ratio_ext.*load(371641:length(load))./0.22481./A_ext;
%[MPa]
```

```
%Stress vs strain plot
```

```
axes1 = axes('Parent',figure,'FontSize',16,'FontName','Arial');
```

```
box(axes1,'on');
```

```
hold(axes1,'all');
```

```
hold on;
```

```
plot(int_axial1,stress_int1,'b');
```

```
xlim([0 0.7]);
```

```
ylim([0 5000]);
```

```
hold on;
```

```
plot(int_axial2,stress_int2,'b');
```

```
plot(int_axial3,stress_int3,'b');
```

```
plot(ext_axial1,stress_ext1,'r');
```

```
plot(ext_axial2,stress_ext2,'r');
```

```
plot(ext_axial3,stress_ext3,'r');
```

```
%Plot legend, and axis labels
```

```
h=legend("Internal","","External","");
```

```
set(h,'fontsize',12,'fontname','arial');
```

```
xlabel('Axial Strain [%]', 'fontsize',16,'fontname','arial');
```

```
ylabel('Axial Stress [Psi]', 'fontsize',16,'fontname','arial');
```

```
hold on;
```

```
clear h;
```

H.3 Thermal Analysis

The following .m files in MATLAB call one another in the following order:

- loop.m - Contains \dot{Q}_{approx} , T_{approx} , and emissivity. This is the file that is run.
- optimizer.m – runs the loop.m file until the \dot{Q} values converge
- dual_wall.m – contains the specific pipe system information

Running loop.m in MATLAB generates an excel file called loop.xls, which contains the results of the analysis for the given pipe information in dual_wall.m and with the convergence values specified in optimizer.m.

H.3.1 loop.m

```
function loop()
%This function generates an Excel spreadsheet containing the effect of
%changing air pressure on the thermal resistance in a dual wall composite
%pipe.
%This function was written by Mark Ruhl on May 25, 2009.

format long;

Qapproxin=2.7116; %First guess of heat loss [W]
%P=101325/760*10^-9; %[Pa] Air pressure in the annulus : 101325/760 Pa = 1
Torr
P=101325; %Air pressure in the annulus [Pa]
T3in=7.8673; %First guess of surface 3 temperature [°C]

emis1(:,1) = (0.005:0.001:1); %emissivity of surface 1
emis2(:,1) = (0.005:0.001:1); %emissivity of surface 2
emis3(:,1) = (0.005:0.001:1); %emissivity of surface 3

n=length(emis1);

%Generate the output data matrix and make all values 0
column(1:n)=0;
column=column';
[data] = [[column] [column] [column] [column] [column] [column] [column] [column]
[column] [column] [column] [column] [column]];

%Run the thermodynamic analysis and store the converged output in the data
%matrix for the specific emissivity value
for (row = 1:n)
    data(row,:) = optimizer(Qapproxin,emis1(row),emis2(row),emis3(row),P,T3in);
end;
```

```
%Write the data matrix to an excel file  
xlswrite('loop.xls',data);
```

H.3.2 optimizer.m

```
function [data] = optimizer(Qapproxin,emis1,emis2,emis3,P,T3in)
%This function determines Rtotal, Qactual and T3 iteratively by calling the
%dual_wall_air function.
%This function was written by Mark Ruhl on May 25, 2009.

format long;

Qin = Qapproxin;
T3 = T3in;

[Rtotal,Qactual,Qapprox,RaD,T3,T3kact,TfC] =  

dual_wall(Qin,emis1,emis2,emis3,P,T3);
count=1;

while (abs((abs(Qactual)-abs(Qapprox))/abs(Qactual))*100)>= 0.01  

[Rtotal,Qactual,Qapprox,RaD,T3,T3kact,TfC] =  

dual_wall(Qin,emis1,emis2,emis3,P,T3);
Qin=Qactual;
T3=T3kact;
count=count+1;
end;

%Output data matrix
[data] = [Rtotal Qactual Qapprox RaD T3in T3 T3kact P emis1 emis2 emis3  

TfC];  

%T3in is the first approximation made, T3 is the value used for the last
%iteration, and T3kact is the calculated T3 value from the last
%calculation.
```

H.3.3 dual_wall.m

```
function [Rtotal,Qactual,Qapprox,RaD,T3,T3kact,TfC] =  
dual_wall(Qapprox,emis1,emis2,emis3,P,T3)  
%This function determines the effective thermal resistance of a dual wall  
%pipe.  
%This function was written by Mark Ruhl on May 11, 2009 and modified on  
%December 29, 2009.  
  
%Surface 1 is the inside surface of the 1.5 inch inner pipe  
%Surface 2 is the outside surface of the 1.5 inch inner pipe  
%Surface 3 is the inside surface of the 2 inch outer pipe  
%Surface 4 is the outside surface of the 2 inch outer pipe  
  
format long;  
  
%%%%%%%%%%%%%%  
%Composite Tubular Specimen Dimensions  
%%%%%%%%%%%%%%  
%4-layer multi-axial pipe dimensions  
%ri1=double(1.5/2*25.4/1000); %[m]  
%ro1=double(1.601/2*25.4/1000); %[m]  
%ri2=double(2/2*25.4/1000); %[m]  
%ro2=double(2.122/2*25.4/1000); %[m]  
  
%6-layer multi-axial pipe dimensions  
ri1=double(1.5/2*25.4/1000); %[m]  
ro1=double(1.634/2*25.4/1000); %[m]  
ri2=double(2/2*25.4/1000); %[m]  
ro2=double(2.118/2*25.4/1000); %[m]  
  
%8-layer multi-axial pipe dimensions  
%ri1=double(1.5/2*25.4/1000); %[m]
```

```

%ro1=double(1.687/2*25.4/1000); %[m]
%ri2=double(2/2*25.4/1000); %[m]
%ro2=double(2.194/2*25.4/1000); %[m]

%%%%%%%%%%%%%
%Properties
%%%%%%%%%%%%%

L = double(1); %Pipe length in metres
Di=ri1*2; %Pipe ID [m]
Fij = double(1); %Shape factor
SB = double(5.6704*10^-8); %Stefan Boltzmann Constant
Toil = double(60); %Oil temperature in °C
Tair = double(4); %Air temperature in °C
voil = double(2); %Velocity of oil [m/s]
Nuoil = double(3.66); %Oil Nusselt number
g = double(9.81); %Gravity constant [m/s^2]
Do=2*ro2; %Outer diameter [m]
Lc = Do; %Characteristic length [m]
d = double(ri2-ro1); %Distance between surfaces 2 and 3
K=0.0284; %Thermal conductivity of air at room temperature and pressure
[W/m/K]

if Toil==20
    koil = double(0.145); %Conduction coefficient of oil at Toil [W/mC]
else if Toil==40
    koil = double(0.1444);
else if Toil==60
    koil = double(0.1404);
end;
end;
end;

```

```

%%%%%
%Calculate the k for the composite
%%%%%
kresin=double(0.21); %W/m/K
kbasalt=double(1.513); %W/m/K

```

%4-layer tubes

```

%Vf1=double(0.481); %Fiber volume fraction of 1.5 inch tube
%Vf2=double(0.412); %Fiber volume fraction of 2 inch tube

```

%6-layer tubes

```

Vf1=double(0.568); %Fiber volume fraction of 1.5 inch tube
Vf2=double(0.557); %Fiber volume fraction of 2 inch tube

```

%8-layer tubes

```

%Vf1=double(0.540); %Fiber volume fraction of 1.5 inch tube
%Vf2=double(0.532); %Fiber volume fraction of 2 inch tube

```

kcomp1=(Vf1)*kbasalt+(1-Vf1)*kresin; %Conduction coefficient of
 Basalt/Epoxy Composite [W/m/K]

kcomp2=(Vf2)*kbasalt+(1-Vf2)*kresin; %Conduction coefficient of
 Basalt/Epoxy Composite [W/m/K]

```

%%%%%
%Calculate conduction resistance for the 1.5 and 2 inch tubes
%%%%%
Rcond1 = double(log(ro1/ri1)/(2*pi()*L*kcomp1));
Rcond2 = double(log(ro2/ri2)/(2*pi()*L*kcomp2));

```

```

%%%%%
%Calculate convection from the oil to the 1.5 inch tube
%%%%%
hconv1 = double(Nuoil*koil/Di);

```

```

Rconvin = double(1/(hconv1*2*pi()*Di/2*L));

%%%%%%%%%%%%%%%
%Temperature Calculations
%%%%%%%%%%%%%%%
T1 = Toil; %[°C]
T1k = T1+273.15; %[K]
T2k = double(T1k - Qapprox*Rcond1); %[K]

emis = 1/(1/emis1+(1-emis2)/emis2*(ro1/ri2));

T3k=T3+273.15; %[K]
T4k = double(T3k - Qapprox*Rcond2); %[K]

Rcondvac           = double(log(ri2/ro1)/(2*pi()*L*K/(1+7.6*10^-
5*((T2k+T3k)/2)/P/d)));
if P==101325
    Rcondvac = double(log(ri2/ro1)/(2*pi()*L*K));
end;

Radvac=(T2k-T3k)/(emis*SB*(T2k^4-T3k^4)*2*pi()*ro1*L);

%%%%%%%%%%%%%%%
%Calculate Prandtl number, Kinematic Viscosity, and Conduction Coefficient
%%%%%%%%%%%%%%%
TfC = double((T4k-273.15+Tair)/2); %[°C]
TfK = double(TfC+273.15); %[K]

%Prandtl number properties
Pr0=double(0.7362);
Pr5=double(0.7350);
Pr10=double(0.7336);

```

```
Pr15=double(0.7323);
Pr20=double(0.7309);
Pr25=double(0.7296);
Pr30=double(0.7282);
Pr35=double(0.7268);
Pr40=double(0.7255);
Pr45=double(0.7241);
Pr50=double(0.7228);
```

%Conduction Coefficient properties [W/m/k]

```
k0=double(0.02364);
k5=double(0.02401);
k10=double(0.02439);
k15=double(0.02476);
k20=double(0.02514);
k25=double(0.02551);
k30=double(0.02588);
k35=double(0.02625);
k40=double(0.02662);
k45=double(0.02699);
k50=double(0.02735);
```

%Kinematic Viscosity properties [m²/s]

```
v0=double(1.338*10^-5);
v5=double(1.382*10^-5);
v10=double(1.426*10^-5);
v15=double(1.470*10^-5);
v20=double(1.516*10^-5);
v25=double(1.562*10^-5);
v30=double(1.608*10^-5);
v35=double(1.655*10^-5);
v40=double(1.702*10^-5);
v45=double(1.750*10^-5);
```

```

v50=double(1.798*10^-5);

if (TfC >= 5) && (TfC < 10)
    Prair = double(Pr5-(5-TfC)*(Pr5-Pr10)/(5-10));
    kair = double(k5-(5-TfC)*(k5-k10)/(5-10));
    vair = double(v5-(5-TfC)*(v5-v10)/(5-10));

else if (TfC >= 0) && (TfC < 5)
    Prair = double(Pr0-(0-TfC)*(Pr0-Pr5)/(0-5));
    kair = double(k0-(0-TfC)*(k0-k5)/(0-5));
    vair = double(v0-(0-TfC)*(v0-v5)/(0-5));

else if (TfC >= 10) && (TfC < 15)
    Prair = double(Pr10-(10-TfC)*(Pr10-Pr15)/(10-15));
    kair = double(k10-(10-TfC)*(k10-k15)/(10-15));
    vair = double(v10-(10-TfC)*(v10-v15)/(10-15));

else if (TfC >= 15) && (TfC < 20)
    Prair = double(Pr15-(15-TfC)*(Pr15-Pr20)/(15-20));
    kair = double(k15-(15-TfC)*(k15-k20)/(15-20));
    vair = double(v15-(15-TfC)*(v15-v20)/(15-20));

else if (TfC >= 20) && (TfC < 25)
    Prair = double(Pr20-(20-TfC)*(Pr20-Pr25)/(20-25));
    kair = double(k20-(20-TfC)*(k20-k25)/(20-25));
    vair = double(v20-(20-TfC)*(v20-v25)/(20-25));

else if (TfC >= 25) && (TfC < 30)
    Prair = double(Pr25-(25-TfC)*(Pr25-Pr30)/(25-30));
    kair = double(k25-(25-TfC)*(k25-k30)/(25-30));
    vair = double(v25-(25-TfC)*(v25-v30)/(25-30));

else if (TfC >= 30) && (TfC < 35)

```

```

Prair    = double(Pr15-(30-TfC)*(Pr30-Pr35)/(30-
35));
kair = double(k15-(30-TfC)*(k30-k35)/(30-35));
vair = double(v15-(30-TfC)*(v30-v35)/(30-35));

else if (TfC >= 35) && (TfC < 40)
Prair      =      double(Pr35-(35-TfC)*(Pr35-
Pr40)/(35-40));
kair      =      double(k35-(35-TfC)*(k35-k40)/(35-
40));
vair      =      double(v35-(35-TfC)*(v35-v40)/(35-
40));

else if (TfC >= 40) && (TfC < 45)
Prair      =      double(Pr40-(40-TfC)*(Pr40-
Pr45)/(40-45));
kair      =      double(k40-(40-TfC)*(k40-
k45)/(40-45));
vair      =      double(v40-(40-TfC)*(v40-
v45)/(40-45));

else if (TfC >= 45) && (TfC < 50)
Prair = double(Pr45-(45-TfC)*(Pr45-
Pr50)/(45-50));
kair  =  double(k45-(45-TfC)*(k45-
k50)/(45-50));
vair  =  double(v45-(45-TfC)*(v45-
v50)/(45-50));
end;
end;
end;
end;
end;
end;

```

```

end;
end;

%%%%%%%%%%%%%%%
%Convection Calculations
%%%%%%%%%%%%%%%
%Average temperature of surfaces 2 and 3 (the outer surface of the 1.5 inch
%pipe and the inner surface of the 2 inch pipe)
T = double((T2k-273.15+T3)/2); %[°C]

%Calculate the Rayleigh Number (Must be below 10^12 to use the %Nusselt
number equation below)
B = double(1/TfK);
RaD = double(g*B*Lc^3*(T4k-273.15-Tair)*Prair/vair^2);

%Calculate the Air Nuselt Number
Nuair = double((0.6+(0.387*RaD^(1/6))/(1+(0.559/Prair)^(9/16))^(8/27)))^2);

%Calculations
hrad1 = double(emis*SB*((T2k)^2+(T3+273.15)^2)*(273.15+T3+T2k));
hrad2 = double(emis3*SB*((T4k)^2+(Tair+273.15)^2)*(T4k+273.15+Tair));
hconv2 = double(Nuair*kair/(ro2^2));

%Calculate thermal resistances
Rrad1 = double(1/(2*pi()*L*ro1*hrad1));
Rrad2 = double(1/(2*pi()*L*ro2*hrad2));
Rconv2 = double(1/(hconv2*2*pi()*ro2*L));

%%%%%%%%%%%%%%%
%Total Thermal Resistance
%%%%%%%%%%%%%%%
Rtotal = double(Rconvin + Rcond1 + (Radvac*Rcondvac)/(Radvac +
Rcondvac) + Rcond2 + (Rrad2*Rconv2)/(Rrad2 + Rconv2));

```

Qactual = double((Toil - Tair)/Rtotal);

R=(Radvac*Rcondvac)/(Radvac + Rcondvac); %Resistance in the %annulus

T3kactual=T2k-Qactual*R; %Calculated T3 assuming radiation and %conduction approximated as parallel heat conduction in the %annulus

T3kact=T3kactual-273.15; %[°C]